Atmospheric dust transport to high-elevation Dronning Maud Land, Antarctica, over the satellite era and implications for centennial scale ice core records of dust deposition

Kevin Colet Henson

A thesis submitted to

Victoria University of Wellington

In partial fulfilment of the requirements for the degree of

Master of Science

In

Physical Geography

School of Geography, Environment, and Earth Sciences

Victoria University of Wellington

2022

TABLE OF CONTENTS

LIST OF FIGURES

LIST OF TABLES

LIST OF ANALYSES CONDUCTED AS PART OF THIS THESIS

- Interpretation of the dust dataset from the ISOL-ICE ice core*
    - Dust concentration and dust flux
    - Particle size distribution analysis
    - Change point analysis
- Dust dispersion modeling
    - Trajectory clustering
    - Emission sensitivity
- Dust-climate correlation analysis

*This thesis did not involve drilling, retrieval, or lab processing of the ice core, working up the data or dating the ice core. These were done by Winton et al. (2019). Computed dust values used in this study can be found in the attached appendix csv files.

ACKNOWLEDGEMENTS

This thesis would not have been possible without the enormous support from my supervisors, Holly Winton and Kyle Clem. Their sustained efforts to guide me throughout the year have been extremely helpful and encouraging. I firstly want to thank Holly and her colleagues from the British Antarctic Survey for allowing me to work on their ice core dataset, which surely in itself is a product of years of hard work. Holly has also been a great mentor who always provided constructive feedback to improve my research skills and writing, especially when I struggled with these. She went out of her way to give me laboratory tours and encourage me to attend conferences and workshops. Secondly, I want to thank Kyle for sharing his expertise in climate analysis and for all his help and guidance with other portions of my thesis. Kyle has also been a very supportive and motivating supervisor, especially with struggles in my thesis journey. I cannot thank both of you enough for being such excellent supervisors. You have taught me so much.

Holly, Kyle, and I would like to thank the British Antarctic Survey (BAS) and Alfred Wegener Institute (AWI) staff for their field and logistics support at Halley Station and Kohnen Station, respectively. Technical support for ice core measurements at BAS were provided by Holly Winton, Markus Frey, Robert Mulvaney, Rebecca Tuckwell, Lisa Hauge, Julius Rix, Catriona Sinclair, Emily Ludlow and Shaun Miller. The ISOL-ICE ice core project was supported by a National Environment Research Council (NERC) Standard Grant (NE/N011813/1) to Markus M. Frey.

Lastly, I would like to express my sincerest gratitude to my family and friends both here in New Zealand and back home. I would like to thank my friends and family back home for the regular video calls, always reminding me that though I am far away, you guys are always there to support me through thick and thin. Doing my thesis in a pandemic-stricken time would also not be possible without my friend circles here in New Zealand – the conservation biologists (Nai, Jamie, Steph, Mau, Sandra, Maddie), the scholarship group (Indi, Mai, Jodel, Tristan, Novia, Asty, Manisha, Fariya, Javier, Daniel, Mastura), and my university friends (Selina, Corinna, Simon, Keren, Meg, Jack, Sofia, Josh). All of you have been my family away from home, and though our paths are diverging, I am eagerly looking forward to reunions around the world. You have truly filled my stay here in New Zealand with unforgettable memories.

ABSTRACT

Deposition of aeolian mineral dust recorded in Antarctic ice cores is strongly tied to large-scale atmospheric circulation variability. This natural archive can be used to extend knowledge about atmospheric circulation variability in the Southern Hemisphere (SH) prior to the satellite era (1979-2017). Additionally, dust plays an important role in the climate system through cloud formation processes, the radiation budget, and as a micronutrient source for biological productivity in the Southern Ocean. Hence, investigating the drivers of Antarctic dust variability is useful for better understanding past and future changes to SH climate. This thesis investigates present-day dust transport to a high elevation ice core site in Dronning Maud Land (DML; 74°60′S, 0°6′E), Antarctica, where an anomalous increase in dust deposition is observed over the past century in a 1300-year ice core recently drilled as part of the Isotopic Constraints on Past Ozone Layer in Polar Ice (ISOL-ICE) program.

This study aims to determine the potential source area (PSA) and atmospheric transport mechanism of dust deposited to high-elevation DML over the satellite era. Additionally, the implications of the findings for ice core dust records spanning the last millennium are also discussed. The specific objectives of this study are: 1) identify dominant atmospheric dust transport pathways to DML over the satellite era, 2) determine regional climatic controls of particle size distribution (PSD) at DML over the satellite era, and 3) contextualise the recent increase in dust deposition at DML relative to the last millennium.

To achieve these three objectives, dust deposition to the ISOL-ICE ice core site over the satellite era is examined using dust dispersion modeling (Flexpart model; Pisso et al., 2019) and correlation analysis with a range of climate parameters, such as geopotential height, zonal and meridional winds, and precipitation, using the ERA-interim atmospheric reanalysis dataset (Dee et al., 2011). Flexpart is configured to run backward dust dispersion simulations to investigate dust transport pathways and potential source areas to the ISOL-ICE site constrained by PSD observations from the ISOL-ICE core. The correlation analysis determines which large-scale circulation/climate patterns are important for dust transport to ISOL-ICE site. Both methods help ascertain drivers of modern dust transport to the ISOL-ICE site, providing new insights into potential drivers of the observed dust variability before the satellite era.

Analysis of the ISOL-ICE dust record reveals an abrupt 10-fold increase in dust deposition relative to the past millennium that occurred over ~15 years from 1915 to 1930 CE. Dust flux increased from a background mean of 0.03 mg m^{-2} yr^{-1} (668-1915 CE) to 0.30 mg m^{-2} yr^{-1} (1915-2017). Similarly, the coarse particle percentage (CPP) of dust, a proxy for PSD, rose from a mean of 71 % before 1900s to 83 % after the abrupt shift in dust flux. This abrupt increase is not observed in other ice core dust records from the Antarctic Peninsula, West Antarctica, or coastal DML, suggesting that the observed increase is a regional and/or high-elevation signal rather than Antarctic-wide.

The ISOL-ICE ice core dust deposition is characterised by relatively low dust concentration and dust flux, fine particle size (a dust mode of ~3.5-3.8 μm) for long-range transported dust (1-10 μm), and a maximum seasonal deposition in winter/spring. These characteristics combined with back trajectory analysis point to long-range transport from remote southern South America (SSA) as the dominant PSA. Back trajectory modeling shows that dust is transported to the ISOL-ICE site dominantly from the eastern coast of SSA between 47-50°S, and that dust transport pathways from SSA to the ISOL-ICE site are insensitive to particle size and seasonality over the satellite era. Moreover, dust from SSA are uplifted to ~1500 meters above sea level (m.a.s.l.) over the SSA region and are transported with increasing altitude towards DML. While SSA is the dominant PSA for the ISOL-ICE site, additional inputs from nearby Antarctic dust sources cannot be ruled out based on the presence of large coarse particles (10-50 μm) and published geochemical evidence from nearby ice core sites in DML.

The observed interannual variability of dust CPP at the ISOL-ICE site over the satellite era is associated with cyclonic circulation south of SSA, further supporting long-range transport of dust from SSA to the ISOL-ICE site. This circulation pattern explains 9-36 % of the observed variability in CPP at the ISOL-ICE site and is associated with convective activity in the South Pacific Convergence Zone (SPCZ) and the central tropical Pacific. During winter and spring, dust is transported to the ISOL-ICE site through a deep and broad Amundsen Sea Low, coinciding with the observed seasonal maximum in dust deposition at the site. During summer and autumn, the proposed dust transport occurs through a cyclonic circulation over the Drake Passage that is tied to the Pacific Decadal Oscillation (PDO). Interestingly, the

El Niño Southern Oscillation (ENSO) and the Southern Annular Mode (SAM) do not appear to be significant drivers of cyclonic activity south of SSA and consequent dust transport to the ISOL-ICE site contrary to published ice core studies from coastal DML and West Antarctica that implicate SAM and ENSO as important drivers of dust transport from SSA to Antarctica.

This study, combined with geochemical evidence from high-elevation DML over the last glacial and Holocene period, suggests that the present-day dominant PSA of South America did not change since the last glacial period. In addition, dust transport pathways and the seasonality of dust deposition also did not change over this period. These constant factors suggest that the abrupt increase in dust concentration over the last century could have resulted from either 1) an enhanced cyclonic circulation south of SSA related to the SPCZ and PDO or 2) changing conditions at the two PSA regions (SSA and dust input from nearby Antarctic dust sources). Stronger cyclonic activity south of SSA leads to enhanced wind flow and drier conditions over SSA allowing for increased dust transport from SSA to the ISOL-ICE site. Comparatively, changes in source conditions (e.g., aridity and soil sediment supply) in the PSA alter the availability and physical characteristics of emitted dust particles.

The established relationship between dust CPP and the cyclonic circulation south of SSA over the satellite era provides a foundation for future work to investigate the drivers of dust variability in the high-elevation DML region over the past millennium. Findings from this study are also useful for investigating episodic dust events within

the satellite era and potentially predicting how dust transport patterns will evolve in the future based on projected changes to atmospheric circulation patterns.

1. INTRODUCTION

1.1 Motivation

Aeolian mineral dust is widely utilised as an indicator of environmental change. Dust entrainment, transport, and deposition processes are sensitive to atmospheric circulation and precipitation (Fig. 1.1; Kok et al., 2012; Bullard et al., 2016; Marx et al., 2018). This allows information about local and large-scale circulation variability to be inferred from dust records (e.g., Koffman et al., 2014; Laluraj et al., 2020). At the source regions, dust emission is also dependent on land surface properties, such as land cover and soil moisture content (Hooper & Marx, 2018; Bullard et al., 2016; McConnell et al., 2007). Both atmospheric and land surface drivers of dust variability operate simultaneously and in conjunction with one another (Marx et al., 2018; Marticorena, 2014). Thus, there is a need to deconvolute these parameters to separate dust variability associated with each control. This study focuses on investigating the relationship between dust transport and atmospheric circulation.

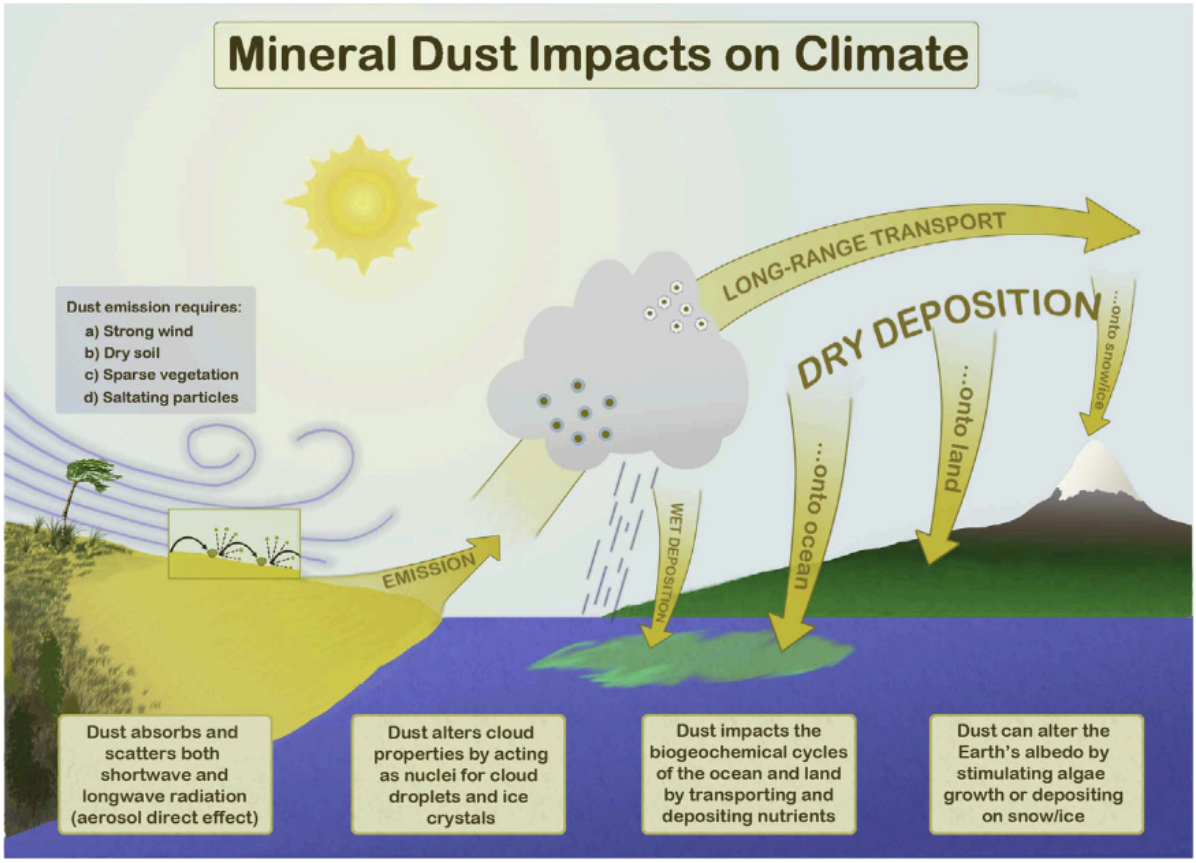

Figure 1.1 Schematic of interactions of dust with climate and biogeochemistry. From Mahowald et al. (2014).

Apart from its utility in investigating atmospheric circulation variability, another motivation for studying aeolian dust variability is the wide-ranging influence of mineral dust on several aspects of the coupled ice-ocean-climate system (Fig. 1.1). Dust particles affect the radiative balance in a region by serving as an intermediary layer in the atmosphere, scattering and absorbing incoming solar radiation and outgoing terrestrial radiation (e.g., Tegen et al., 1996; Ackerman & Chung, 1992). Furthermore, surface reflectivity can be altered in dust laden snow and ice where increased absorption of solar radiation enhances surface melt (Bullard et al., 2016; Marx et al., 2018). Dust particles can also indirectly modify the energy budget by serving as cloud condensation/ice nuclei, influencing cloud formation and properties (Schepanski et al., 2014; Bullard et al., 2016). Lastly, mineral dust is an important source of new iron to

the iron limited waters of the Southern Ocean. Additions of atmospheric iron from deposited atmospheric dust stimulate phytoplankton productivity and consequent CO_2 uptake into the ocean (Martin, 1990; Yamamoto et al., 2019). Iron fertilisation has been hypothesised to drive glacial periods: increased (decreased) iron supply leads to higher (lower) biological productivity and enhanced (reduced) CO_2 drawdown into the ocean (Sigman et al., 2010; Yamamoto et al., 2019; Lambert et al., 2015). Investigating the relationship between dust and atmospheric circulation variability will therefore aid in understanding potential future changes to these components of the SH climate system.

1.2 Research question

This research aims to examine the question: "From where and how is dust transported to high-elevation Dronning Maud Land (DML), Antarctica, over the satellite era?" Based on the findings over the satellite era (1979-2017), implications for dust deposition variability to high-elevation DML over the last millennium are also suggested. To answer the research question and the consequent implications for centennial ice core records, this study investigates an anomalous increase in dust deposition observed over the past century in the new ISOL-ICE dust record from Kohnen Station, DML, Antarctica (74°60′S, 0°6′E; Fig. 1.2). While the focus of this study is the last century, the observed increase in dust deposition is contextualised within the entire length of the dust record spanning the last millennia. An increase in dust deposition over the last century is also observed in other Antarctic ice cores, namely from James Ross Island (JRI; McConnell et al., 2007), West Antarctic Ice

Sheet (WAIS) Divide (Koffman et al., 2014), and the coastal DML (IND-25/B5; Laluraj et al., 2020), thereby suggesting an Antarctic-wide change in dust deposition over the past century.

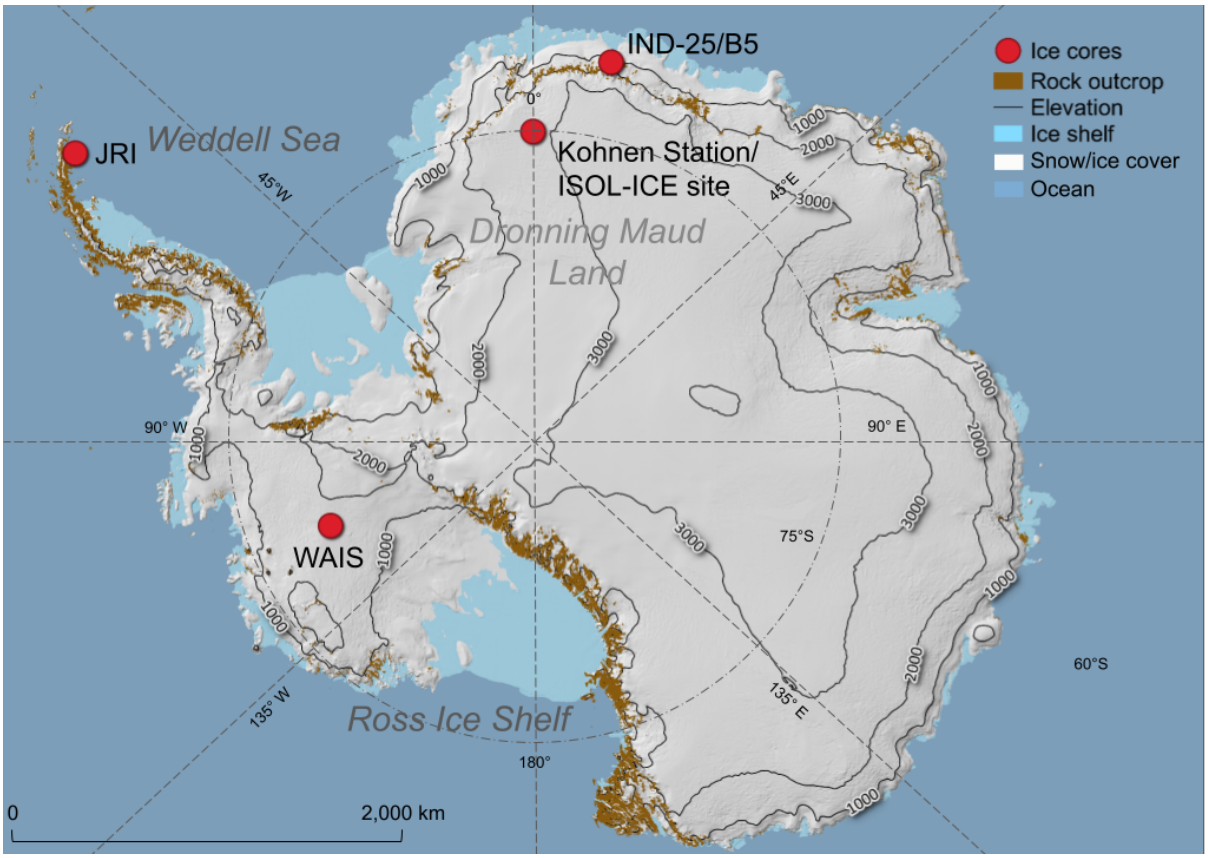

Figure 1.2 Map of Antarctica showing the location of ice core locations mentioned in this study and relevant topographical features. Elevation is in meters above sea level. Map was generated using the Quantarctica package (Matsuoka et al., 2021).

1.3 Thesis aims

The overall aim of this project is to investigate temporal and spatial relationships between dust deposition in DML and atmospheric circulation variability over the satellite era. The hypothesis is that dust deposition at the ISOL-ICE site over the satellite era is dominantly associated with large-scale atmospheric circulation patterns

in the mid to high latitude Southern Hemisphere (SH). The specific objectives of this study are to:

1) Identify dominant atmospheric dust transport pathways to the ISOL-ICE site over the satellite era;

2) determine regional climatic controls of particle size distribution (PSD) at the ISOL-ICE site over the satellite era; and

3) contextualise the recent increase in dust deposition at the ISOL-ICE site over the last millennium.

2. BACKGROUND

2.1 Dust Lifecycle

2.1.1 Dust definition

For the purposes of this study, dust is defined as insoluble particles that have been deflated (wind-blown/eroded) from the ground and suspended into the atmosphere, and have a diameter ranging between 0.9 and 50 μm. Insoluble particles have been widely used as a proxy for atmospheric dust in ice cores (e.g., Ruth et al., 2008; Lambert et al., 2008; Delmonte et al., 2002). Examples of insoluble particles may include soil particles, volcanic ash, and diatoms (Bullard et al., 2016). In general, these aerosols are less than ~100 μm in diameter (Marx et al., 2018), typically in the sediment size class of silt (<63 μm) and clay (<4 μm) (Bullard et al., 2016). Dust size

ranges are operationally defined due to the methods of measuring dust concentration and particle size in ice cores (section 3.1.1.4) and as such, includes non-crustal material such as pollen and diatoms, which are biogenic in origin but represent relatively low concentrations compared to crustal material (Tetzner et al., 2021). In terms of elemental composition, mineral dust particles are generally composed of Si, Al, and Fe along with trace elements such as Ti, Ni, Cr, and Pb. However, the percentage contribution of each element varies regionally (Pye, 1987; Ruth et al. 2008; Lawrence et al., 2010).

2.1.2 Dust entrainment

Dust emission and entrainment processes are partly dependent on wind properties at the source region (Schepanski et al., 2014; Kok et al., 2012; Marx et al., 2018). Dust is generated largely as a result of saltation (Fig. 2.1), which involves the continuous hopping of sand particles initiated due to surface wind shear stress at site-specific wind speed thresholds (Bagnold, 1941; Marticorena, 2014). Once saltation is initiated, sandblasting occurs wherein the repeated collision of sand particles ejects smaller dust particles, which are then suspended into the atmosphere in accordance with the equation of terminal velocity — accounting for both gravitational force and air resistance (Bagnold, 1941; Pye, 1987). Additionally, a sheared wind flow environment, describing the logarithmic profile of wind speed across altitude, creates pressure differences between the top and bottom side of a grain thereby inducing lift (the Bernoulli effect) (Pye, 1987). This dependence of dust emission on wind properties is expressed in the fact that the entrainment of dust particles is strongly positively

correlated to wind velocity and turbulence intensity (Bullard et al., 2016). Turbulence involves unstable fluctuations of wind flow known as eddies. These irregular motions of air enhance sandblasting and impart vertical momentum to particles important for their uplift (Bagnold, 1941; Pye, 1987).

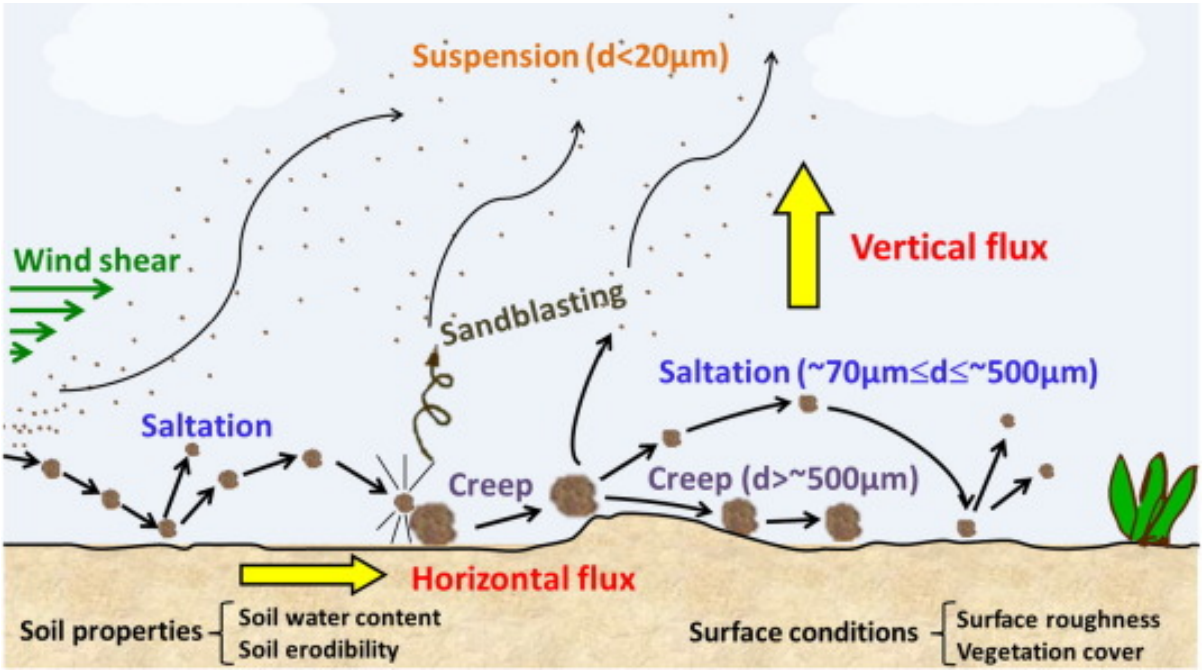

Figure 2.1 Schematic of dust entrainment processes. Typical diameters of particles are noted for each process. From Gherboudj et al. (2017).

Particle size influences the strength of dust mass emission at source regions. The PSD of emitted dust is largely dictated by the PSD of the soil and prevailing meteorological conditions (Marx et al., 2018), though the exact sensitivity to each of these parameters remains debated (Kok et al., 2012). Measurements of emitted dust PSDs typically show a size mode (dominant particle size) of ~ 10 μm, but these can vary regionally (Fig. 2.2; Mahowald et al., 2014). In general, smaller (larger) particles are more (less) susceptible to wind flow because of weaker (stronger) inertial forces. Due to smaller size and higher susceptibility to wind flow, fine dust particles (< 20 μm) remain suspended in the air (Bagnold, 1941; Bullard et al., 2016; Kok et al., 2012).

However, it has also been shown through field measurements that PSD during emission is insensitive to wind speed (Kok et al., 2011). This suggests that while dust particles are emitted at a certain wind speed threshold, the size of the particles do not vary significantly with wind speed past this threshold. Though once uplifted, with stronger winds, particles can more easily remain suspended in the atmosphere and thus be transported over longer distances compared to weaker flow (Schepanski et al., 2014). Prolonged suspension of fine particles allows for dust to be transported long-range (> 2000 km), such as to Antarctica (e.g., Koffman et al., 2014, Laluraj et al., 2020), and is primarily associated with regional atmospheric circulation. In contrast, proximal coarser (> 20 μm) dust particles are associated with local wind systems, such as valley winds (Pye et al., 1995).

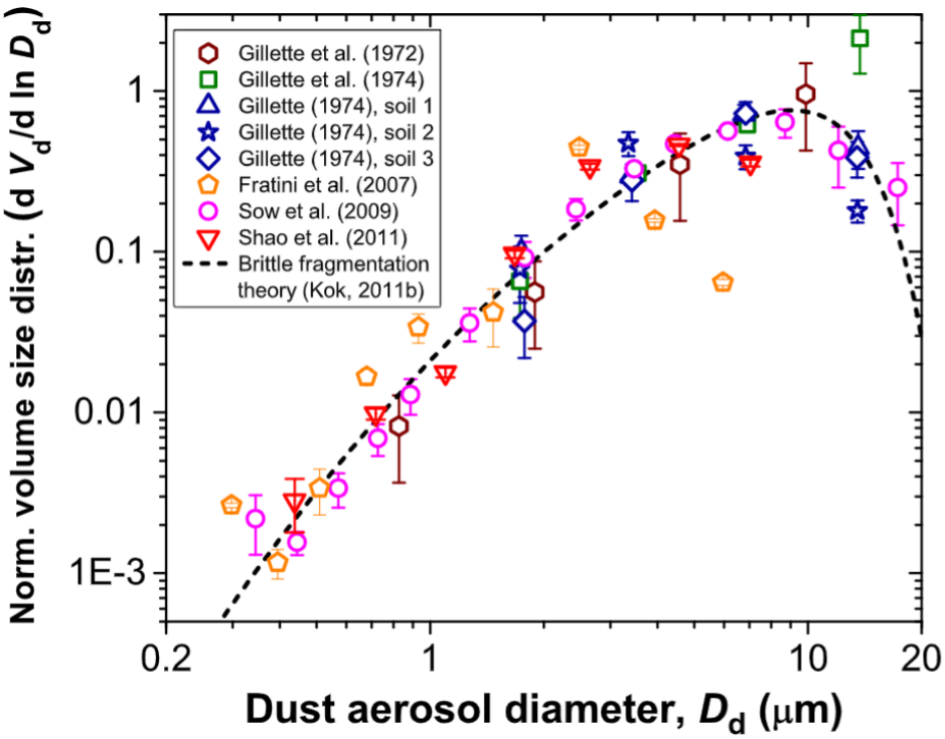

Figure 2.2 Compilation of measured of Particle Size Distribution (PSD) at source regions. Samples are taken from several locations such as Nebraska, Texas, China, Niger, and Australia. The PSD is expressed as normalised volume size distribution. From Mahowald et al. (2014).

Aside from atmospheric processes, land surface characteristics also influence dust entrainment at source areas (Fig. 2.1). Surface protruding objects, such as vegetation canopy and buildings, affect surface roughness and change the vertical wind velocity gradient by obstructing wind flow near the ground. The resulting weaker surface winds hinder saltation and dust entrainment (Marticorena, 2014). Soil moisture also controls dust generation by means of influencing interparticle cohesion and vegetation growth. Wet surfaces encourage vegetation growth and decrease sediment availability (for deflation) while the opposite is true for dry surface conditions (Kok et al., 2012; Marticorena, 2014). Shifts from natural vegetated surfaces to anthropogenic landscapes, such as croplands and mining depots, alter the efficacy of dust generation in the region by increasing surface exposure of sediments and consequent wind erosion (McConnell et al., 2007; Hooper & Marx, 2018). The magnitude of such change, however, varies regionally and requires individual quantification (Marx et al., 2018).

2.1.3 Dust Transport

Atmospheric dust pathways to Antarctica follow prevailing wind patterns. Depending on the variability of wind flow patterns, source and destination regions may change over time, especially during major shifts in circulation patterns that occur on decadal to millennial timescales. Changes to the mean position and characteristics of synoptic weather systems can alter regional wind strength and airmass trajectories (Marx et al., 2018). Some examples of prominent shifts include the latitudinal migration of the circumpolar westerly wind belt over decadal-centennial timescales (e.g.,

Koffman et al., 2014; Abram et al., 2014) and the deepening of the Amundsen Sea Low (ASL) pressure system (Turner et al., 2013) observed over the past few decades (Raphael et al., 2016). Cyclones and anticyclones drive both horizontal and vertical transport of dust since these systems are characterised by specific wind flow patterns (Li et al., 2010; Reijmer & Oerlemans, 2002). In the SH, cyclones describe a general convergent, upward, and clockwise flow of air with strong pressure gradients and wind speed (Wallace & Hobbs, 2006). While dust is potentially uplifted and transported poleward through these systems, removal of particles in these systems through cloud formation and precipitation also occurs due to the convective nature of cyclones (Knippertz, 2014). The opposite flow patterns occur with SH anticyclones; airmasses are descending in a counter clockwise and outward direction. Unlike cyclones, anticyclonic activity is often associated with weak pressure gradients and slower wind speeds (Wallace & Hobbs, 2006). The influence of cyclones and anticyclones on dust transport is not generalisable due to the interplay of several factors, such as wind strength and particle removal efficiency. Nonetheless, these systems contribute to determining regional dust transport patterns (Li et al., 2010; Knippertz, 2014).

The PSD of dust particles undergo changes during transport. For long-range transported dust, particles smaller than ~20 μm (typically <5 μm) are more relevant for transport due to increased susceptibility to suspension (Marx et al., 2018; Bagnold, 1941; Struve et al., 2020). Without sufficient turbulence from strong winds, grains larger than 20 μm usually settle back down quickly near source regions (Pye, 1987). Transported dust experiences a reduction in size proceeding downwind with distance from the source due to preferential deposition of coarser particles resulting from higher mass and settling velocity (Stuut & Prins, 2014; Pye et al., 1995). Vertically, finer grains

are more susceptible to uplift and thus progressively dominate the size mode in higher atmospheric levels (Lambert et al., 2008; Delmonte et al., 2019). Dust PSD during transport is therefore partly a product of size sorting through depositional processes and susceptibility to wind flow rather than wind-induced size sorting during emission, as suggested by Kok et al. (2011).

2.1.4 Dust Deposition

En route, dust is removed from the atmosphere by wet or dry deposition. The former consists of in-cloud and below-cloud scavenging wherein particles are removed from the atmosphere through water-related processes. In-cloud scavenging involves the conversion or collision of particles into condensation/ice nuclei, which comprise cloud mass (Kok et al., 2012). Conversion into condensation/ice nuclei occurs when water vapor condenses (and potentially freezes) onto a dust particle once the air is sufficiently saturated (Bergametti & Foret, 2014). Saturation is typically achieved through the decrease in air temperature with altitude; particles that are lifted to higher tropospheric levels are therefore more susceptible to in-cloud scavenging (Wallace & Hobbs, 2006). Comparatively, below-cloud scavenging occurs through precipitation; snow or rain droplets collide with suspended particles thereby removing them from the atmosphere (Bergametti & Foret, 2014). Dry deposition occurs through gravitational settling of particles with turbulent diffusion in the atmospheric boundary layer typically within 1000-2000 meters above sea level (m.a.s.l.) (Kok et al., 2012; Bagnold et al., 1941). These processes are dependent on particle size, wherein settling velocity is a function of the diameter of a particle squared, following Stokes law. The overall lifetime

of dust particles is dependent on the efficacy of these deposition regimes (Kok et al., 2012).

Depositional processes are known to affect PSDs of atmospheric dust. In general, wet deposition is thought to dominate aerosols smaller than ~ 5 μm, while dry deposition dominates particles larger than this size (Kok et al., 2012; Lawrence et al., 2010). Additionally, dry deposition is more pronounced for proximal transport compared to distal transport due to a larger fraction of coarse particles emitted from source regions. Comparatively, wet removal of dust particles is more prevalent further downwind due to the higher proportion of finer particles (Bergametti & Foret, 2014). However, the exact effect of these processes on PSDs remains equivocal and varies regionally (Wegner et al., 2015; Stuut & Prins, 2014). Given the influence and dependence of particle size on the dust lifecycle (i.e., entrainment, transport, and deposition), PSDs can therefore be used to infer changes to dust transport and potential source areas, which in turn can be indicative of changes in atmospheric circulation (e.g., Koffman et al., 2014). However, it is difficult to make interpretations about dust transport from PSDs alone since PSDs can also reflect changes from source regions, and therefore multiple lines of evidence are required to interpret the potential source areas (PSA) for ice core dust records.

2.2 Antarctic dust deposition

Over Antarctica, atmospheric dust is deposited and preserved in ice sheets (Vallelonga & Svensson, 2014; Pye et al., 1995). Deposited dust particles are

preserved through the densification of annual snow layers into firn and recrystallization into ice (Fig. 2.3). Polar ice cores (especially in high elevation regions) therefore archive long-range transported dust from major dust regions (Vallelonga & Svensson, 2014) in addition to locally sourced dust. Ice cores may provide sub-annual resolution dust records, whereas in other natural archives (e.g., marine sediments, loess), such high resolutions are typically not resolved.

Figure 2.3 Example of dust stored in a segment of an ice core drilled in Greenland. Photo taken by Bradley Markle.

2.2.1 Temporal Dust Variability

Some of the largest dust variations have occurred over glacial-interglacial timescales (Marx et al., 2018; Lamy et al., 2014; Lambert et al., 2008). Antarctic ice cores have shown as much as ~20 times increased dust content during glacial periods relative to interglacials (Fig. 2.4; Lambert et al., 2008; Petit et al., 1999). It is thought that colder and drier glacial periods are typified by stronger winds and a less active hydrological cycle compared to warmer and wetter interglacials. Increased surface wind speeds, coupled with lower soil moisture content and sparse vegetation cover,

results in a more conducive overall environment for dust generation during glacials. The opposite is true for interglacials, wherein weaker winds and wetter conditions inhibit dust entrainment (Bullard et al., 2016). It has been proposed that the dramatic increase in dust during glacial periods leads to increased biological productivity in the Southern Ocean and consequent reduction in atmospheric CO_2 through drawdown into the ocean (Martin, 1990). Conversely, lower atmospheric dust loading during the interglacials weakens CO_2 uptake into the ocean due to reduced phytoplankton carbon production. This relationship between dust and atmospheric CO_2 concentrations is thought to help drive climate shifts on glacial-interglacial timescales (Lamy et al., 2014; Shaffer & Lambert, 2018). However, dust-climate coupling is thought to be stronger during glacial periods versus interglacials. As much as 90 % of dust variability can be explained by temperature variations during glacial periods, whereas there is significantly less correlation between dust and temperature during interglacial periods (Fig. 2.4; Lambert et al., 2008). Dust variability during warm interglacials, including the Holocene, could represent a different set of drivers and mechanisms influencing dust processes (e.g., Koffman et al., 2014). This study aims to address this mismatch between dust-climate variability on glacial-interglacial versus interannual-millennial timescales.

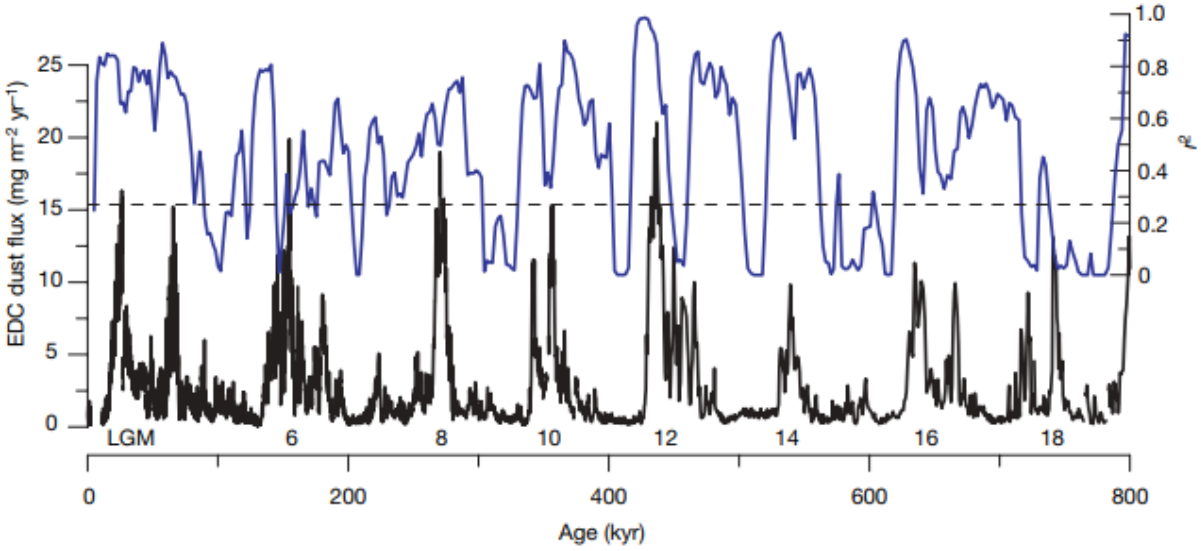

Figure 2.4 Correlation between dust and temperature from the European Project for Ice Coring in Antarctica (EPICA) Dome C ice core. Linear plot of dust flux (black) and the coefficient of determination r^2 (blue) between the high-pass filtered values (18-kyr cut-off) of both the δDeuterium and the logarithmic values of dust flux. The correlation was determined using 2-kyr mean values in both records and a gliding 22-kyr window. Correlations above $r^2 = 0.27$ (dashed line) are significant at a 95 % confidence level. Numbers indicate the marine isotopic glacial stages. From Lambert et al. (2008).

While there is a clear overall pattern for dust concentrations over glacial-interglacial cycles, less is known about changes in PSDs over these timescales. Ice cores from the European Project for Ice Coring in Antarctica (EPICA) DML, Dome C, and Komsomolskaya sites show an increase in particle size during the warmer interglacials compared to glacial periods (Wegner et al., 2015; Delmonte et al., 2004), while other sites, such as Dome B on the East Antarctic Plateau, show larger particles deposited during glacial periods (Delmonte et al., 2004). The differences in glacial-interglacial particle size patterns are likely due to different transport pathways and PSAs for different ice core site (e.g., Laluraj et al., 2020; Koffman et al., 2014). Hence, it is important to understand site-specific relationships between particle size and climate to able to make any connections between these two variables. The EPICA DML (EDML) ice core was drilled approximately ~1 km from the ISOL-ICE site, thereby making it the closest ice core dust record to the ISOL-ICE site. The particle size mode

for the EDML core was ~2.0 μm during the last glacial period, rising to ~2.2 μm in the Holocene (Wegner et al., 2015).

Over centennial timescales, significant dust deposition variability has also been observed in Antarctica. The EPICA Dome C ice core in the East Antarctic Plateau records rapid decreases in dust flux coinciding with abrupt warming events that occur ~2-3 times every 10 kyr throughout the last 800 kyr (Lambert et al., 2012). The WAIS dust record shows notable increases in dust particle size between ~1050-1400 CE and over the last 50 years, while relatively smaller particle sizes are detected from 1430 CE to the mid-late 20th century (Koffman et al., 2014). For both Dome C and WAIS cores, latitudinal shifts to the SH circumpolar westerly winds have been suggested as the cause of the observed dust variability (Lambert et al., 2012; Koffman et al., 2014).

The seasonality of dust deposition in Antarctica varies from site to site. For instance, a winter/spring maximum in dust deposition is observed for the JRI (McConnell et al., 2007) and EDML (Wegner et al., 2015) core, while snow-pits from Berkner Island in the Weddell Sea region show a maximum in summer (Bory et al., 2010). Thus, there is no Antarctic-wide seasonality in dust deposition, and the differences in seasonality for each site is likely tied to different combinations of PSAs and regional dust transport patterns.

2.2.2 Key climate periods and anthropogenic events in the last millennium

Since the main ice core record used in this study spans the last millennium, important climatic/anthropogenic periods and events that may be related to dust deposition at the ISOL-ICE site are discussed in this section. The Medieval Warm Period (MWP; Lamb, 1965), also known as the Medieval Climate Anomaly (Grove & Switsur, 1994) is generally agreed to have occurred between 800-1300 CE (e.g., Lüning et al., 2019; Crowley & Lowery, 2000; Mann et al., 2009). Temperatures during this interval, primarily in the Northern Hemisphere, are relatively higher than in adjacent time periods and are thought to have been caused by changes in volcanic and solar activity (Masson-Delmotte et al., 2013). After the MWP, the Little Ice Age (LIA; Grove, 2004; Mann et al., 2009) describes a period of relatively colder temperatures occurring between 1450-1850 CE discovered through evidence of glacial advances in the Northern Hemisphere. Similar to the MWP, the LIA is also thought to have resulted from variations in volcanic and solar activity (Masson-Delmotte et al., 2013). Though it is debated whether the MWP and LIA are global or Northern Hemisphere signals in scope, there is evidence to suggest that the both patterns are observed as far south as Antarctica (e.g., Luning et al., 2019, Simms et al., 2021). The Industrial Revolution began around ~1750 CE onwards. Rapid industrialization (especially in the Northern Hemisphere) instigated the steady increase in carbon dioxide and global-mean temperature.

Globally, a doubling of dust concentrations since the Industrial Revolution has been observed in numerous natural archives and instrumental records. The timing of such global increase in dust concentrations suggests an anthropogenic cause, such as widespread land conversion (Hooper & Marx, 2018). Over the last century, dust bowls occurred both in North America (Schubert et al., 2004), and in the Argentinean Pampas region in South America (Bernardos et al., 2001; Viglizzo & Frank, 2006). In South America, mass agricultural land conversion and overgrazing of livestock are thought to have led to the degradation and desertification of natural areas most pronounced in the 1930s and 1940s. This rapid land use change was accompanied by anomalously dry and windy conditions resulting in increased dust emissions in southern South America (SSA) during this period (Viglizzo & Frank, 2006).

While land use change is implicated as the cause of the increase in dust since the Industrial Revolution (Hooper & Marx, 2018; McConnell et al., 2007), its contribution to the dust increase is difficult to quantify due to limited land cover datasets, varied anthropogenic land use activities, and significant influence of external factors (such as climate). Furthermore, disentangling the two-way interactions between land surface and atmospheric processes remains challenging. For instance, precipitation and humidity directly affect soil moisture content (Marx et al., 2018; Marticorena, 2014), while conversely, evaporation of soil moisture contributes to air saturation and consequent precipitation (Hartmann, 2016).

2.3 Study area information

2.3.1 Site Characteristics

The primary ice core investigated in this study was drilled near Kohnen Station (74°60′S, 0°6′E), DML, Antarctica, as part of the National Environment Research Council (NERC) funded project “Isotopic Constraints on Past Ozone Layer in Polar Ice” (ISOL-ICE). Kohnen Station is a summer-only research station where the deep (~2800 m) EPICA DML ice core was recovered (Oerter et al., 2009). The station is a high elevation inland (rather than coastal) site approximately 550 km from ice shelf edge with an elevation of 2,892 m.a.s.l (Fig. 1.2). To prevent downwind contamination from Kohnen Station buildings, the location of the drilling site is in the clean-air sector of Kohnen Station located ~1 km from the station. Kohnen Station is ideal for studying long-range transport of dust from sub-Antarctic regions as there is likely less contribution from local Antarctic dust sources due to the site’s inland position and high elevation.

2.3.2 Local meteorology

Local meteorology at the ISOL-ICE site is described by certain features. Temperature at the site ranges from -9°C to -74°C, with an annual average of -41°C and a mean summer temperature of -28°C as measured by the University of Utrecht Automatic Weather Station 9 (DML05/Kohnen) since 1997 (https://www.projects.science.uu.nl/iceclimate/aws/files_oper/oper_20632) The surface wind direction is

predominantly northeasterly across all seasons (Fig. 2.5), suggesting air mass intrusions coming from the South Atlantic. The mean snow accumulation rate at the site measured between 1259-1997 CE is relatively low (~6 cm yr^{-1} water equivalent; Oerter et al., 2000) compared to coastal sites, which exhibit annual mean accumulation rates of ~10 to 100 cm yr^{-1} water equivalent over the satellite era (Thomas et al., 2017). Additionally, ~80 % of the precipitation is sourced from frontal cloud systems (Reijmer & Oerlemans, 2002), with majority of precipitation falling in a small number of heavy precipitation events (Turner et al., 2019b).

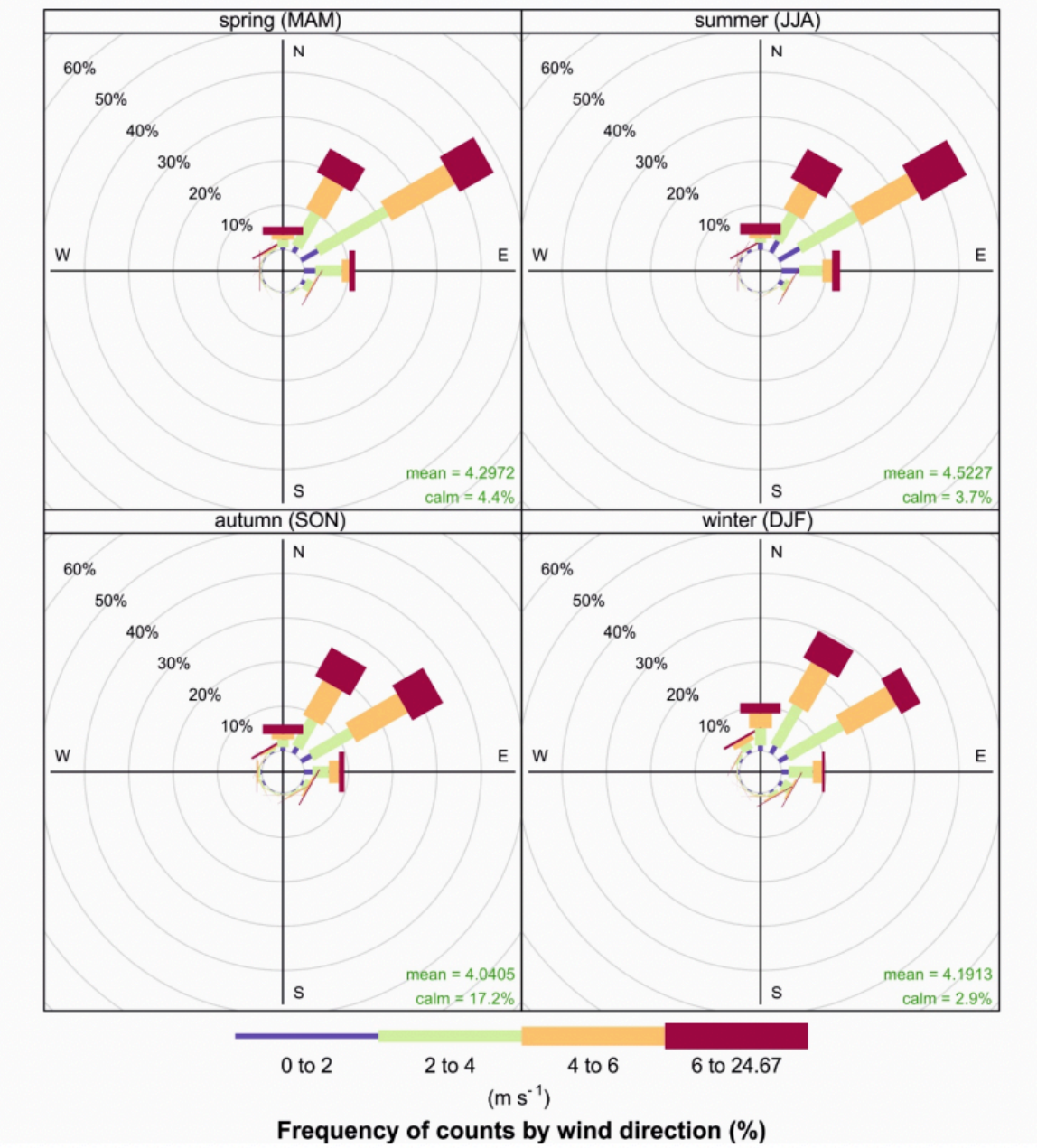

Figure 2.5 Seasonal wind rose at Kohnen Station (74°60′S, 0°6′E) from hourly automatic weather station data from 29/12/1997 18:00 UTC to 19/03/2017 08:00 UTC. From Winton et al. (2020).

Local northeasterly winds at the site are associated with katabatic flows from the Antarctic interior. Katabatic winds are downslope flows that occur as a result of temperature and pressure gradients across an inclined surface, in this case from the plateau to coastal regions (Parish & Bromwich, 2007; Broeke & Lipzig, 2003b). Katabatic flow is persistent throughout the year but is most pronounced during winter when meridional temperature and pressure gradients are strongest (Broeke & Leipzig,

2003b). The katabatic flows from the plateau exert downward momentum on air masses entering the north Atlantic sector of Antarctica. Consequently, long-range transported dust in the mid-high troposphere is entrained downwards towards the surface (Laluraj et al., 2014).

The climate in the DML region is largely influenced by cyclones tracking eastward along the coast. Cyclonic activity originates from the Southern Ocean, and the effect of these cyclones is more pronounced in coastal Antarctic regions compared to inland areas (Reijmer & Oerlemans, 2002). Lower troposphere convergent (divergent) flow in cyclones (anticyclones) contain an upward (downward) component thereby transporting dust particles to upper (lower) tropospheric levels (Wallace & Hobbs, 2006; Li et al., 2010). These synoptic-scale (~1,000 km) eddy circulations result from pressure anomalies in the greater region spanning the middle-to-high latitude South Pacific, Antarctic Peninsula, southern South America, and DML (e.g., Rondanelli et al., 2019; Ding et al., 2012).

2.3.3 Potential dust source areas to the DML region

In terms of remote PSA, the SSA region is currently the dominant dust emitter in the SH high latitudes (Delmonte et al., 2019; Gassó & Torres, 2019; Bullard et al., 2016; Vallelonga, 2014). The SSA dust emissions are estimated to be 54-79 Tg year^{-1} while Australia emits 47–63 Tg year^{-1} (Ginoux et al., 2012). The SSA region, specifically Patagonia, covers ~900,000 km^2 of territory featuring high topographical ranges, semi-arid scrub-grasslands, and desert regions from 39-55°S (Bullard et al.,

2016; Gassó & Torres, 2019). The western section is dominated by the Andean cordilleras and dissected plateaus punctuated by glaciers and glacial landforms. Glacial grinding produces a significant amount of fine sediment that is transported downstream to floodplains via fluvial systems (Bullard et al., 2016; Marx et al.,2018; Pye, 1987). The ongoing retreat of glaciers is expected to expose more land surface area to wind erosion and thus increase dust entrainment in the region. Moreover, the presence of ice masses in these high elevation areas instigate strong katabatic winds that together with sparse vegetation, provide a conducive environment for dust storms in the eastern plains (Bullard et al., 2016; Marx et al.,2018). In terms of climate, the regional atmospheric circulation is dominated by strong and persistent westerly winds and cold frontal systems that uplift dust sediments (Vallelonga, 2014). These prevailing wind conditions create a strong east-west gradient in precipitation wherein annual values range from ~4000 to 7000 mm in the western side and only ~200 mm in the east. This rain shadow effect maintains the semi-arid scrub/grasslands and arid desert regions in eastern Patagonia (Bullard et al., 2016). Combined, the terrain and climatic conditions in the region underpin the high frequency (as much as 30 yr^{-1}) of dust storms occurring in Patagonia (Gassó & Torres, 2019; Bullard et al., 2019).

Some dust activity hotspots include Tierra del Fuego (53.8°S 67.8°W; Gassó et al., 2010), the San Julia's Great Depression (49.5°S 68.5°W; Li et al., 2010), and Colihue Huapi lake (46.56°S 70.74°W; Gassó et al., 2010; Gassó & Torres, 2019). These regions are all associated with scattered dry lakes (Gassó et al., 2010; Gassó & Torres, 2019; Li et al., 2010). In the Colihue Huapi lake region, changes to the lake area show a strong correlation (R=0.69) with reported dust events in downwind regions. Over the past 50 years, surface and satellite observations have shown a

positive trend in dust activity (Gassó & Torres, 2019). While this is an isolated case study, the same scenario could be occurring in other Patagonian regions due to the abundance of dry lakes. The increase in dust emissions is likely due to the combined effect of lake desiccation, associated with climatic conditions (Gassó et al., 2010; Gassó & Torres, 2019; Li et al., 2010), and anthropogenic land activities, such as mining, grazing pressure, agricultural conversion, and infrastructural development (Marx & Hooper et al., 2018; McConnell et al., 2007). The relative contribution of each factor remains difficult to quantify but is essential for determining future trends in regional dust variability. Observational and modelling studies show that dust transport from SSA can take 4-5 days and 7-10 days to reach West Antarctica and East Antarctica, respectively, (Neff & Bertler 2015; Gassó et al., 2010), with increased transport efficacy in higher tropospheric levels due to stronger wind speeds (Shao, 2014).

Geochemical fingerprinting of dust in East Antarctica overwhelmingly point to a SSA origin, especially during the recent glacial period (Wegner et al., 2012; Delmonte et al., 2019, 2017; Gili et al., 2017; Bory et al., 2010). This technique involves the use of radiogenic isotopes (Nd, Sr, and Pb), elemental ratios, and rare earth elements in deposited dust to identify source regions; ice core dust geochemistry is compared to source-specific bedrock lithology. An example of geochemical signatures pointing to an SSA source for dust deposited in DML is shown in Fig. 2.6. While provenance studies suggest a dominantly SSA dust source for East Antarctica, there is significant overlap in the geochemical footprint of PSAs as exemplified in Fig. 2.6, leading to uncertainties in the interpretation of geochemical signatures (Vallelonga, 2014; Marx et al., 2018; Struve et al., 2020). Hence, multiple lines of evidence are required for

determining PSAs, and additional methods, such as particle dispersion modeling and particle size observations in ice cores, can complement the results of fingerprinting studies.

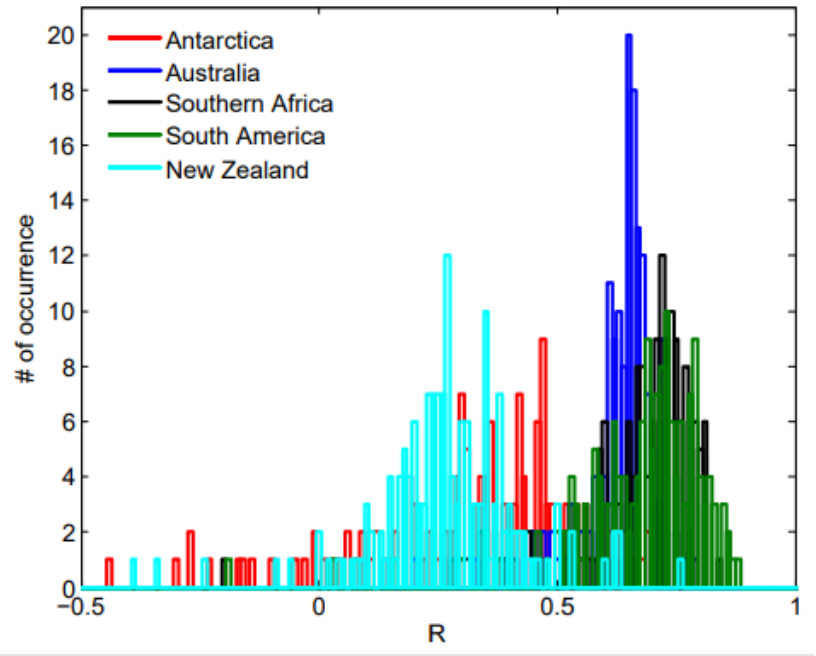

Figure 2.6 Example of geochemical fingerprinting data from Wegner et al. (2012). Histogram of the correlation coefficient R between the rare earth element pattern of each sample from the EDML core between 26,500 and 15,200 years BP (before present) and the mean rare earth element pattern of each PSA (red: exposed areas in Antarctica, green: South America, blue: south eastern Australia, black: southern Africa, light blue: New Zealand). Each ice sample from the glacial stage was correlated with the mean value from each PSA. From Wegner et al. (2012).

Findings from air-parcel trajectory modeling over the satellite era provide further evidence for a SSA provenance for East Antarctic dust for the present day, particularly in DML. Forward trajectories initiated in SSA reach coastal DML regions in approximately 7-10 days and exhibit persistent southward and eastward pathways mostly confined within the boundary layer typically within 1000-2000 m.a.s.l. (Neff & Bertler, 2015; Gassó et al., 2010; Li et al., 2010; Laluraj et al., 2020). Transport from SSA to the interior East Antarctic plateau is less frequent compared to other Antarctic regions due to the high topography. Despite a mean trajectory towards Antarctica, only about 8-20 % of SSA trajectories reach the continent, with an even smaller fraction (<

1 %; Fig. 2.7) arriving at the East Antarctic plateau (Neff & Bertler, 2015; Li et al., 2010). Compared to SSA, Australia-sourced trajectories dominate in Wilkes and Victoria Land due to proximity to the Australian continent and mostly travel in the free troposphere (Neff & Bertler, 2015).

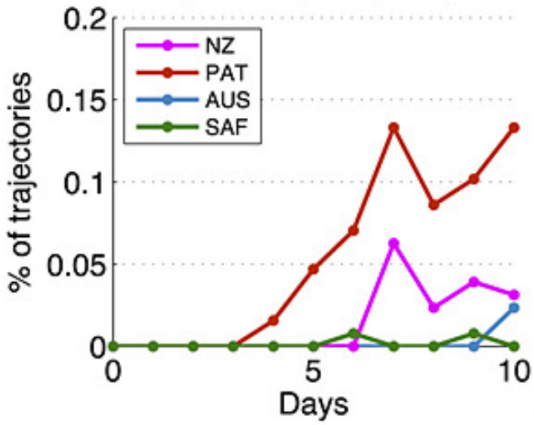

Figure 2.7 Air-parcel trajectory modelling from SSA to DML. Percent of 1979–2013 daily forward trajectories passing over EDML/ISOL-ICE site. From Neff & Bertler (2015).

Case studies of modern dust activity confirm dust particles reaching Antarctica from SSA (Li et al., 2010; Gassó et al., 2010). In late February 2005, a week-long series of dust plumes was tracked from Patagonia to Antarctica (Fig. 2.8). Satellite observations and model simulation consistently showed that most of the particles travelled within the atmospheric boundary layer reaching at least 1700 km east/southeast of the source region. Surface measurements of aerosol-induced radiation absorption at Neumayer Station, coastal DML, detected a corresponding increase during the same period (Gassó et al., 2010). Similarly, in June 2006, a dust plume was observed initially traveling east from Patagonia. The dust event was triggered by a low-pressure system over Drake Passage that intensified surface winds over SSA. The increased wind speeds produced dust emissions greater than 200 tons, and the resulting plume was entrained into the cyclonic circulation allowing dust

transport towards the coast of East Antarctica. Following this event, modeled surface dust concentrations at coastal DML regions were simulated to be ~1 μg m^{-3} compared to less than 0.1 μg m^{-3} prior to dust transport (Li et al., 2010). These dust events exemplify how dust emission and transport from SSA are usually episodic in nature rather than a continuous and sustained phenomenon.

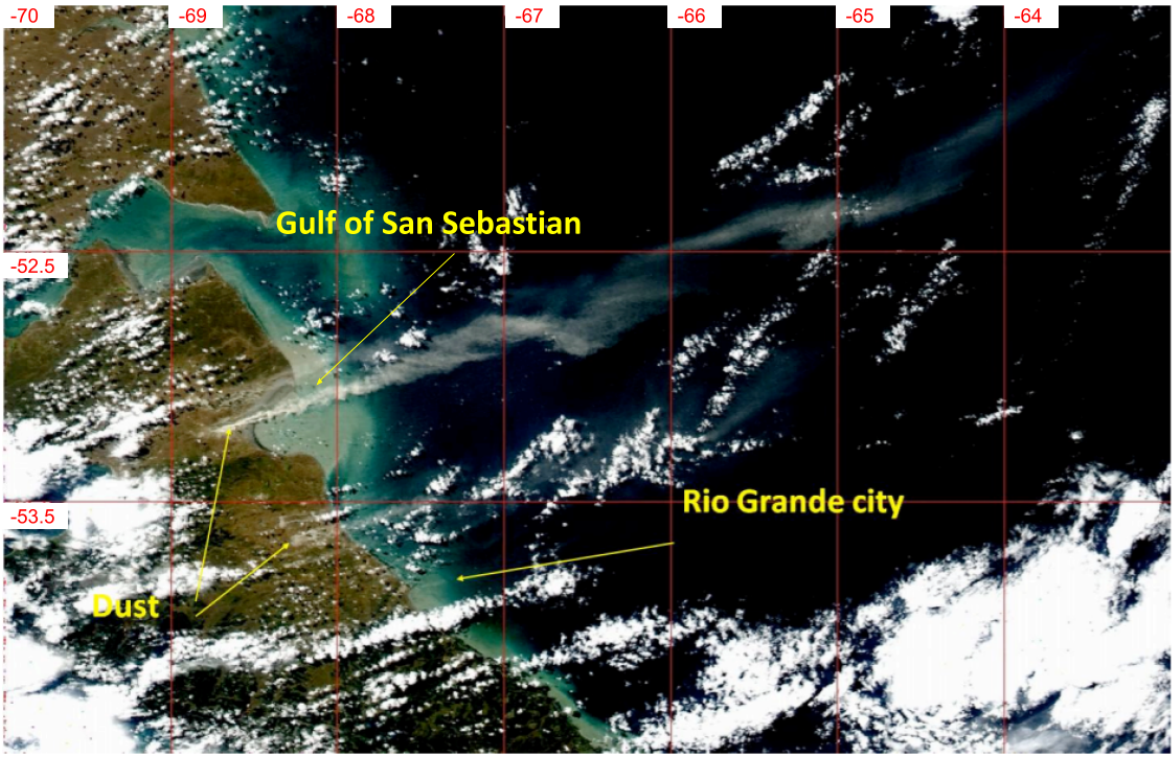

Figure 2.8 Dust Event in the Tierra del Fuego Island, Argentina (~53° S) detected by Aqua satellite on 26 February 2005. The largest plume is in the Gulf of San Sebastian and several minor plumes (some are not resolved in this image but they are visible by zooming in the full 250 m image) are located between San Sebastian and the city of Rio Grande, 100 km south. From Gassó et al. (2010).

Additionally, local Antarctic dust sources also contribute to dust deposition in Antarctic ice cores. The majority of the DML region is ice-covered but a few areas with exposed rock areas are present mostly running parallel to the coastline (Fig. 1.2). These regions comprise the sparse areas of ice-free landscapes, serving as potential local sources of dust to the DML region. Some examples of these nunataks include the Heimefrontfjella, Vestfjella, Basen, Plogen, and Fossilryggen (Delmonte et al., 2019). Dust emissions from these nearby ice-free regions are not expected to be as

abundant as in sub-Antarctic land areas since most of DML is ice-covered. Furthermore, the high altitude (> 2500 m.a.s.l.) of the East Antarctic plateau makes it difficult for local coarser dust (e.g., from warmer coastal Antarctic regions) to be transported to these areas due to the significant amount of uplift required (Koffman & Kreutz, 2014; Marx et al., 2018). However, the proximity of these ice-free regions to the ISOL-ICE site means that contribution from these local sources cannot be excluded, though the exact contribution is not well-known (Delmonte et al., 2019).

2.4 SH Hemispheric Scale Climate Variability

Local and regional atmospheric circulation patterns affecting dust transport to the ISOL-ICE site occur within the background variability of hemispheric-scale circulation/climate patterns. Hence, the next discussion gives an overview of the main modes of climate variability that are possibly associated with regional circulation patterns and consequent dust transport over the general region encompassing SSA, the South Atlantic, and DML.

Climate variability in the SH extratropics is dominated by fluctuations in the circumpolar westerly winds. Periodically, these westerly winds exhibit a repeating bi-modal pattern known as the Southern Annular Mode (SAM), describing an alternating poleward contraction (positive phase) and equatorward expansion (negative phase) of the westerly wind belt on weekly to monthly timescales (Rogers & van Loon, 1982; Thompson & Wallace, 2000). Alternatively, the SAM is defined as the leading mode in the Empirical Orthogonal Function (EOF) analysis of lower troposphere geopotential

heights, explaining ~20-30 % of month-to-month circulation variability in the SH extratropics. Each SAM polarity is associated with atmospheric pressure and zonal wind anomalies between around 40° and 65°S (Thompson & Wallace, 2000). During positive SAM, pressure decreases in the Antarctic region while increases in the SH mid-latitudes (Fig. 2.9). Consequently, this produces a stronger north-south pressure gradient and westerly wind tends to strengthen in the higher latitudes and weaken in the mid-latitudes. The opposite set of patterns is observed during negative SAM. Furthermore, synoptic storm activity follows the westerly wind belt, enhancing convection within the latitudinal band of influence (Fogt & Marshall, 2020).

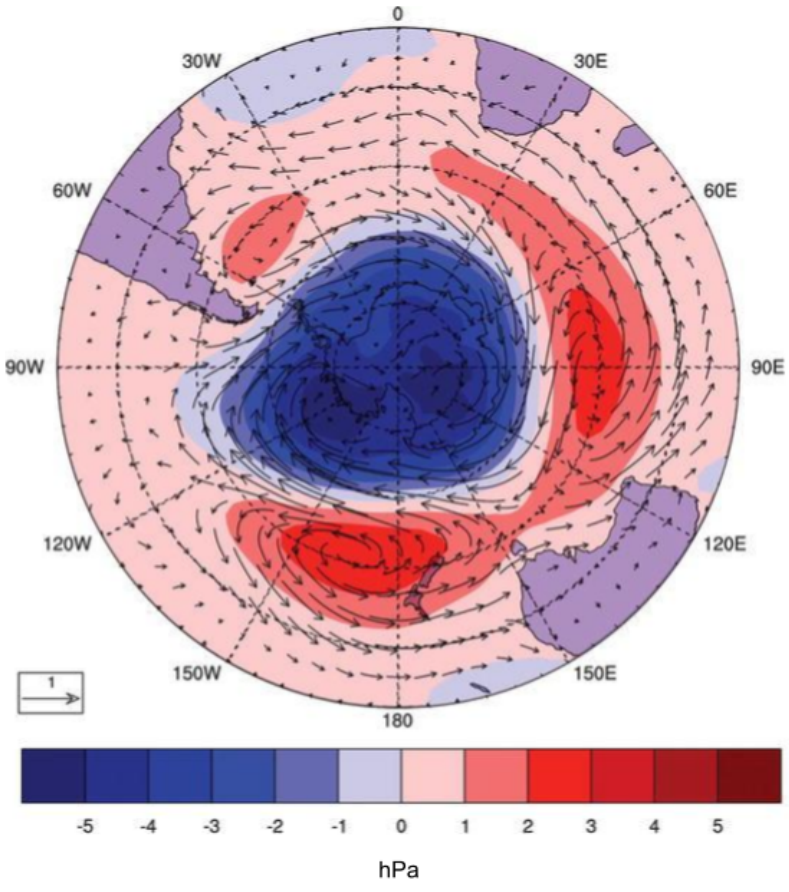

Figure 2.9 Regression on the SAM index of modelled surface wind vectors (1 m s^{-1} reference vector shown), superimposed on the corresponding SAM sea level pressure signal. The color bar indicates the sea level pressure signal in hPa. The regression values indicate the response of the variables to a 1 standard deviation positive SAM anomaly. From Gupta & England (2006).

The bimodal behaviour associated with SAM has been quantified through several indices. Some of the main metrics include the principal component analysis of geopotential heights (Z700 south of 20°S) from reanalysis products (Thompson & Wallace, 2000), the difference in mean sea level pressure (SLP) from station data between 40°S and 65°S (Marshall, 2003), and zonal mean pressure difference between two nodes (40 and 65°S) derived from gridded datasets (Gong & Wang, 1999). In general, station-based indices have the advantage of avoiding issues related to spurious changes in the quality of reanalysis products before and after the assimilation of satellite sounder data in 1979. However, gridded datasets have a larger spatial coverage and more uniformly distributed data points compared to weather stations (Fogt & Marshall, 2020).

Aside from the latitudinal shift in the circumpolar westerlies, variations in SAM also influence katabatic winds over Antarctica. Strengthening of the circumpolar westerlies and weakening of polar easterlies occurs during the positive phase of the SAM. Katabatic flow and associated downward air mass mixing are also reduced with lower than normal pressure over the Antarctic interior and higher than normal pressure over the Southern Ocean, thereby reducing the interior-to-coast pressure gradient (Broeke & Leipzig, 2003a). While reduced downward mixing suggests less deposited dust, stronger westerly winds are more conducive for dust transport. The competing effects of these two patterns on dust transport warrants further investigation. The opposite set of patterns ensues from negative SAM conditions.

Since approximately the 1970s, the SAM has been trending towards a more positive state during the austral summer. This upward trend has been primarily attributed to an enhanced meridional temperature gradient associated with stratospheric ozone loss and greenhouse gas (GHG) increases (Arablaster et al., 2011; Simpkins & Karpechko, 2012). Since ozone is a key absorber of ultraviolet solar radiation in the stratosphere (Wallace & Hobbs, 2006), ozone depletion induces cooling in the upper atmosphere through a decrease in absorbed shortwave and emitted longwave radiation pronounced during austral spring (Thompson & Solomon, 2002). This thermal anomaly propagates downward into the troposphere most actively in late spring/early summer as the polar vortex breaks down, making conditions conducive for coupling between the stratosphere and troposphere. Therefore, the tropospheric response is most evident during summer (Thompson & Solomon, 2002; Gillet & Thompson, 2003). For GHG warming, temperatures increase in the tropics while relatively minimal large-scale change occurs in the SH high latitudes. This uneven warming pattern steepens the meridional temperature gradient and induces a positive SAM trend (Abram et al., 2014; Bracegirdle et al., 2020). Within the last two decades, ozone recovery has started counteracting the effect of GHG warming, thereby reducing the rate of the positive SAM trend during the summer (Solomon et al., 2016).

In addition to SAM, the El Niño- Southern Oscillation (ENSO) (Yuan et al. 2018, Ding et al., 2012) and the Pacific Decadal Oscillation (PDO) (Mantua et al., 1997; Henley, 2017) are also important climate patterns affecting circulation patterns over SSA, South Atlantic, and DML. From a qualitative perspective, ENSO and the PDO have a similar signature in the tropical Pacific expressed as anomalous sea surface

temperatures and troposphere atmospheric pressure in the western and eastern regions of the basin (Wills et al., 2018; Henley, 2017). During neutral conditions, the eastern equatorial Pacific has cooler waters and higher atmospheric pressure compared to the western Pacific (Fig. 2.10). In contrast, the western equatorial Pacific is considered a warm pool with relatively lower atmospheric pressure. During an El Niño or positive PDO phase, this configuration is reversed, while during a La Niña or negative PDO phase, it is enhanced (Yang et al., 2018; Collins et al., 2010). Though similar, ENSO and PDO operate on different timescales, the former being ~2-7 years and the latter 20-30 years (Wang et al., 2017; Newman et al., 2016). This multi-decadal periodicity of the PDO is related to storage of thermal anomalies in deep ocean layers especially in the north Pacific. PDO is also thought to represent multiple basin-wide processes, with ENSO being a key contributor to its variability (Newman et al., 2016).

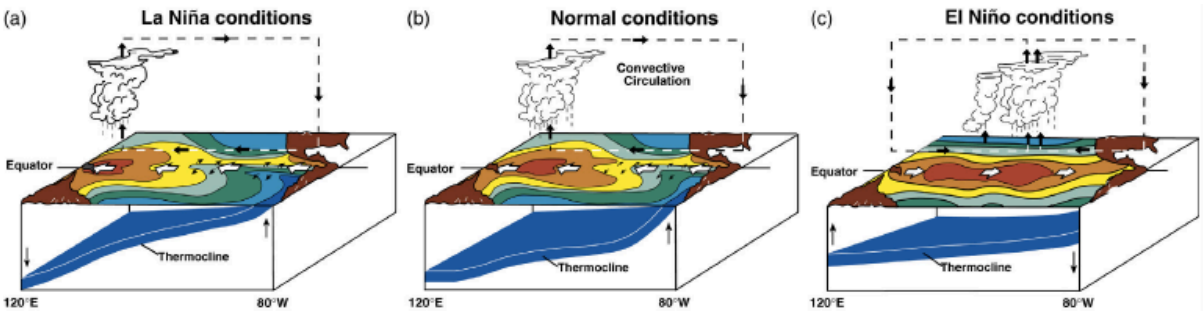

Figure 2.10 Atmospheric and oceanic conditions during a) La Niña, b) Normal state, and c) El Niño. Colors on the surface indicate SST from warm (red) to cold (blue). The black arrows indicate the convective circulation associated with each phase, while the white arrows denote the surface ocean current. Changes to the thermocline (delineating warm surface ocean layer and cold deep ocean layer) are shown in the bottom of each plot. From Hartmann (2016).

Because of its strong association with SSTs and surface pressure, ENSO is typically measured by spatially-averaged SST anomalies called Niño indices and sea level pressure differences in the western versus eastern tropical Pacific. The multiple SST-based Niño indices (e.g., 1+2, 3, 3.4, 4) span different segments of the equatorial

Pacific, collectively covering nearly the entire tropical Pacific (Wang et al., 2017). Sea level pressure patterns in the western and eastern equatorial Pacific are captured by the Southern Oscillation Index (SOI; National Oceanic and Atmospheric Administration Climate Prediction Center), measuring the observed pressure difference in Darwin, Australia versus Tahiti. Alternative ENSO metrics include outgoing longwave radiation (Hartmann, 2016), zonal winds, and 20°C ocean isotherm (Wang et al., 2017).

In terms of metrics, the PDO was first described as the leading principal component of SSTs in the North Pacific poleward of 20°N (Mantua et al., 1997). Subsequent versions of this index mostly involve additional low pass filtering techniques, such as over 6 (Zhang et al., 1997) and 13 (Power et al., 1999) year periods. Principal component PDO indices are thus the most widely used, but other metrics exist. For instance, a more recent index, termed the Interdecadal Pacific Oscillation, utilises a box-based linear sum method to produce the linear sum of deseasonalised mean SST anomaly over three separate regions encompassing the tropical Pacific and South Pacific in addition to the more traditional North Pacific region (Henley et al., 2015).

Despite being located in the SH extratropics, both the circumpolar westerlies and the SAM are also influenced by tropical variability primarily related to the ENSO and PDO. During ENSO phases, anomalous atmospheric and oceanic patterns result in the displacement of tropical convection that triggers atmospheric Rossby waves (Wang et al., 2017; Yang et al., 2018). Known as the Pacific South American pattern

in the SH (Mo & Higgins, 1998), these wave trains of alternating low- and high-pressure systems typically follow a great circle path from the north-eastern region of Australia to the southern tip of South America (Fig. 2.11). In the process, the anomalous pressure systems perturb the circumpolar westerly winds and influence SAM behaviour (Ding et al., 2012; Yuan et al., 2018; Clem et al., 2020). In particular, La Niña (El Niño) phases favour positive (negative) SAM (L'Heureux & Thompson, 2006; Fogt et al., 2011). Moreover, the pressure systems are associated with cyclonic and anticyclonic activity that alter regional wind flow patterns along the Rossby wave path. Consequently, atmospheric rivers and anomalous precipitation patterns may ensue, as exemplified by the unusual heavy rainfall event in the Chilean Atacama Desert in March 2015 triggered by anomalous tropical convection (Rondanelli et al., 2019). For PDO phases, the same set of relationships hold since positive (negative) PDO phases tend to coincide with more pronounced El Niño (La Niña) conditions (Verdon & Franks, 2006).

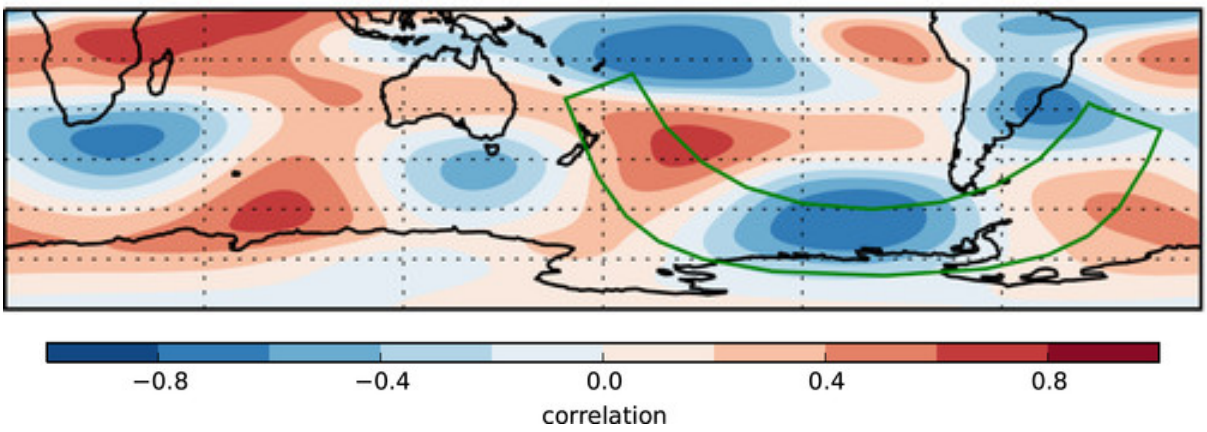

Figure 2.11 The Pacific South American pattern as identified through the leading empirical orthogonal function of the monthly 500-hPa zonal streamfunction anomaly from the ERA-Interim reanalysis over the period 1979–2014. The green lines indicate the search region of interest (the "Pacific South American sector") and the data are presented as the correlation of the corresponding principal component with the original field. From Irving & Simmonds (2016).

The impact of ENSO over the greater SSA, Antarctic Peninsula, and DML region is captured by a mode of regional climate variability known as the Antarctic Dipole (AD). The AD describes the dominant interannual variability in sea ice extent and surface air temperature over the eastern Pacific and Atlantic sectors of Antarctica. It is strongly associated with pressure and circulation systems in the SSA, Antarctic Peninsula, and DML region. Empirical Orthogonal Function (EOF) analysis reveals primary and secondary leading modes expressed as a stationary wave and an eastward propagating wave, respectively, largely contained within the mentioned Antarctic sectors (Yuan & Martinson 2001). The pole/circulation centres are located in the western Amundsen Sea and the central Weddell Gyre, maintained by mean meridional heat flux from the Ferrel Cell and anomalous regional circulation associated with paired high- and low-pressure systems (Yuan & Martinson 2001; Yuan, 2004). The proximity of eddy activity to dust source areas in SSA, therefore suggests a strong association between poleward dust transport and the AD. Tropical forcing modulates AD variability through stationary atmospheric Rossby wave trains (Yuan & Martinson 2001; Yuan, 2004). Specifically, these Rossby waves produce anticyclonic circulation over the Pacific pole of the AD during an El Niño event, resulting in increased poleward wind flow in the southeast Pacific and weaker poleward flow in the south Atlantic (Fig. 2.12). These changes to mean meridional flow are associated with the modulation of the strength of the Ferrel Cell. Furthermore, the high-pressure system over the southeast Pacific is accompanied by a reduction in cyclonic activity, while more cyclones develop over the South Atlantic. The opposite pattern occurs during La Niña conditions (Yuan, 2004). The effect of this tropical teleconnection on dust transport could be twofold. Firstly, poleward dust flux increases (decreases) with stronger (weaker) poleward wind flow. Second, wet deposition could also be enhanced

(diminished) due to more (less) moisture and precipitation directed toward the continent. The relative influence of these two factors will determine the overall effect on dust transport.

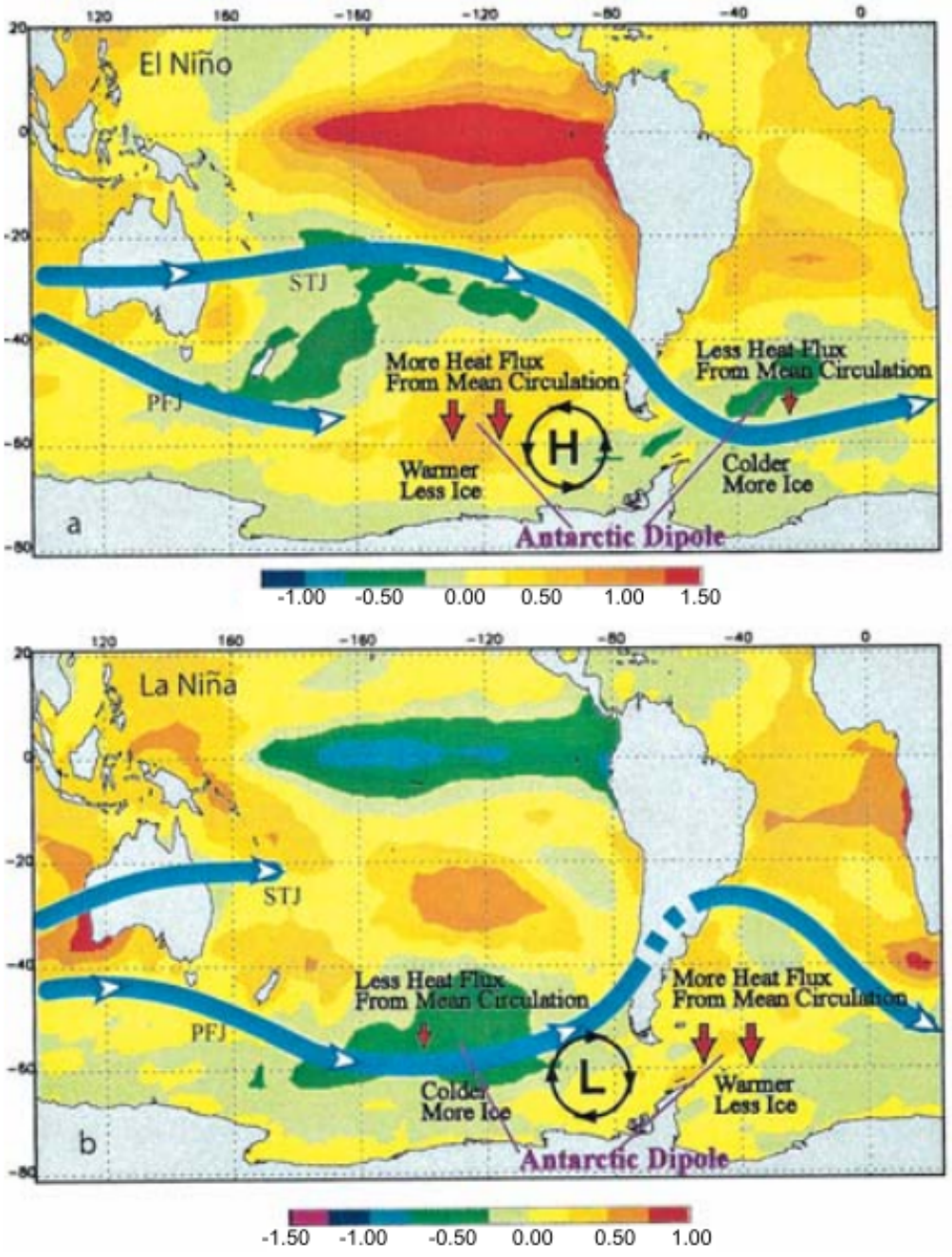

Figure 2.12 SST anomalies (°C) showing interaction between ENSO and the Antarctic Dipole during (a) El Niño conditions, and (b) La Niña conditions. Schematic jet stream (STJ; subtropical jet, and PFJ; polar front jet), persistent anomalous high and low pressure centres, and anomalous heat fluxes due to mean meridional circulations are marked in corresponding SST composites. From Yuan (2004).

The PDO has been linked to variability in cyclonic activity over the Drake Passage. The recent negative PDO phase between 1999-2014 coincides with increased cyclonic activity over the Drake Passage, especially over austral summer (Turner et al., 2016). This association is further explained in Clem et al. (2019), wherein the negative PDO phase induces anomalous sea surface temperature warming over the tropical western Pacific thereby inducing Rossby wave trains that enhance cyclonic activity over Drake Passage. Increased cyclonic activity in this region possibly affects long-range transport of dust from SSA to DML due to its proximity to SSA dust sources.

2.5 Dust deposition in the Atlantic sector of Antarctica over the last century and suggested causes

Increased dust deposition has been observed in several Antarctic ice cores in the Atlantic sector over the past century (Fig 1.1). The IND-25/B5 core in coastal DML shows three stepwise increases during 1905-1929, 1930-1979, and 1980-2005 with average dust fluxes of 0.83, 4.7, and 12.88 mg m^{-2} $year^{-1}$, respectively (Laluraj et al., 2020). The increase in dust deposition is attributed to enhanced aridity in SSA that is related to the in-phase relationship of ENSO and PDO. Additionally, the shift to a more positive SAM since the 1980s has likely resulted in stronger wind speeds and more favourable wind flow direction for long-range transport of dust from SSA to coastal DML. In the Antarctic Peninsula, the JRI core reveals doubling of dust influx over the last century, increasing from 12 mg m^{-2} $year^{-1}$ between 1832-1900 CE to 27 mg m^{-2} $year^{-1}$ between 1960-1991 (McConnell et al., 2007). This increase is thought to

have been caused by increased desertification in SSA due to land-use changes and global warming. At the WAIS Divide, dust flux has been shown to increase from background levels of 4 mg m^{-2} $year^{-1}$ to 10-25 mg m^{-2} $year^{-1}$ between 1850-2002 (Koffman et al., 2014). It is suggested that this change is due to latitudinal shifts in the circumpolar westerlies that affect long-range dust transport particularly from SSA. While these dust records are consistent in showing an overall increase in Antarctic dust deposition over the last century, there is significant variability between the dust trends in these ice cores within the last century. This suggests that the dust deposition at each site is caused by different site-specific factors, such as varying regional circulation patterns.

3. DATA AND METHODS

The methodology employed in this study is divided into three parts: 1) ice core dust record analysis, 2) dust dispersion modeling, and 3) dust-climate relationships. The first section investigates the temporal variability of millennial scale Antarctic dust deposition records from ice cores focusing on the last century. The second section models dust transport to DML in order to investigate the key dust transport pathways and potential source areas to DML. Lastly, to understand dust-climate relationships over the satellite era, reanalysis data (1979-2017) is used for correlation analysis between dust particle size at the ISOL-ICE site and large-scale atmospheric circulation/climate patterns. Each of these parts are discussed in detail in this chapter.

3.1 Ice Core Data

3.1.1 ISOL-ICE ice core

3.1.1.1 Ice core drilling and dust measurements

The primary dataset used in this study is taken from the new ice core drilled under the National Environment Research Council (NERC) funded project “Isotopic Constraints on Past Ozone Layer in Polar Ice” (ISOL-ICE). The ice core drilling, laboratory processing, dating, and data production were done by Winton et al. (2019). While this thesis focuses on the analysis of the dust dataset as described in section 3.1.1.3 to 3.1.3, the ice core retrieval and lab processing methodology employed by Winton et al. (2019) is described next.

Ice core drilling occurred in January 2017 using a shallow electro-mechanical drill to retrieve a 120 m deep and 105 mm diameter ice core. The site is located ~1 km from the European Program for Ice Coring in Antarctica (EPICA) Dronning Maud Land (EDML) deep ice core drilling location. The ice core was bagged into 80 cm long sections and shipped frozen to the British Antarctic Survey (BAS) in Cambridge, United Kingdom. At the BAS ice core facility, a bandsaw was then used to cut a 32 x 32 cm stick (Fig. 3.1) for Continuous Flow Analysis (CFA) including dust concentration and particle size analysis by Laser Particle Detection (LPD); both methods are briefly discussed next.

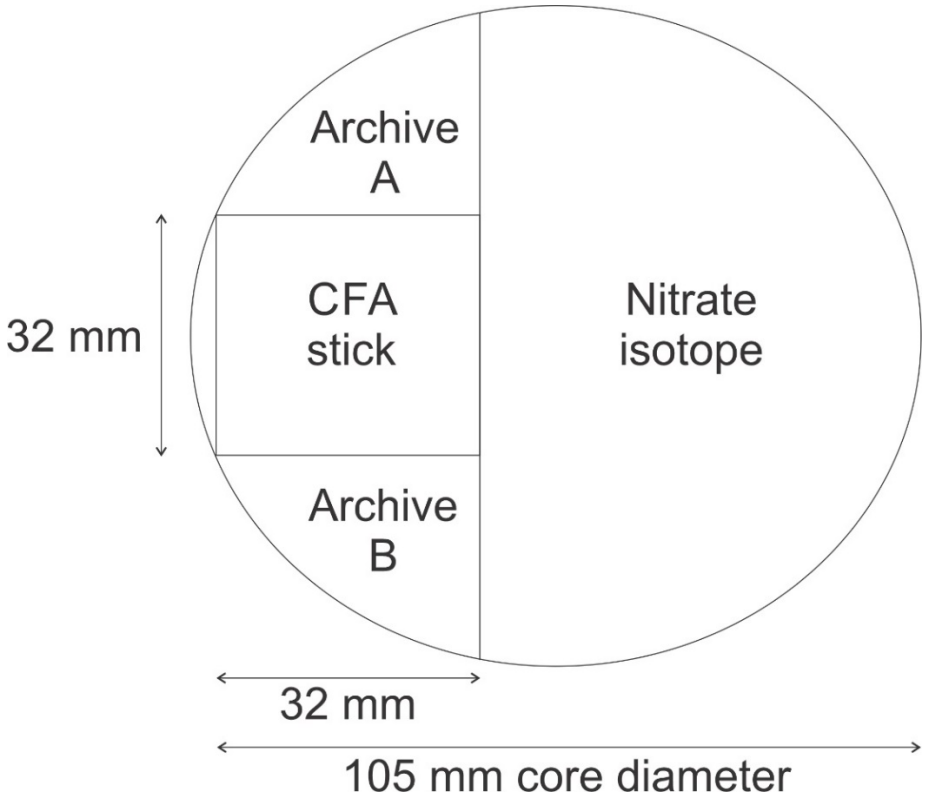

Figure 3.1 Cross section of the ISOL-ICE ice core cut plan. Not to scale. From data repository by Winton et al. (2019).

The stick was melted using the CFA system at BAS, consisting of a melting unit, a flow system for gas and water, and several sets of instrumentation for different analyses (Grieman et al., 2022). The melting unit is comprised of gold-plated copper

melt head with 2 rings separating the inner and outer layers of the melted core, and to avoid sample contamination, only the inner section of the core was utilised for dust analysis. Melted liquid from one end of the ice core is channelled through a flow pipe system allowing for continuous high-resolution sampling of the core.

Insoluble particles were then measured through LPD (Abakus, Fa. Klotz, Bad Liebenzell, Germany). LPD utilises the attenuation of transmitted light to make high spatial resolution measurements of particles flowing continuously through a liquid (Fig. 3.2; Ruth et al., 2002; Wegner et al., 2015). Shadowing and scattering of light from the passage of a particle results in a negative peak in the beam signal (Ruth et al., 2002). The peaks are counted to give the particle number concentration, and the magnitude of attenuation is indicative of the size of the particle, therefore allowing for sorting of particles according to size (Ruth et al., 2003). For the ISOL-ICE core, the LPD system was configured to measure insoluble particles between 0.9 and 50 μm in diameter in 32 size bins. The measured volume concentration was converted into mass concentration assuming a spherical particle density of 2.5 g cm^{-3}.

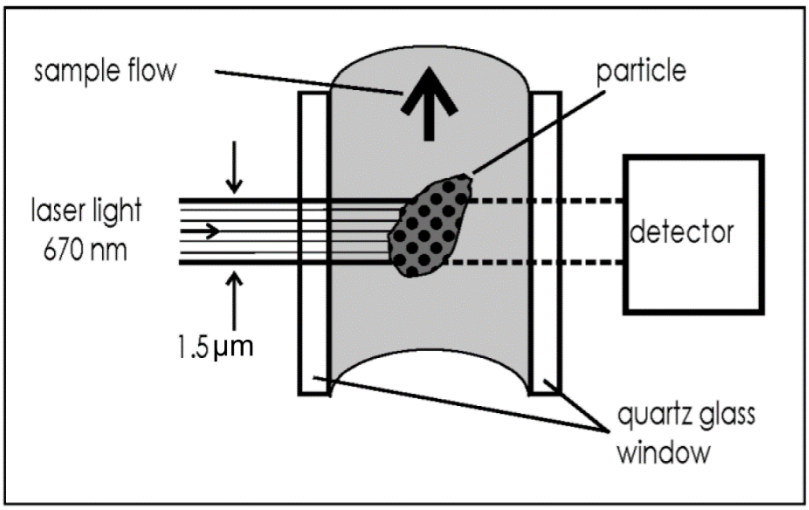

Figure 3.2 LPD schematic. From Ruth et al. (2002).

Sodium concentrations in the core were measured using Inductively Coupled Plasma Mass Spectrometry (ICP-MS; 7700 series, Agilent). The ICP-MS method utilises high-temperature plasma to atomise and ionise acid-digested/leached samples. The generated ions are then separated by a mass-analyser according to mass-charge ratio and subsequently measured using a detector (Barbante et al., 1997; Wilschefski & Baxter, 2019). The measured sodium concentrations underwent quality control through a certified reference material (ERM-CA408 simulated rainwater standard; Sigma-Aldrich) yielding an accuracy of 94 % and precision of 10 %.

3.1.1.2 Ice core dating

The ice core was dated by counting annual layers based on sodium concentrations as described in Winton et al. (2019). Briefly, multi-year aerosol observations from Kohnen Station show a narrow seasonal minimum in sodium concentrations in austral summer and a broad peak in late winter/spring. The observed seasonal pattern of sodium is related to variability in emitted sea salt aerosols that are influenced by seasonal sea ice formation (Weller & Wagenbach, 2007). Where possible, annual markers were positioned where the seasonal sodium minimum coincides with δD (deuterium) maximum in summer (Winton et al., unreleased data). Otherwise, markers were based solely on sodium minima. Additionally, known volcanic eruptions were used as tie-points to further constrain the age-depth model (Cole-Dai & Mosley-Thompson, 1999; Zielinski et al., 1994; Langway et al., 1995; Traufetter et al., 2004). Snow accumulation rates were derived from the density and annual layer thickness of the core, and plastic deformation associated with thinning deeper ice layers was accounted for by using the thinning model of Nye (1963).

3.1.1.3 Ice core data processing

To analyse dust trends, dust mass concentration and flux are investigated. The dust mass concentration is a measure of the amount of dust within a specific volume of melted ice, while the dust flux is calculated by multiplying dust mass concentration and the water equivalent accumulation rate (i.e., precipitation rate) at the site. The dust flux provides additional information regarding depositional processes at the ice core site.

3.1.1.4 Particle size distribution

In this study, particle sizes are operationally defined as fine particles (1-5 μm), coarse particles (5-10 μm), large coarse particles (10-50 um), and total particles (0.9-50 um).

Dust particle size distribution (PSD) is explored using particle volume-size distribution following Delmonte et al. (2002), Wegner et al. (2015), and Koffman et al. (2014). The volume-size distribution is parameterised by fitting a lognormal function as used by Delmonte et al. (2002):

$$dV / d(\ln D) = V / \left[(2\pi)^{1/2} \ln \sigma_g \right] * \exp\left[-0.5 \left(\ln (D/D_v) / (\ln \sigma_g)\right)^2 \right] \qquad (2.1)$$

where V is the total volume, D_v is the modal diameter, and σ_g is the geometric standard deviation. Equation 2.1 originates from the change in the number of particles relative to the logarithmic change in the particle radius in lognormal form:

$$dN / d(\log r) = 0.434N_0 / [(2\pi)^{1/2} \log \sigma_g] * \exp[(\log r - \log r_n)^2 / (2 \log^2 \sigma_g)] \quad (2.2)$$

where N_0 is the number of particles per unit volume, r_n the mean radius, and σ_g the geometric standard deviation. A lognormal fit is chosen as this parameterisation was used for the EDML ice core, which was drilled close to the ISOL-ICE site. Applying equation 2.1 to the entire ISOL-ICE dust record to determine the particle size mode resulted in a poor lognormal fit due to low concentration of particles. This was also experienced in low concentration Holocene dust in the EDML core as noted by Wegner et al. (2015). The low number of particles in most intervals of the core precludes resolving a continuous PSD throughout the entire ISOL-ICE record. Rather, selected examples of lognormal-fitted volume-size distribution displaying a good fit are presented in the Results chapter.

In addition to volume-size distribution, the coarse particle percentage (CPP), a proxy of PSD (Delmonte et al., 2004), was calculated following the methodology for EDML ice core (Wegner et al., 2015). For the EDML core, CPP was defined as the volume fraction of coarse particles (> 2 μm) divided by the total volume fraction of particles (> 1 μm). As the upper limit of the size bins is not explicitly mentioned in Wegner et al. (2015), the upper boundary in this study is set to 5 μm following Lambert et al. (2008), which was referenced in Wegner et al. (2015). Hence, CPP in this study

is defined as the volume fraction of 2-5 μm particles divided by the total volume fraction of 0.9-5 μm particles.

3.1.1.5 Change point analysis

Change point analysis is utilised to investigate significant shifts in dust mass concentration and CPP in the ISOL-ICE dust record. The specific implementation of the change point algorithms used in this study are based on the MATLAB algorithm *findchangepts* (Killick et al., 2012; Lavielle, 2005). The change points are detected based on changes in the mean. The detection algorithm iterates over subsections of the dataset and fits a mean line on the data. The optimal change points are then selected based on the combination of points that minimises the residual fitting error. The detected change points pinpoint possible transition periods that can be further investigated. Additionally, change points also divide the time-series into unique periods based on similar means.

3.1.2 Other published Antarctic dust ice core records

The available Antarctic ice core dust records spanning the last millennium/century are compiled and listed in Table 3.1 and described in section 2.5. The selection of ice core dust records is based on 1) temporal coverage over the last century with at least annually-resolved data, 2) proximity to SSA (serving as a PSA), and 3) data availability. The locations of the ice cores were shown previously in Fig. 1.2. As discussed in section 2.1.1, insoluble particles are used as a proxy for dust for most of the ice cores analysed in this study except for the James Ross Island ice core,

where aluminium is used as the elemental proxy for dust. Aluminium is almost exclusively sourced from aluminosilicate minerals of crustal origin, and dust concentrations have been derived from aluminium content considering the average amount in soils — 6-8 % (McConnell et al., 2007; Pye, 1987).

Table 3.1 Ice core data used in this study.

Ice Core	Elevation (m.a.s.l.)	Temporal Coverage	Resolution	Dust proxy	Method	Source
ISOL-ICE	2,892	668-2017 ± 3 CE	Sub-annual	Insoluble particles	CFA-LPD	Winton et al., 2019
IND-25/B5	1,300	1905-2005 ± 2 CE	Annual	Insoluble particles	Coulter Counting	Laluraj et al., 2020
JRI	1,600	1832-1991 ± 1 CE	Sub-annual	Aluminium concentration	ICP-MS	McConnell et al., 2007

*Abbreviations – ISOL-ICE: Isotopic Constraints on Past Ozone Layer in Polar Ice; IND-25/B5: Indian-25/B5; JRI: James Ross Island; CFA-LPD: Continuous Flow Analysis-Laser Particle Detection; ICP-MS: Inductively Coupled Plasma Mass Spectrometry.

3.1.3 Data Smoothing

The dust datasets are smoothed using either low pass filtering or annual averages. Given the high-resolution of the ISOL-ICE dust record, low-pass filtering using the Butterworth filter (Butterworth, 1930) is utilised to reduce noise in the dust mass concentration, flux, CPP, and snow accumulation rate data following Koffman et al. (2014), which featured a similar high-resolution dust record. The average sampling rate of the filter is ~1.7 days for the entire dust record, and the cutoff frequencies are specified in Fig. 4.4, 4.5, and 4.6. However, for the intercomparison of dust records from different ice cores, annual averages are used given the lowest resolution is annual average data from the IND-25/B5 core (Table 3.1).

3.2 Dust Dispersion Modelling

3.2.1 Model exploration and testing

This study explores several Lagrangian models to simulate dust transport to the ISOL-ICE site. In general, Lagrangian models are used to investigate transport of particles, gases, or air-parcels in a fluid medium, such as the atmosphere. This type of model tracks chemical species, particles or air-parcels during transport producing spatial trajectories (in contrast to the Eulerian models that focuses on fixed points in space in which substances can flow through) (Stohl et al., 1998). Useful information can be extracted from Lagrangian models, such as 3-dimensional transport pathways, species dispersion, and species removal processes. A summary table of the models explored to investigate dust back trajectories from the ISOL-ICE site are provided in

Table 3.2. The initial selection of models is based on the review by Bowman et al. (2013). For this study, Lagrangian particle dispersion models are preferred over Lagrangian air-parcel models as the former provide a more realistic representation of particle transport, especially with some dispersion models factoring in particle size (e.g., Pisso et al., 2019). The drawback is that dispersion models are generally more computationally expensive than air-parcel models and hence the greater popularity of the latter for Antarctic studies (e.g., Neff & Bertler, 2015, Laluraj et al., 2020, Markle et al., 2012). Based on model capabilities, accessibility, and support, the selection is narrowed down to Flexpart (Flexible particle dispersion model; Stohl et al., 2005) and HYSPLIT (Hybrid Single-Particle Lagrangian Integrated Trajectory model; Draxler & Hess 1998). Both models can simulate particle dispersion and are readily accessible for download online.

Table 3.2 Explored Lagrangian transport models.

Model*	Developer	Particle Dispersion	Stochastic Turbulence	Input Meteorological Data
Flexpart	NILU (Norway)	Included	Included	ERA-Interim (0.75° horizontal grid resolution, 6-hourly)**, NCEP GFS (0.25° horizontal grid resolution, 6-hourly)**
NAME	UK Met Office	Included	Included	Met Office Unified Model (1.5-300 km horizontal grid resolution, varying temporal resolution), ERA-Interim
HYSPLIT	NOAA	Included	Included	NCEP GFS, ERA-Interim
Lagranto	ETH Zurich	Not included	Not included	ERA-Interim
Stilt	Multiple	Not included	Included	NCEP GFS, ERA-Interim

*Abbreviations – ERA-Interim: European Centre for Medium-Range Weather Forecasts Interim Reanalysis, NCEP GFS: National Centers for Environmental Prediction Global Forecast System, Flexpart: Flexible particle dispersion model (Stohl et al., 2005), NILU: Norwegian Institute for Air Research, NAME: Numerical Atmospheric dispersion Modelling Environment (Jones et al., 2007), UK Met: United Kingdom Meteorological Office, HYSPLIT: Hybrid Single-Particle Lagrangian Integrated Trajectory model (Draxler & Hess 1998), NOAA: National Oceanic and Atmospheric Administration, Lagranto: Lagrangian analysis tool (Wernli & Davies, 1997), ETH Zurich: Eidgenössische Technische Hochschule Zürich, Stilt: The Stochastic Time-Inverted Lagrangian Transport Model (Lin et al., 2003).
**Same resolutions for other rows.

To test the computational requirements and comparability of each model, trial simulations of 14-day back trajectories were carried out for the intended geographic study domain (south of 30°S) and over an arbitrary common time period (March 15 – 31, 2010) for each model. The models are forced by ERA-interim reanalysis, and 14 days simulates the typical maximum lifetime of tropospheric aerosols (Kok et al., 2012). Further details about the model configuration and input meteorological data are discussed in section 3.2.3. The results of the test runs are illustrated in Fig. 3.3 and show that both models generate trajectories that follow the same general circulation patterns. Flexpart is ultimately chosen as for this study due to the parameterisation of dust particles and dispersion modeling capabilities that allow tracking plume trajectories (instead of a single particle/parcel), emission sensitivity estimates, and calculating wet/dry deposition values at a particular site (Pisso et al., 2019).

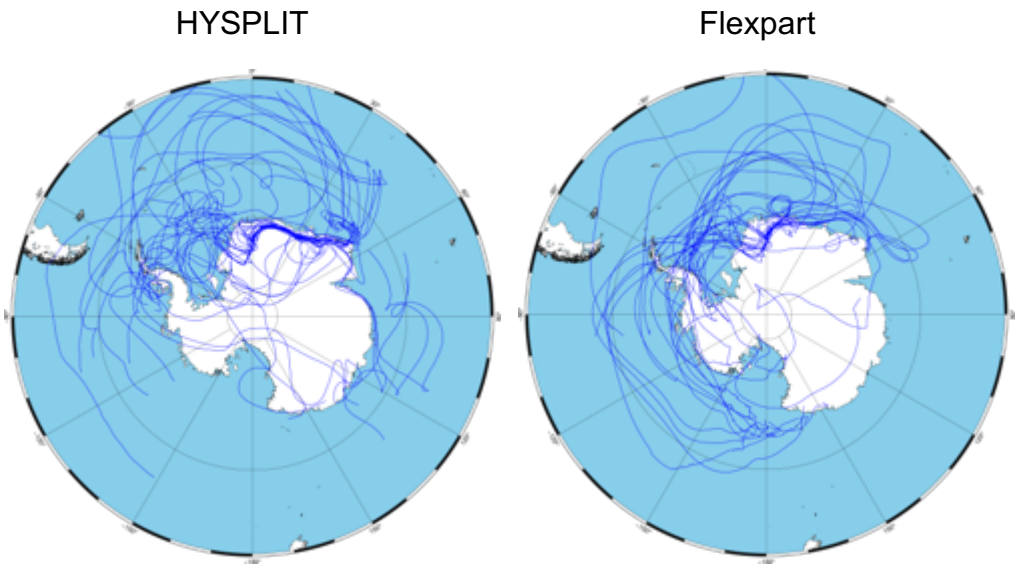

Figure 3.3 Example of trial 14-day trajectory simulations from (left) HYSPLIT and (right) Flexpart run from March 15 to 31, 2010, using the same meteorological input (ERA-interim).

3.2.2 The Flexpart model

The Flexpart model features several state-of-the-art particle transport and dispersion capabilities. The following discussion provides an overview of the model and summarises key model features important for this study. Further details about the model can be found in Pisso et al. (2019) and Stohl et al. (1998 & 2005).

Particle transport and diffusion in Flexpart follows the “zero acceleration scheme”:

$$X(t + \Delta t) = X(t) + v(X, t)\Delta t, \quad (2.3)$$

where X is the position vector, t is time, Δt is time increment, and $v=v_g + v_t + v_m$ describing the wind vector consisting of the grid-scale wind v_g, the turbulent fluctuations v_t and the mesoscale wind fluctuations v_m. The vector position obtained by the zero-acceleration scheme is corrected whenever possible by the Pettersen scheme for grid-scale winds (Stohl et al., 2005).

Particle dispersion in Flexpart tracks plume clusters based on particle quantity and accounts for tracer filaments generated by dispersion in the atmosphere (Stohl et al., 2005; Ottino, 1989). This feature is typically absent or not treated systematically in air-parcel trajectory models as air-parcel models simulate a single infinitesimally small particle rather than numerous particles in the atmosphere. Plume clusters present a more accurate depiction of aerosol transport in the atmosphere since particulate

plumes are deformed by atmospheric flow during transport resulting in multiple strands of elongated trajectories. Another notable benefit of this approach is the consideration of convection and turbulence. Particle dispersion is significantly affected by vertical mixing processes especially in the atmospheric boundary layer. Plumes traveling within the atmospheric boundary layer are subject to growth over time due to convection and turbulence. Again, this consideration is not well-represented when simulating only a single particle/parcel in the atmosphere (Stohl et al., 2002).

Lastly, Flexpart also includes wet and dry deposition of particles, a feature which is typically omitted in air-parcel trajectory models (Stohl et al., 2005). Removal from wet deposition follows an exponential decay process over time *t* (McMahon & Denison, 1979)

$$m(t + \Delta t) = m(t) \exp(- \lambda \Delta t), \quad (2.4)$$

where m is particle mass and λ is the scavenging coefficient, which varies depending on whether the particles are scavenged below or in-cloud. The scavenging coefficient is dependent on the sizes of both the particle and falling hydrometeors and is described in further detail in Grythe et al. (2017). Dry deposition in flexpart takes the form of:

$$v_d(z) = [\, r_a(z) + r_b + r_a(z) r_b v_g \,]^{-1} + v_g \,, \quad (2.5)$$

where r_a is the aerodynamic resistance between height z and the surface, r_b is the quasi laminar sublayer resistance, r_c is the bulk surface resistance, and v_g is the gravitational settling velocity taken from (Slinn, 1982):

$$v_g = (g p_p d^2_p C_{cun}) / (18\mu) , \quad (2.6)$$

where g is the gravitational coefficient, p_p and d_p are the particle density and diameter, respectively, μ the dynamic viscosity of air, and C_{cun} the Cunningham slip-flow correction. The dynamic viscosity of air is computed as a function of temperature following the formula in Sutherland (1893). Dry deposition in the model is strongly dependent on the particle size, given the exponential relationship between settling velocity and particle diameter. Flexpart assumes a lognormal size distribution for particle mass, and the mean diameter can be specified by the user (Stohl et al., 2005).

Transport and dispersion computations in Flexpart can be run backwards in time. The process is the same as in forward simulations except that the receptors are now treated as the sources and vice versa, and the wind vectors are reversed. This modeling capability is a powerful tool for investigating source-receptor relationships. While forward modeling outputs concentration values of particles, in reverse mode, the model produces source-receptor relationships (Seibert & Frank, 2004), also called source-receptor sensitivity (Wotawa et al., 2003), or simply emission sensitivity. The theoretical formulation of source-receptor relationships in Seibert & Frank (2004) is expressed as

$$\frac{\partial \bar{x}}{\partial q_{in}} = \frac{1}{J} \sum_j^J \frac{p_{jn} \Delta t'_{ijn}}{\rho_{in}} \quad (2.7)$$

where $\bar{x}$ describes the time-averaged mass mixing ratio, q the source emission (in mass per volume per time), j the discretized arrival time of a back trajectory (j practically represents one back trajectory) at grid space i, J the total number of back trajectories, n the discretized backward time unit, p the transmission function determining the fraction of material transmitted along a trajectory (accounting for decay and deposition processes), ρ the density of the substance, and $\Delta t'_{ijn}$ the residence time of trajectory j in spatio-temporal grid cell (i, n). In simpler terms, emission sensitivity is the average residence time of back trajectories in a given intersected grid cell and therefore describes the potential of that grid cell to contribute to transport to a receptor area (Pisso et al., 2019; Seibert & Frank, 2004). In the context of this study, a higher (lower) emission sensitivity means a longer (shorter) trajectory residence time in a given intersected grid cell, allowing for increased (decreased) particle entrainment from that grid cell given a non-zero emission rate. Further details on the theoretical derivation of emission sensitivity are described in Seibert & Frank (2004). Computing emission sensitivity for each grid cell generates an emission sensitivity map, which is typically calculated for the bottom 100 m of the model output grid to determine sensitivity to surface emissions (e.g., McConnell et al., 2018; Eckhardt et al., 2017). While these maps are indicative of particle transport, they do not comprehensively characterise transport pathways (especially in the vertical dimension) as the emission sensitivity calculation only considers the residence time of a back trajectory and not its exact path. Hence, it is beneficial to discuss both emission sensitivity and plume trajectories to gain a comprehensive understanding of dust transport to the ISOL-ICE site. Importantly, emission sensitivity is not tantamount to the actual aerosol contribution from each source region since the released backward

particles are prescribed and not representative of actual source emissions. To compute the actual contribution, the emission rates from source areas must be known. This calculation requires further dust emission modeling that can be done in future work but is beyond the scope of this study.

3.2.3 Model configuration

Flexpart is used to identify key dust transport pathways to the ice core site in DML. The model set up is designed to simulate backward particle dispersion and transport forced by 6-hourly meteorological fields from European Centre for Medium-Range Weather Forecasts (ECMWF) Reanalysis Interim dataset (ERA-Interim, Dee et al., 2011). The ERA-Interim input data has a 0.75° x 0.75° horizontal grid resolution and 60 vertical model levels. While the current version of the Flexpart can also utilise data from the United States National Center of Environmental Prediction (NCEP) Global Forecast System (GFS), ERA-Interim is used because previous work has shown it to be the most reliable atmospheric reanalysis over the SH (Bracegirdle & Marshall, 2012). Additionally, ERA-Interim is used over the newer ECMWF Reanalysis version 5 (ERA5, Hersbach et al., 2020) since currently, ERA-Interim is the freely accessible dataset for use with Flexpart.

From the ISOL-ICE site (74°60′S, 0°6′E), the model is configured to release a puff of 20,000 particles every 3 hours from 15 January, 1979 to 31 December, 2016. Particles are then dispersed and transported backward in time for a duration of 14 days as this is the typical maximum lifetime of tropospheric particulate matter (Kok et al., 2012). This duration also allows for a range of transport times to be explored by

merely truncating the model output files to shorter transport durations. To determine the sensitivity of transport to transit time, 14, 10, and 5-day trajectories are investigated. Particles are released at 4 heights (100, 600, 1500, and 3000 meters above ground level; m.a.g.l.) to comprehensively characterise the arrival of dust particles at the ISOL-ICE site. Dust transport to the surface is represented by the 100 m.a.g.l. release height as this level generally demarcates the atmospheric surface layer at the Antarctic Plateau (Rodrigo & Anderson, 2013). The 600 and 1500 m.a.g.l. release heights represent transport within and above the climatological atmospheric boundary layer, respectively (Engeln & Teixeira, 2013). Lastly, 3000 m.a.g.l. captures upper troposphere dust transport, such as that associated with cyclonic activity (Li et al., 2010; Gassó et al. 2010).

A novel approach in this study is to run Flexpart simulations with varying mean particle sizes in order to investigate the relationship of particle size and dust transport using a range of sizes. The particle sizes in the model are constrained by particle size observations from the ISOL-ICE core (section 4.1.3) and Holocene dust size mode data from the EDML ice core (section 2.2.1; Wegner et al., 2015), which were also measured using LPD and parameterised using a lognormal curve therefore making the two datasets comparable. The Holocene size mode from the EDML ice core drilled at Kohnen Station is ~2.2 μm (Wegner et al., 2015), while selected examples of PSDs from the ISOL-ICE core show dust particle size modes between 3.5 and 3.8 μm (Table 4.1). In general, 10 μm approximates the dust particle size mode at several dust source regions around the world and therefore is used as the upper limit of particle size for the simulations (Fig. 2.2; Mahowald et al., 2014). Based on this information, simulations were run using particle sizes of 2, 3, 4, 5, 8, and 10 μm.

The comprehensive set of model configurations used in this study allows for numerous combinations of parameters to be used for analysis and plotting (i.e. 4 release heights, 3 trajectory durations, and 6 size modes). However, for brevity, only select combinations are presented in this thesis.

3.2.4 Trajectory clustering

Trajectory clustering using the Trajectory Statistics (TrajStat) software (Wang et al., 2009) is utilised to determine the dominant dust plume pathways to the ISOL-ICE site. TrajStat is a Geographic Information System (GIS) software that provides a variety of statistical tools for analysing trajectories in the atmosphere (Wang et al., 2009). It has been used in conjunction with HySPLIT in several studies (e.g., Cruz et al., 2019, Ma et al., 2019, He et al., 2016). A script was developed to convert Flexpart trajectory output to HySPLIT format. The clustering technique used in this study is based on the Euclidean distance:

$$d_n = \sqrt{\sum_{i=1}^{n}((x_1(i) - x_2(i))^2 + (y_1(i) - y_2(i))^2)} \quad (2.8)$$

where $x_1(y_1)$ and $x_2(y_2)$ denote longitudes and latitudes between two temporally corresponding trajectory end points, and n is the total number of points for each trajectory, in other words the temporal duration of each trajectory. The clustering algorithm iterates over multiple combinations of trajectories, and the optimal number of clusters is determined based on the “elbow method”, which identifies the number of clusters where a large increase in total spatial variance between clusters occurs

(Wang et al., 2009). A mean trajectory is then produced for each identified cluster. Percentages are attached to each mean trajectory denoting the fraction of total trajectories included in each cluster.

Apart from clustering all back trajectories from the ISOL-ICE site, the Quantum Geographic Information System (QGIS.org, 2021) is used to isolate trajectories that pass over the main sub-Antarctic landmasses – SSA, South Africa, Australia, and New Zealand. Since mineral dust is terrestrial in origin, back trajectories that solely pass over marine regions are not representative of long-range transported mineral dust. Subsequent clustering is done on the subset of trajectories passing over the mentioned sub-Antarctic land areas.

3.3 Dust-climate relationship

3.3.1 Correlations

Correlation analysis is employed to investigate spatial and temporal relationships between dust deposition at the ISOL-ICE site and large-scale atmospheric circulation. The linear Pearson product-moment correlation is utilised:

$$R = \frac{\sum_{i=1}^{n}(x_i - \underline{x})(y_i - \underline{y})}{\sqrt{\sum_{i=1}^{n}(x_i - \underline{x})^2}\sqrt{\sum_{i=1}^{n}(y_i - y)^2}} \quad (2.9)$$

where x_i and y_i denote two chosen variables. The equation calculates an R-value between 1 to -1, wherein a positive (negative) value indicates that the variables

synchronously change in the same (opposite) direction. The strength of the relationship is determined by the absolute value of R, where 1 indicates a perfect correspondence and 0 indicates no relationship. Correlation analysis is performed from 1979-2017 for both seasonal and annual averaged data to identify persistent linear relationships between two variables. All data are detrended over their respective temporal coverage prior to calculating the correlations to emphasise interannual co-variability between the two variables rather than spurious relationships arising from trends in the two variables.

Climate data for the correlation analysis are primarily taken or derived from the ERA-Interim reanalysis (Dee et al., 2011). While the newer ERA5 dataset has recently become available, ERA-Interim is chosen for consistency with the Flexpart modeling. As discussed in the previous section, the dataset has a horizontal grid resolution of 0.75° x 0.75° and features 60 vertical model layers. Monthly averages of daily mean data are used, and the temporal coverage of the reanalysis dataset goes back to 1979. The only climate variables that are not taken from ERA-interim are sea surface temperature (SST) and outgoing longwave radiation (OLR). The SST dataset is comprised of monthly data with a horizontal resolution of 2° × 2° from the NOAA Extended Reconstructed Sea Surface Temperature version 5 (ERSST V5, Huang et al., 2017). The OLR data is from the NOAA Interpolated OLR dataset, which has a 2.5° x 2.5° horizontal grid spacing and a monthly temporal resolution (Liebmann & Smith, 1996). Compared to ERA-Interim simulated SST and OLR, the ERSST V5 and the NOAA Interpolated OLR dataset are derived from direct measurements of SST and OLR, respectively, and are therefore more reliable estimates than those simulated by ERA-Interim.

Among the ice core dust parameters, annually averaged CPP is chosen as the dust variable for the correlation analysis. Unlike dust concentration and dust flux, CPP provides information regarding changes to dust PSD. As discussed in the introduction, the size of a particle determines its susceptibility to wind flow and removal processes. Therefore, CPP is likely more representative of climatic changes compared to dust concentration or flux, as exemplified by Koffman et al. (2014). Years with gaps in the CPP data are excluded in the correlation analysis.

Dust CPP is correlated with several atmospheric/climate parameters. As particle transport is most directly associated with winds and precipitation, dust CPP is correlated with ERA-Interim meridional and zonal winds, and total precipitation. Circulation patterns are investigated by correlating CPP with ERA-Interim geopotential height, which describes the height of a specific isobaric surface and is indicative of regions of low (cyclonic) and high (anticyclonic) pressure (circulation). Given the susceptibility of the study region to tropical teleconnections (e.g., Clem et al. 2020, Turner et al., 2016), CPP is also correlated with tropical OLR (a proxy for the presence and intensity of deep tropical convection), SST, and upper-tropospheric stream function derived from ERA-Interim to investigate tropically-forced circulation patterns. The OLR and SST are used as measures of ENSO activity (Wang et al., 2017). The stream function represents upper-tropospheric non-divergent flow and is useful for investigating spatial patterns of Rossby wave propagation from the tropics to the mid-high latitudes. The stream function is derived from the rotational (V_{rot}) and divergent (V_{div}) components of wind velocity (V) following Helmholtz's theorem:

$$V = V_{rot} + V_{div} \quad (2.10)$$

which is further broken down into:

$$V_{rot} = k \times \mathrm{div}(\Psi) \quad (2.11)$$

where k represents the curl/rotation coefficient and Ψ is the stream function. Lastly, correlations between CPP and several climate indices are calculated to investigate the possible role of large-scale climate modes in driving regional circulation patterns related to CPP variability at the ISOL-ICE site. The indices used in this study are listed in Table 3.3. Annual and seasonal averages are calculated for all years depending on the common temporal coverage between the ice core and atmospheric/climate parameters. For most variables, correlation analysis is done between 1979 and 2017 due to the poor skill of atmospheric reanalyses over the SH prior to the modern satellite era (Bromwich & Fogt, 2004). However, for large-scale climate patterns (i.e. SAM, ENSO, and PDO indices), the temporal coverage extends as far back as 1900.

Table 3.3 Large-scale climate patterns investigated in this study along with corresponding indices.

Climate pattern	Index	Temporal Coverage	Description
SAM	Observation-based index from Marshall (2003)	1957-present	Difference in standardised zonal mean sea level pressure anomalies between weather stations located ~40° and 65°S
ENSO	Southern Oscillation Index from the National Oceanic and Atmospheric Administration (NOAA) Climate Prediction Center	1951-present	Standardised sea level pressure difference between weather stations in Tahiti and Darwin, Australia
PDO	PDO index (Zhang et al., 1997)	1900-present	The leading principal component of North Pacific monthly sea surface temperature variability poleward of 20°N

Linear trends are computed using linear regression primarily for the purpose of detrending variables. A linear trend line is fitted on temporal data by minimising the sum of the distances between the trend line and the individual data points. Trend analysis is useful for determining the long-term change of a dataset. The derived linear relationship can then be used for potentially removing trends that result in spurious correlation coefficients towards higher values due to variables trending together. This detrending process results in a more accurate representation of interannual co-variability between two parameters and provides information regarding how trends are affecting the correlations.

For all analyses, the Student's *t*-test is utilised for statistical significance testing. The data are assumed to follow a normal distribution, meaning values tend to cluster

towards an average and symmetrically taper off towards the tails of the distributions, which is a good approximation for the climate variables used in this study. Additionally, averages from one year to another are assumed to be independent resulting in n-2 degrees of freedom for a two-tailed t test, where n is the sample size. The null hypothesis for the correlation and trend analyses is that the correlation coefficient and linear trend are zero. Conversely, the alternative hypothesis states that the same calculated values are non-zero. A two-tailed test is calculated for all analyses since there is uncertainty as to whether the alternative hypothesis results in a positive or negative value. The t-tests for the various statistical analysis are expressed as:

$$\text{Correlation: } t_{n-2} = \frac{r\sqrt{n-2}}{\sqrt{1-r^2}} \tag{2.12}$$

where r is the correlation coefficient and n is the sample size,

$$\text{Linear trend: } t_{n-2} \approx \frac{b}{s_b} \tag{2.13}$$

where b is regression coefficient (slope of the line) and s_b is the standard error of the slope. The t-values are then converted into probability values (*p*-value) using statistical tables, and probabilities less than 10 % are considered significant. This threshold is conventionally used as the maximum probability for significance testing and translates to a 90 % confidence level that the alternative hypothesis is true.

3.3.2 Seasonal grouping of dust data for correlations analysis

Seasonal analysis of the dust record is conducted by splitting the 1979-2017 ISOL-ICE data into annual winter-spring (JJASON) and summer-autumn (DJFMAM) mean values. This grouping scheme is used for the following reasons. Firstly, dating of the ice core is based on the seasonality of sodium concentrations, showing a minimum in summer (Weller & Wagenbach, 2007) and a maximum in winter/early spring (Weller & Wagenbach, 2007; Sommer et al., 2000, Göktas et al., 2002). Second, previous research has shown that peak Antarctic dust deposition at the EDML site occurs most frequently in winter (Wegner et al., 2015). Since Wegner et al. (2015) based their seasonal dust analysis on seasonal sodium maximum following Sommer et al. (2000) and Weller & Wagenbach (2007), it is possible that the winter dust maxima noted in Wegner et al. (2015) is also an early spring peak, and hence the winter-spring grouping. Lastly, climatological atmospheric circulation patterns across the SH middle and high latitudes display a similar spatial structure in the winter/spring and summer/autumn semesters (Ding et al., 2012).

4. RESULTS

This chapter is divided into 1) ISOL-ICE ice core dust record, 2) dust dispersion modelling, and 3) dust-climate relationships. Each section reports on the key observations for each figure. A synthesis and discussion of the results are given in the Discussion chapter.

4.1 ISOL-ICE ice core dust record

The ISOL-ICE dust record is presented in this section. While the main focus of this thesis is the last century, the dust record over the last millennia (entire temporal coverage of the core; 668-2017 CE) is shown to contextualise dust variability over the last century.

4.1.1 Validation of the age-model

As this thesis utilises a previously analysed and dated ice core dataset (Winton et al., 2019), a brief validation of the age-model is presented here to confirm the dating on sub-annual timescales. The ISOL-ICE age-depth model is illustrated in Fig. 4.1 and is compared to two other ice cores retrieved in DML for reference. The age-depth models of the ISOL-ICE and the EDML (75°00′S, 00°04′E, 2882 m.a.s.l.; Ruth et al., 2007) cores, located ~1 km apart, show excellent agreement. Additionally, the age-depth model of M1 ice core (75°00′S, 15°00′E, 3457 m.a.s.l.; Hofstede et al., 2004), drilled within 500 km of the ISOL-ICE core in a higher accumulation zone, shows a

largely similar age-depth relationship as the ISOL-ICE and EDML cores except with slightly flatter slope at deeper levels.

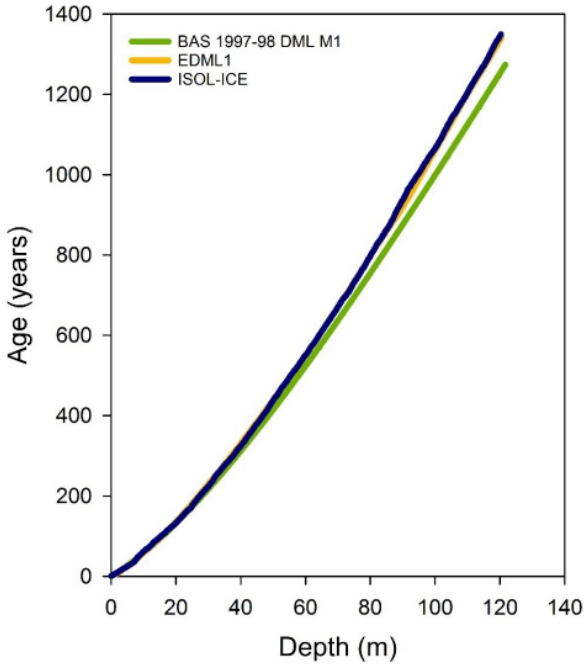

Figure 4.1 Age-depth model of the ISOL-ICE core and comparison to the EDML (EDML1 chronology; Ruth et al., 2007) and M1 ice core (Hofstede et al., 2004). From Winton et al. (2019).

The seasonal pattern of sodium concentrations in the ISOL-ICE core is investigated based on sodium minima in summer. To compare the seasonality of sodium concentrations in the dated ISOL-ICE ice core with monthly aerosol observations at the DML site, seasonal mean concentrations of sodium are computed for 12 equal intervals to represent 12 months between mid-summer annual markers (Fig. 4.2a) following Sommer et al. (2000) and Wegner et al. (2015). This method is adopted since the sub-annual dating of the core is based on linear interpolation between late winter/spring sodium minima assuming snowfall is constant throughout a year, but in reality, snow accumulation at the ISOL-ICE site is likely not evenly distributed throughout a year (e.g., Turner et al., 2019b). Hence, it is more appropriate to discuss seasonal patterns based on 12 intervals relative to the sodium minima

annual markers rather than specific calendar months. The numbers along the x-axis in Fig. 4.2a therefore indicate the intervals rather than specific calendar months.

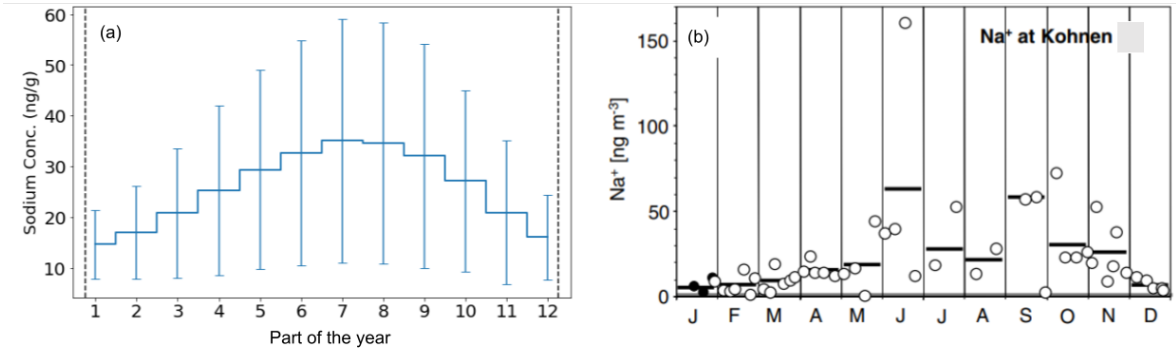

Figure 4.2 Seasonal sodium concentrations in the ISOL-ICE core and aerosols at the DML site. (a) ISOL-ICE ice core mean sodium concentration for the period 668-2017 CE. Data are divided linearly into 12 intervals between annual sodium minima in summer (vertical dashed line). Whiskers denote 1 standard deviation. (b) Observations of aerosol-based sodium concentrations at Kohnen Station from Weller & Wagenbach (2007). Open and filled circles denote measurements from the 2003-2005 and 2000-2002 field seasons, respectively. Black horizontal bars represent monthly means.

The seasonality of sodium in the ISOL-ICE core (Fig. 4.2a) shows a similar overall pattern to the observed seasonal aerosol sodium concentrations at Kohnen Station (Fig. 4.2b). The ISOL-ICE ice core seasonal sodium pattern displays a minimum in summer, while the highest concentrations are detected in months 7 and 8 indicating a peak in winter (Fig. 4.2a). Notably, the standard deviations are significantly larger in winter than in summer, indicating greater variability of sodium concentrations during this season. Comparatively, sodium concentrations measured on aerosol filter samples at Kohnen Station between 2000-2005 show a broad peak in winter-spring and a narrow trough in summer (Fig. 4.2b), consistent with and validating the age-depth model of the ISOL-ICE core on sub-annual timescales.

4.1.2 Dust mass concentration

The raw unsmoothed dust mass concentration from the ISOL-ICE core is presented in Fig. 4.3 highlighting the high sub-annual resolution of the record. From

668-1900 CE, total dust concentrations are relatively low with an annual average or "background" dust concentration of < 2.5 μg mL^{-1}. At ~1900 CE, there is an abrupt increase in the dust concentration with mean concentrations greater than 2.5 μg mL^{-1} and an average maximum concentration of ~12.5 μg mL^{-1} from the early-1900s onwards. To further explore the observed dust deposition, the next plots examine time slices of the smoothed record in more detail.

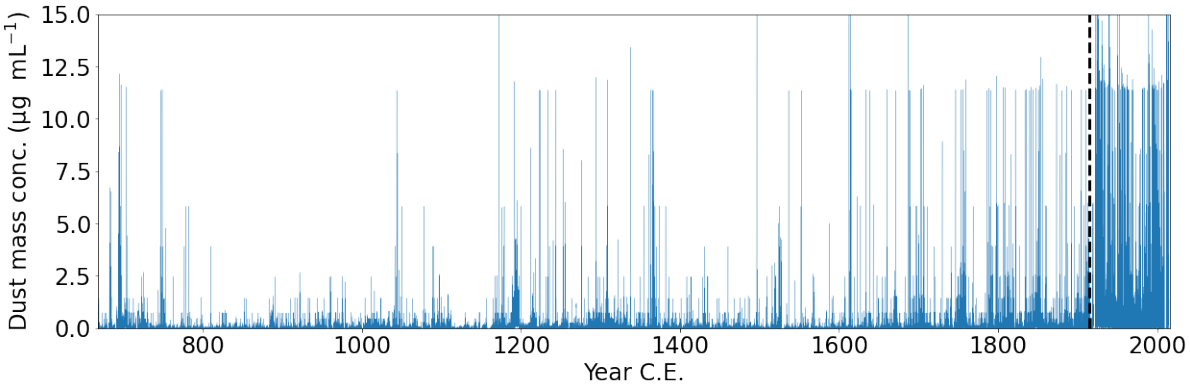

Figure 4.3 Dust mass concentration from the ISOL-ICE record. Data are presented as the high-resolution unsmoothed values. The vertical dashed line marks the abrupt increase in concentrations.

Trends over centennial timescales are investigated in the smoothed dust concentration record (Fig. 4.4). The focus is on centennial variability in order to contextualise dust trends over the past century. However, ten-year smoothed data are also shown to provide background variability. From about 700-800 CE, centennial mean concentrations decrease from ~0.09 to 0.02 μg mL^{-1}, marking a relative minimum at ~800 CE (Fig. 4.4a). This is followed by an upward trend between 800-1200 CE reaching peak dust mass concentrations of ~0.1 μg mL^{-1} at ~1200 CE. A second relative minimum occurs ~1450 CE wherein average dust concentrations dip to ~0.03 μg mL^{-1}. From 1450 onwards, concentrations follow a positive trend in which the most notable feature is an abrupt increase in concentrations in the early 1900s. This shift demarcates a relatively lower mean concentration from 668-1900 CE and a higher mean from the early-1900s onwards. Based on change-point analysis, dust

mass concentrations increase from a background mean of 0.04 µg mL^{-1} pre-1900 to 0.50 µg mL^{-1} from the early-1900s onwards, translating to a ~10x increase in dust deposition at the site. For the 10-year smoothed data, there appears to be regular cycles in dust deposition over this timescale, indicating variability over shorter timescales. Further analysis is required to quantify these periodicities and can be done in future work.

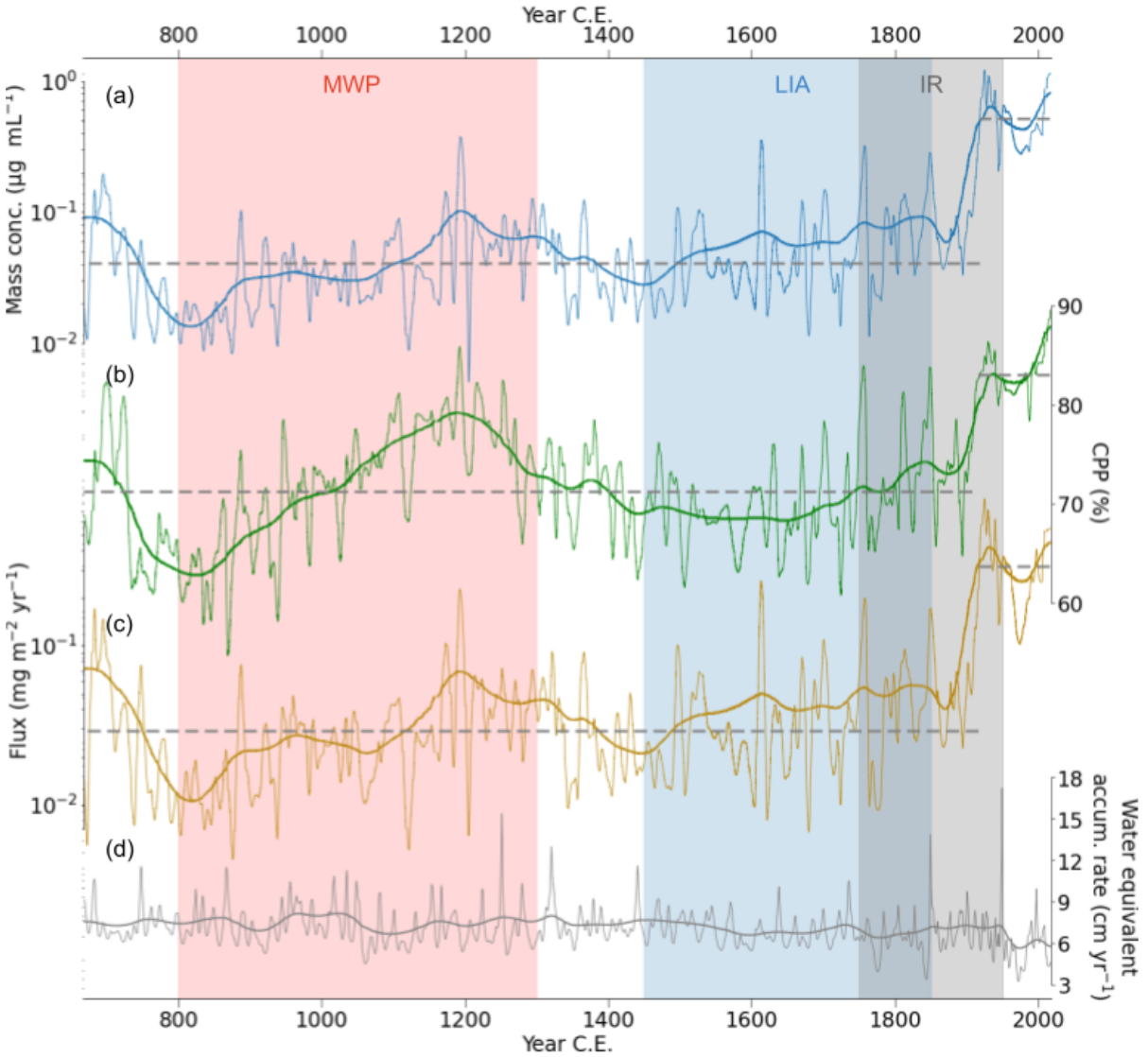

Figure 4.4 The ISOL-ICE dust record: (a) dust mass concentration, (b) coarse particle percentage (CPP), (c) dust flux, and (d) the snow accumulation rate at the ice core site. Data are low-pass filtered with a cutoff of 10 years (thin lines) and 100 years (thick lines). Dashed horizontal grey lines denote the means of distinct periods identified through change-point analysis, and the break signifies the change-point. Mass concentration and flux are plotted on a logarithmic scale to emphasise variability. Known historical climatic/anthropogenic periods are noted at the top of the plot: Medieval Warm Period (MWP), Little Ice Age (LIA), and the Industrial Revolution (IR).

From 1850-2017 CE, the multi-decadal trends in Fig.4.5a show that the increase in mass concentration starts ~1915 CE and peaks between 1925-1930 CE. Between 1850-1915 CE, mean concentrations are ~0.06 μg mL^{-1} then rises to a maximum of ~0.9 μg mL^{-1} between 1925-1930 CE. This is followed by a decrease in concentrations reaching a relative minimum of ~0.5 μg mL^{-1} around 1975. From ~1980s onwards, dust concentrations follow an upward trend.

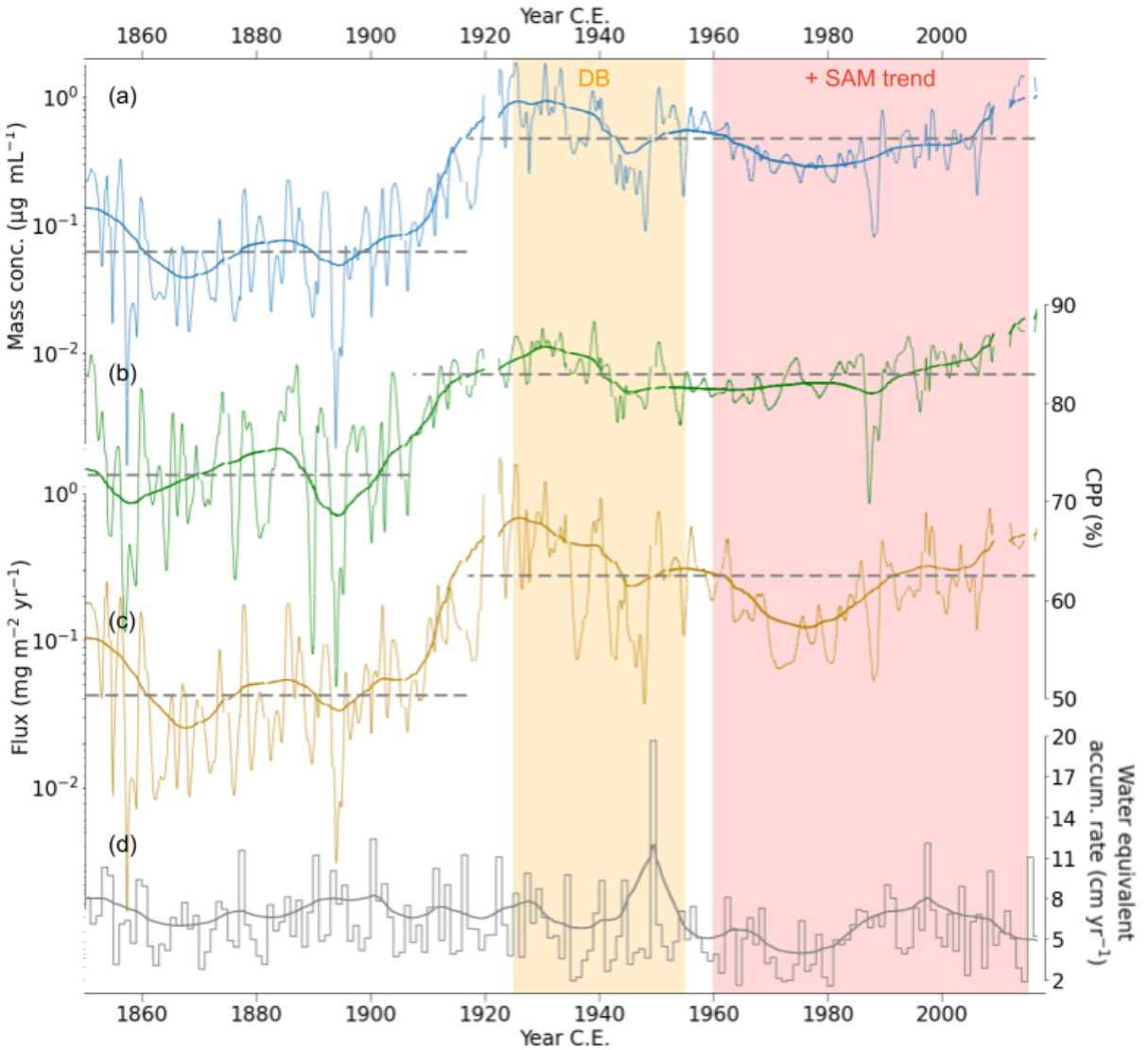

Figure 4.5 Same as Fig. 4.4 but for 1850-2017 CE. Data are low-pass filtered with a cutoff of 2 years (thin lines) and 21 years (thick lines) with the exception of the thin line for accumulation rate, which is presented as the unsmoothed annual average data. Known historical climatic/anthropogenic periods are noted at the top of the plot: Dust Bowls (DB) and the positive SAM trend.

The satellite era (1979-2017 CE) is characterised by an upward trend in mass concentrations (Fig. 4.6a). The trends are significant at $p < 0.01$ and are primarily comprised of relatively low concentrations (~0.1 μg mL^{-1}) in the late-1980s and high concentrations (~1 μg mL^{-1}) in the mid-2010s.

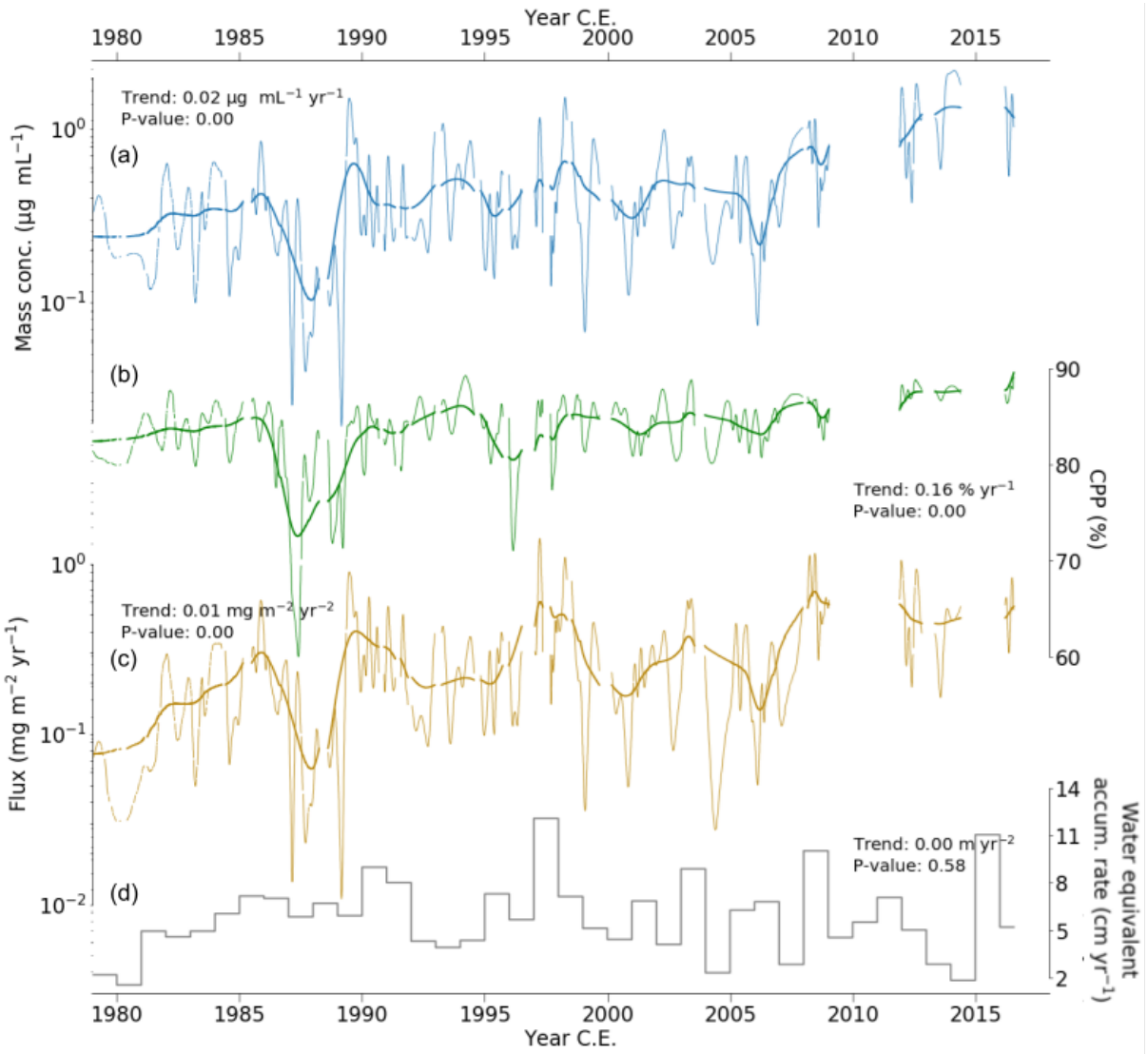

Figure 4.6 Same as Fig. 4.4 but for 1979-2017 CE. Data are low-pass filtered with a cutoff of 6 months (thin lines) and 3 years (thick lines) with the exception of accumulation rate, which is presented as the unsmoothed annual average data. Trends and associated statistical significance are noted for each time-series.

To determine whether the dust trends described above are similar across all particle sizes, dust mass concentrations are segregated into fine (0.9-5.0 μm), coarse (5-10 μm), large coarse particles (10-50 μm) following Laluraj et al. (2020). An overall

upward trend is observed for large coarse particles over the entire record (Fig. 4.7a). Additionally, the dominant size range changes at ~1200 CE. Fine particles dominate the mass concentrations between ~800-1150 CE, with concentrations of fine dust particles averaging ~0.01 μg mL^{-1}, while coarse and large coarse particles show mean concentrations of ~0.003 μg mL^{-1} at ~ 800 CE and ~0.008 μg mL^{-1} between 900-1150 CE. From 1200 CE onwards, large coarse particles generally dominate dust deposition at the ice core site. Thus, 1200 CE appears to mark a transition to larger particles dominating the dust mass concentration of dust deposited at the site. This predominance in mass concentrations is emphasised through to the early-1900s abrupt increase, wherein large coarse particles appear to define a new mean level in mass concentrations. In contrast, fine and coarse particles exhibit a similar sudden increase in concentrations in the early-1900s but drop to pre-1900 levels afterwards. Hence, the transition to a higher mean concentration level is less apparent for these smaller particle sizes. Notably, however, fine and coarse particles exhibit a secondary sharp increase in the 2000s.

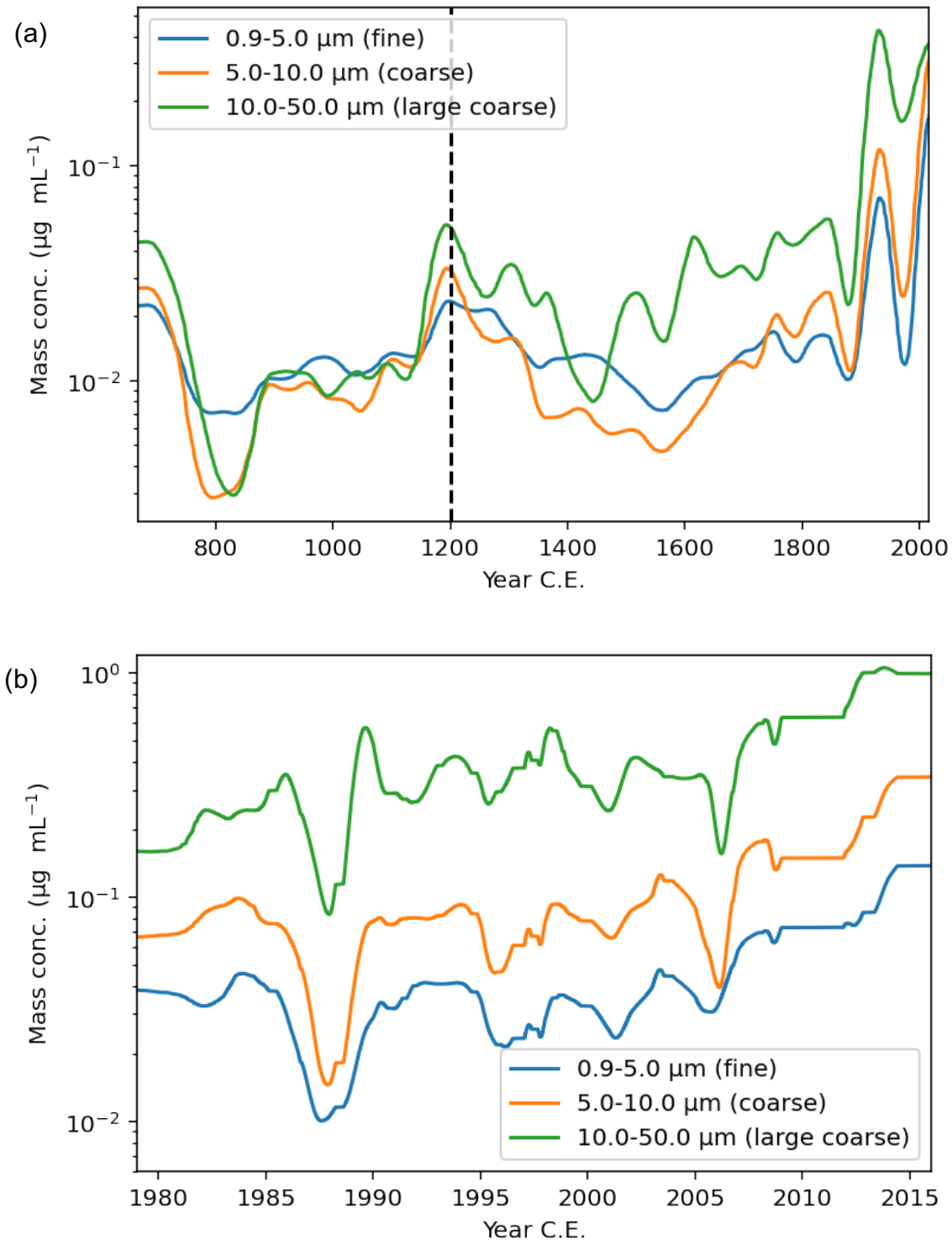

Figure 4.7 Size segregated mass concentrations for (a) 668-2017 CE and (b) 1979-2017. Data for (a) are low-pass filtered with a cutoff of 100 years. The dashed vertical line marks the 1200 CE transition. Data for (b) are low-pass filtered with a cutoff of 3 years.

Similar mass concentration trends are observed across particle sizes between 1979-2017 (Fig. 4.7b). Positive trends are seen in all size bins with relatively low

concentrations in the late-1980s and high concentrations in the 2010s. As with the 1850-2017 trends, large coarse particles dominate dust concentrations at the ice core site between 1979-2017.

Seasonal mean dust mass concentrations from 668-2017 CE exhibit a bi-modal distribution (Fig. 4.8a). As with sodium concentrations, seasonality is explored by dividing each year by 12 equidistant intervals between annual sodium minima during summer. Two peaks in dust mass concentrations are detected in months 3-4 or autumn and months 8-9 or winter/spring, with the latter having the highest dust concentrations. The lowest concentrations are observed during summer. This seasonal dust pattern is consistent with dust deposition at the site between ~2000 – 15,000 years BP (Wegner et al., 2015), where the EDML dust concentration maxima occurred most frequently in winter. The large standard deviations for the mean mass concentrations (mean: ~0.1 μg mL^{-1}, standard deviation: 0.5-1.2 μg mL^{-1}), highlight the episodic nature of dust deposition at the ISOL-ICE site throughout the year (Fig. 4.8b).

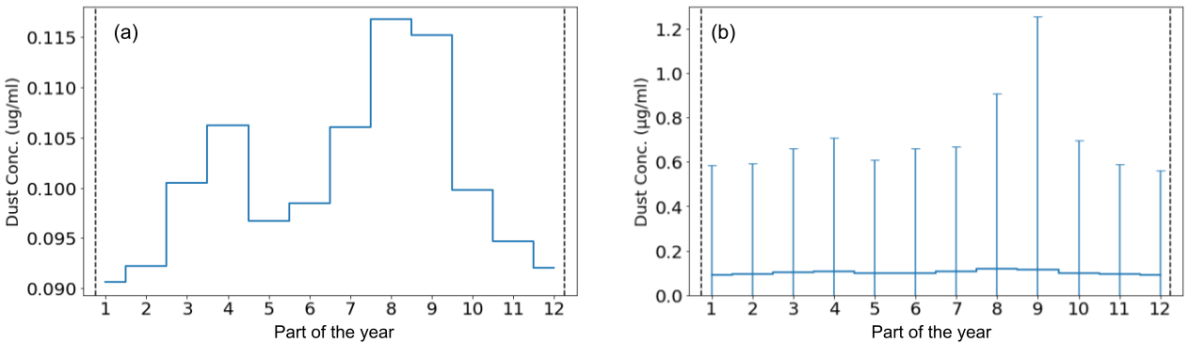

Figure 4.8 Mean seasonal variations in dust mass concentration for the period 668-2017 CE. Data for each year is divided into 12 equidistant intervals as labelled in the x-axis. (a) Mean concentrations for each interval across all years. (b) Mean concentrations including error bars denoting 1 standard deviation. The range of values for (b) are limited to > 0 since negative mass concentrations are unphysical. The vertical dashed lines denote the mid-summer sodium minima.

Based on the findings from this section, three points can be made. Firstly, change point analysis reveals that dust deposition over the 100 years is characterised

by the early-1900s abrupt increase in mass concentrations from a background mean of 0.04 μg mL^{-1} pre-1900 to 0.50 μg mL^{-1} from the early-1900s onwards. Second, a transition to large coarse particles dominating mass concentrations occurs from ~1200 CE onwards. Lastly, seasonal dust deposition shows a maximum in winter/spring and minimum in summer.

4.1.3 Particle Size Distribution

Selected examples of volume-size distributions fitted with a lognormal curve are shown in Fig. 4.9. The focus is on dust particles between 1 and 10 μm to reduce the influence of locally sourced dust on the PSD. The selected PSDs show a size mode between 3.5 and 3.8 μm. Comparatively, the mode of EDML ice core dust during the Holocene (~2000 – 12,000 years BP) ranged between 2-3 μm (Wegner et al., 2015). The mode increase is interesting and warrants further investigation in future work.

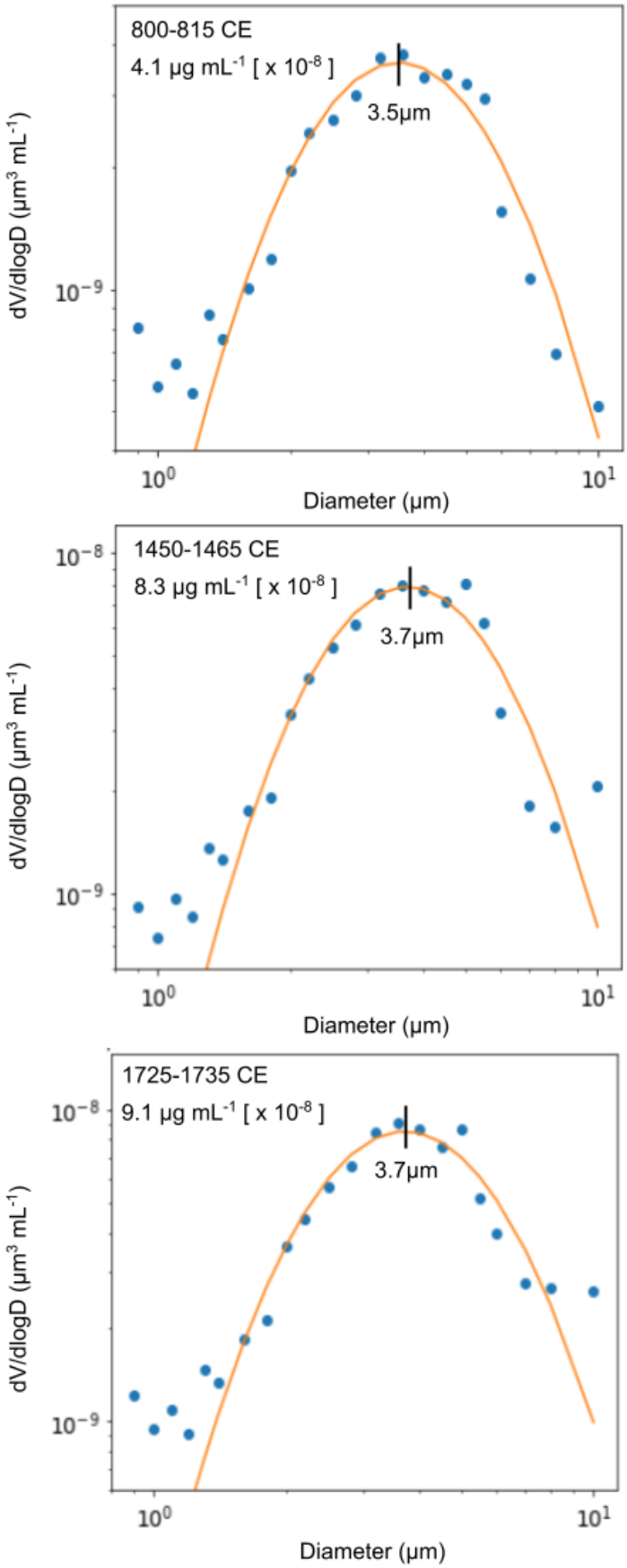

Figure 4.9 Examples of normalised volume size distribution of 1-10 µm particles in the ISOL-ICE ice core. The average dust mass concentrations are also noted in each plot.

To determine if there is a relationship between dust mass concentration and particle size mode over time, five selected examples of PSDs are listed in the Table 4.1. The mode ranges from 3.5 to 3.8 μm and appear to vary randomly with respect to mass concentrations. Hence, no clear relationship between mass concentration and the particle size mode can be determined from the limited number of samples. However, the mode increases from 3.5 to 3.8/3.7 μm after 1200 CE (Table 4.1) when the dust concentration record switches from a greater concentration of fine to large coarse particles (Fig. 4.7). While acknowledging the limitation of a small number of samples, the similarity of the mode in samples from 1200 onwards, and the lack of a relationship between dust concentration and mode, a mode of 3.5 μm is used to represent the period 668-1200 CE and 3.7 μm between 1200-2017 CE.

Table 4.1 Mode and mean dust concentration of particles between 1-10 μm of selected PSD examples.

Depth (m)	**Time period** (CE)	**Mean Concentration** (μg mL^{-1})	**Mode** (μm)
109.97-110.97	800-815	4.1 [x 10^{-8}]	3.5
69.70-70.70	1338-1351	4.8 [x 10^{-8}]	3.8
51.99-52.99	1545-1557	5.0 [x 10^{-8}]	3.8
60.29-61.29	1450-1465	8.3 [x 10^{-8}]	3.7
35.71-36.61	1725-1735	9.1 [x 10^{-8}]	3.7

In addition to volume-size distributions, the trends in dust CPP also show distinct patterns over the entire record similar to that of dust mass concentration. Over centennial timescales, dust CPP decreases from 77 to 63 % from 700-800 CE then rises to a relative maximum of 79 % at ~1200 CE (Fig. 4.4b). This peak in CPP at 1200

CE coincides with the transition from fine to large coarse particles dominating dust mass concentration (Fig. 4.7) and the increase in size mode from 3.5 to 3.7 μm after ~1200 CE. From 1200 CE onwards, CPP reaches a relative minimum of 67 % at ~1600 CE followed by positive trend and a sudden increase in the early-1900s (Fig. 4.4b). Dust CPP changes from a mean of 71 % before 1900s to 83 % after the abrupt shift, reflecting a 12 % increase in the proportion of 2-5 μm particles relative to 0.9-2 μm particles. The increase occurs between 1905-1930 reaching a maximum of ~87 % at ~1930 (Fig. 4.5b). From the early-1940s to ~1980, CPP remains constant at ~82 %. Over the satellite era, CPP exhibits a significant positive trend (Fig. 4.6b), again reflecting an increasing proportion of 2-5 μm particles being deposited at the ice core site. The trend over the satellite era is significant at $p < 0.01$ and is characterised by low CPP (< 80 %) in the late-1980s and a slight increase in the 2010s reaching a maximum of ~90 %. Additionally, dust CPP for most of the satellite era is approximately 80-90 %.

Based on the volume-size distributions and CPP, three main points can be made. Firstly, the proportion of larger particles being deposited at the ISOL-ICE site has been increasing over time. Second, the particle size mode is ~3.5-3.8 um, and there is a shift in the dominant size range at ~1200 CE. Third, the CPP follows similar centennial trends as the dust mass concentration.

4.1.4 Dust flux and accumulation rate

Dust flux trends throughout the record follow the CPP and dust mass concentrations trends. Over centennial timescales, dust flux exhibits a maximum of

0.08 mg m^{-2} yr^{-1} at ~1200 CE and minima of 0.01 and 0.03 mg m^{-2} yr^{-1} at ~800 and ~1450 CE, respectively (Fig. 4.4c). From 1450 CE onwards, dust flux increases with a sharp rise in the early-1900s, translating to a ~10x increase from a mean value of 0.03 mg m^{-2} yr^{-1} pre-1900 to 0.30 mg m^{-2} yr^{-1} after the abrupt shift. Given that dust flux is computed from dust mass concentration and accumulation rate, the abrupt increase in dust flux does not appear to be related to precipitation at the site as the snow accumulation rate does not show a similar sudden change in the early-1900s (Fig. 4.4d). Instead, from 668-2017 CE, the accumulation rate shows significant decadal variability between 3-18 cm yr^{-1} (water equivalent) with a mean of ~7 cm yr^{-1} over centennial timescales. In the last century, dust flux trends are marked by the abrupt increase in the early-1900s (Fig. 4.5c). The rapid increase starts ~1915 and peaks between 1925-1930 with a value of 0.7 mg m^{-2} yr^{-1}. Dust flux then decreases to a relative minimum of 0.1 mg m^{-2} yr^{-1} in the late-1970s. From 1979-2017, the dust flux follows a significant ($p < 0.01$) upward trend (Fig. 4.6c), with relatively low values in the late-1980s amounting to 0.07 mg m^{-2} yr^{-1} followed by a gradual increase through to the 2010s.

The multi-decadal (Fig. 4.5d) and interannual variability (Fig. 4.6d) of the accumulation rate has a more observable contribution to dust flux compared to over centennial timescales (Fig. 4.4d). For instance, the dust flux after 2010 decreases (Fig. 4.6c), whereas mass concentration continues to increase after 2010 (Fig. 4.6a). The difference in trends is likely due to low accumulation rates during the early-2010s (Fig. 4.6d). The observable effect of accumulation rate on the dust flux indicates that wet deposition has more influence on dust deposition at the ISOL-ICE site over multi-decadal and interannual timescales than over centennial timescales. In contrast, dry

deposition is likely more important for dust deposition over centennial timescales as inferred from the minimal contribution of accumulation rate to dust flux over these timescales (Fig. 4.4c & d). Additionally, there is no significant trend for accumulation rate from 1979-2017. Precipitation at the ice core site is therefore likely not a main driver of the upward trend in dust flux over this period but has an observable effect on interannual dust flux variability.

4.1.5 Linking centennial dust trends to historical climatic periods and anthropogenic events

On centennial time scales, the timing of certain peaks and troughs in the pre-1900 dust trends coincide with historical climate periods and anthropogenic events discussed in section 2.2.2. The upward trend in dust parameters (i.e. dust mass concentration, CPP, and flux) from 800-1200 CE and the peak at 1200 CE (Fig. 4.4) align with the MWP when temperatures were warmer than average over the past 2000 years. The minimum in dust parameters centred between 1450 and 1600 CE coincides with colder temperatures during the LIA, as most clearly observed in the dust CPP trends. From ~1600 CE onwards, the common upward trend in dust parameters preludes the start of the industrial era (~1750 CE) when anthropogenic global warming is thought to have begun. On glacial-interglacial timescales, warmer (colder) periods coincide with decreased (increased) dust deposition over Antarctica (e.g., Wegner et al., 2015; Shaffer & Lambert, 2018). However, the temperature-dust relationship over the past millennium inferred from ISOL-ICE core is contrary to how dust is known to vary during glacial-interglacial cycles and could be indicating a different combination of PSAs and/or different dynamics governing dust transport and deposition during

warm interglacial periods. Furthermore, the described potential relationship is not always consistent as exemplified by the increasing dust mass concentration and flux over the LIA. Other factors may be influencing dust deposition at the ice core site and further work looking at other climate proxies is needed to determine the veracity of this potential relationship.

Over the last century, the early-1900s abrupt increase in dust deposition occurs ~15 years before the dust bowls over SSA but peaks during the dust bowl era. While the main dust bowl period is between 1930s to the 1950s, declining crop cultivation and precipitation have been recorded since the 1910s (Viglizzo & Frank, 2006), thereby coinciding with the abrupt increase and suggesting a source-related mechanism behind the sudden shift.

In addition, the upward trend in dust parameters from the ~1980s onwards occurs during the period of the positive SAM trend as discussed in section 2.4. Given the hemispheric-scale influence of SAM, it is possible that the poleward contraction of the circumpolar winds during summer provides more favourable climatic conditions for long-range transport of dust from SSA to the the ISOL-ICE site. Later sections will investigate dust relationships with atmospheric circulation in more detail.

To determine the possible drivers of the dust deposition variability observed in the ISOL-ICE core, the next sections focus on investigating dust transport and relationships with atmospheric circulation over the satellite era (1979-2017). This time period is chosen due to the availability of reliable atmospheric reanalysis data (Bromwich & Fogt, 2004).

4.2 Dispersion Modelling

To gain a better understanding of the regional atmospheric drivers of dust variability at the ice core site, it is crucial to first characterise the dust transport pathways to the site. This section discusses the results of dust transport modelling using Flexpart (Pisso et al., 2019), with one of the key objectives of investigating the sensitivity of dust transport to various parameters such as particle size and seasonality. Findings from this section will give an overview of key dust transport pathways to the ice core site and help determine dominant dust source regions over the overlapping period of the ice core data and satellite era (1979-2017). This information will be used to interpret the observed ice core dust variability presented in the previous section 4.1 and the dust-climate relationships in section 4.3. For the dispersion modelling, both dust trajectories and emission sensitivities are investigated as these simulated variables provide complementary information regarding dust transport and PSA. While mineral dust is terrestrial in origin, emission sensitivities over marine regions are also shown in order to show the overall spatial pattern of emission sensitivity in the study region.

4.2.1 Dust back trajectories

The dust plume trajectories presented here comprise the following:

1) Trajectory clusters (instead of individual trajectories) to highlight spatial variability of the dominant transport pathways

2) Ten day back trajectory clusters (for most figures) since this duration approximates the upper limit of the transit time of dust particles transported from SSA to East Antarctica (Gassó et al., 2010; Li et al., 2010)

3) Dust particle sizes of 2, 5, and 10 μm to capture the full range of simulated particle sizes observed in Antarctic ice core long-range transported dust

Clustering of all back trajectories from 1979-2017 show various potential dust transport pathways to the ice core site (Fig. 4.10). The most dominant clusters follow a large-scale westerly flow and approach the ice core site from the west or the northeast. These transport pathways comprise ~60 % of all back trajectories initiated from the ISOL-ICE site. Approximately 9-20 % of trajectories arrive from the east or southeast following the local polar easterly flow. The smallest number of trajectories, containing ~3-8 %, follow a cross-continental flow originating from the Ross Sea region of Antarctica. In general, trajectory cluster pathways are similar across particle sizes and release heights, with the exception of 10 μm particle trajectories showing longer mean trajectories compared to the 2 and 5 μm particle trajectories. This difference can be explained by a higher transport altitude simulated for 10 μm particles due to the strong influence of gravitational settling that translates to an upward vector backward in time. The backward trajectories suggest that distally-sourced 10 μm particles generally have to be transported at high altitudes in the atmosphere in order to arrive at the ice core site, and higher transport altitudes are associated with stronger wind speed leading to longer trajectories. Coarse 10 μm particles are therefore less likely to be transported to the ice core site compared to finer 2 and 5 μm particles as the strong influence of gravitational settling hinders sufficient uplift of large surface-emitted

particles required for transport at high altitude (Pye, 1987). Aside from longer trajectories for 10 µm particles, no other systematic difference can be observed across particle sizes and release heights. Interestingly, none of the clusters pass over or close to sub-Antarctic (north of 60°S) landmasses, and based on trajectory counts, trajectories originating from sub-Antarctic landmasses represent less than 20 % of all simulated trajectories. This finding suggests that most trajectories arriving at the ISOL-ICE site do not originate from sub-Antarctic land areas and that long-range dust transport from sub-Antarctic regions occurs infrequently. However, sub-Antarctic land areas are noted to be PSAs of dust deposited in Antarctica (e.g., Delmonte et al., 2019, Laluraj et al., 2020, Gassó et al., 2010), and therefore, only trajectories passing over sub-Antarctic continents are investigated in more detail to identify dust transport from these key sub-Antarctic PSA regions.

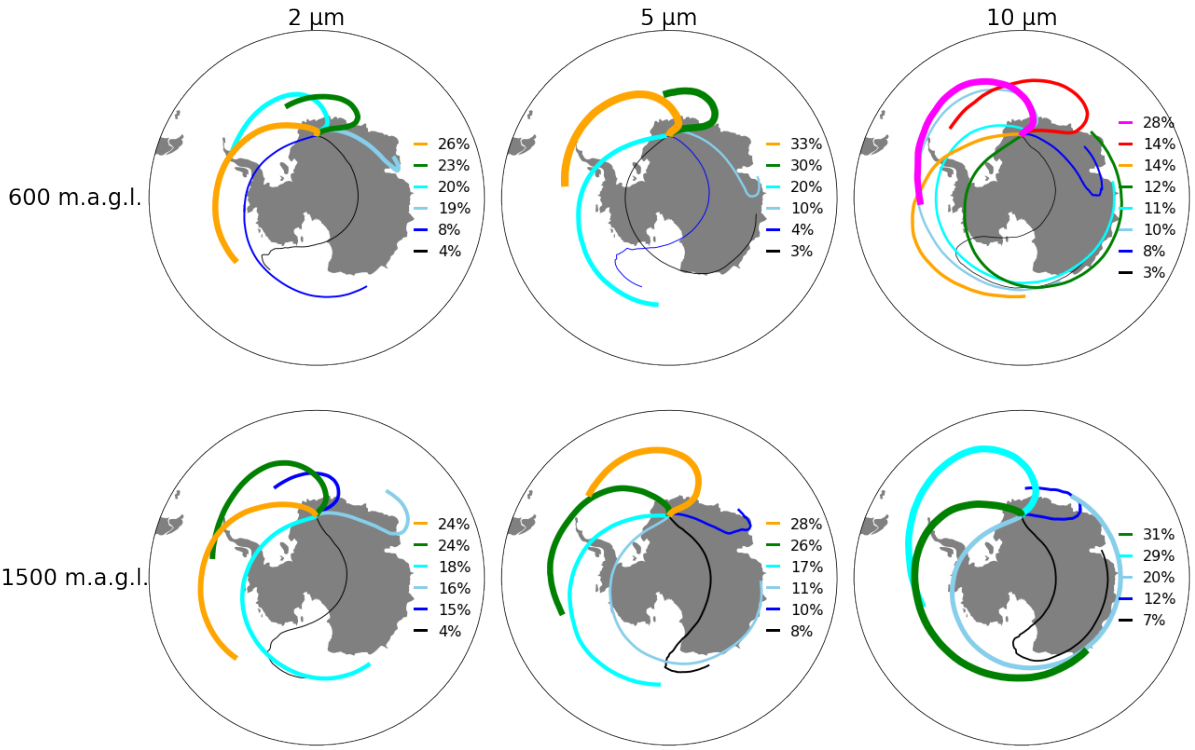

Figure 4.10 10-day back trajectory clustering across particle size (columns) and release heights (row) in meters above ground level. Line widths are proportional to the fraction of trajectories included in a respective cluster. Specific percentages of total trajectories included in each cluster are labelled on the right.

Mean transport paths for trajectories passing over sub-Antarctic landmasses predominantly intersect SSA and then follow a cyclonic/clockwise flow over the South Atlantic directed toward the ISOL-ICE site (Fig. 4.11). Across all particle sizes and release heights, at least 98 % of these trajectories pass over SSA, supporting SSA as a PSA for long-range transported dust to the ISOL-ICE site over the satellite period. The mean trajectory paths converge over SSA, particularly south of 45°S, and then diverge in the south Atlantic. This suggests that while transport pathways all pass over the same location in SSA, the exact path over the Southern Ocean is more variable. Some trajectory clusters show a more direct route from SSA to the ISOL-ICE site, while others travel further east from SSA before veering southward and then following the polar easterly flow to the ISOL-ICE site. With the exception of longer trajectories for 10 µm particles, no other systematic differences in transport pathways can be identified relative to particle size and release height (Fig. 4.11).

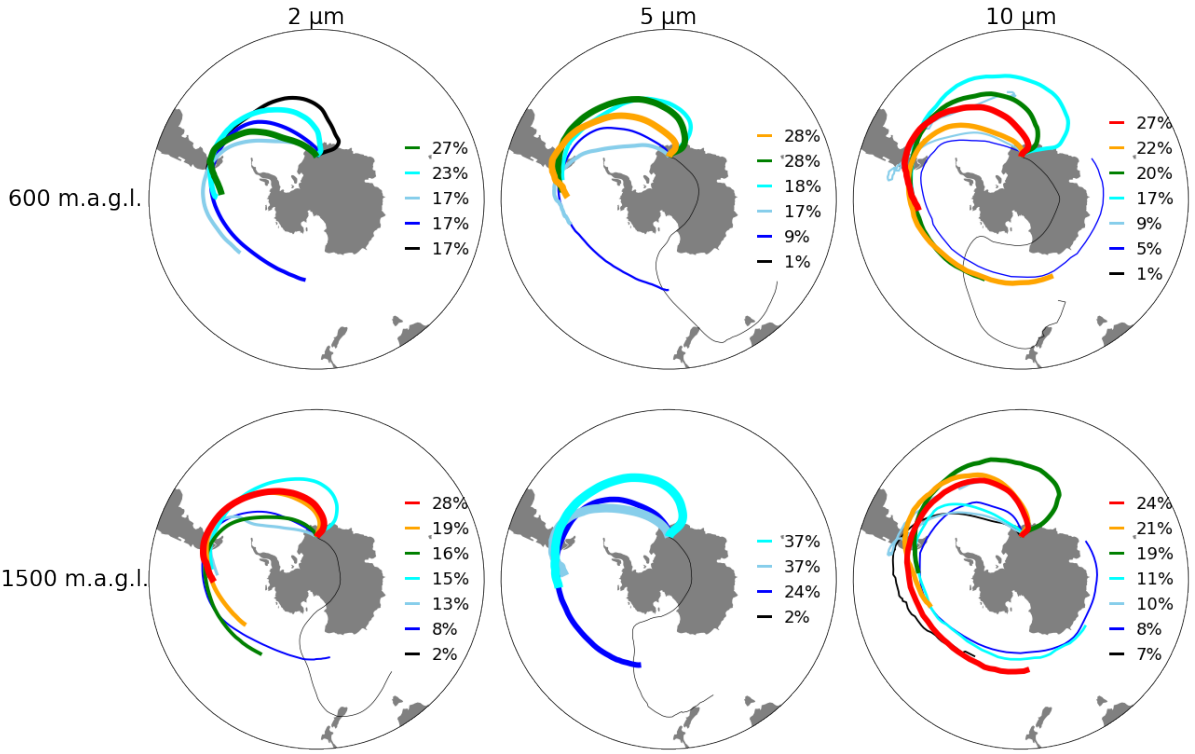

Figure 4.11 Same as Fig. 4.10 but for trajectories passing over sub-Antarctic landmasses.

A very small fraction (< 2 %) of trajectories passing over sub-Antarctic landmasses are part of a cluster originating from New Zealand (Fig. 4.11). The cluster is not consistently identified across all combinations of particle sizes and release heights and does not display a systematic pattern relative to these two factors. Nonetheless, identification of this pathway as a distinct cluster supports findings from recent modelling and Antarctic ice core research that New Zealand is a potential source of long-range transported dust particles for Antarctic regions as far as the Antarctic Peninsula (McConnell et al., 2021) and DML (Neff & Bertler, 2015). However, it has been shown through geochemical fingerprinting that New Zealand is not a major dust source for East Antarctica during the last glacial period (Koffman et al., 2021).

Compared to 10-day trajectories, 5-day trajectory clusters show no pathways originating from New Zealand and follow a more direct route from SSA to the ice core site (Fig. 4.12). The lack of clusters originating from New Zealand suggests that it takes more than 5 days for New Zealand sourced particles to reach the ice core site. Significantly fewer clusters are also identified for 5-day trajectories compared to 10-day trajectories meaning there is less variety in transport pathways and trajectories generally follow the same dominant pathway from SSA to the ice core site for 5-day transit times. Furthermore, the presence of 5-day trajectory clusters originating from SSA indicates that transit time from SSA to the ISOL-ICE site can vary between 5-10 days (and possibly longer or shorter), consistent with Gassó et al. (2010) and Li et al. (2010). Similar to 10-day trajectories, 5-day transport pathways do not exhibit any observable changes in relation to particle size and release height.

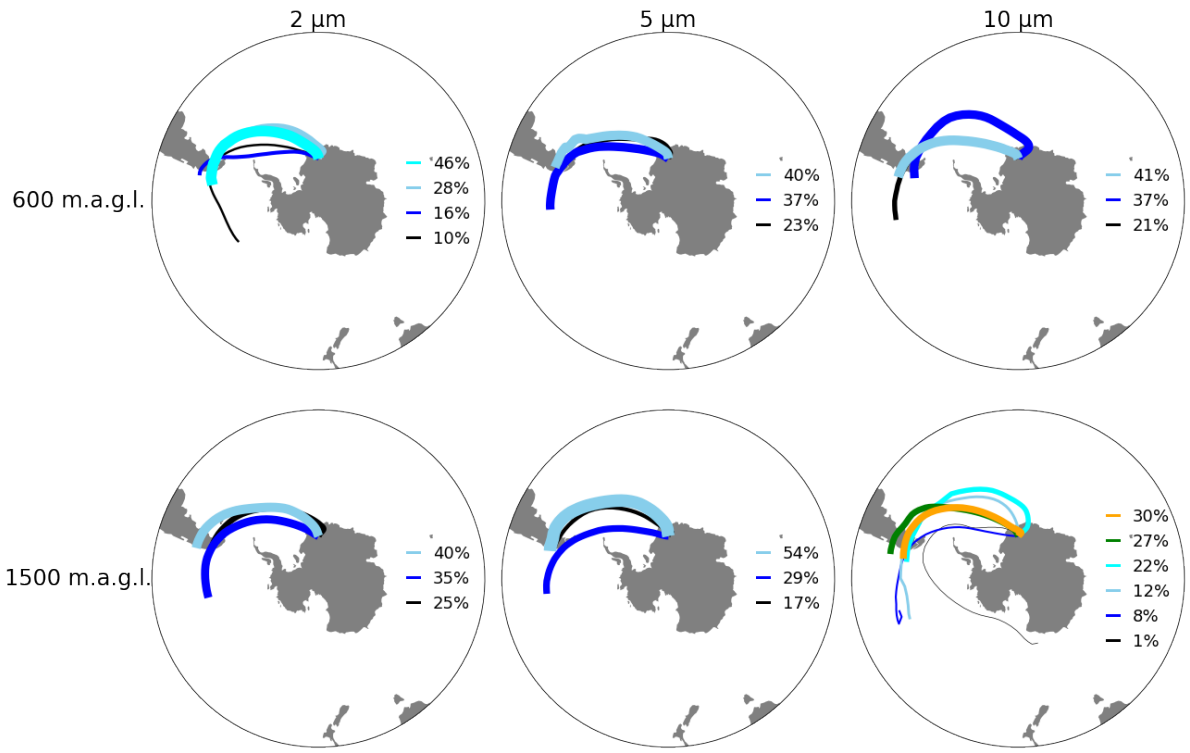

Figure 4.12 Same as Fig. 4.11 but for 5-day trajectories.

Average trajectory heights show an increasing altitude profile with distance from SSA to the ISOL-ICE site (Fig. 4.13). Fig. 4.13 shows trajectories from the 600 m.a.g.l. release height simulation which are similar to the 1500 m.a.g.l. release height (not shown). In general, the northernmost extent of trajectories has the lowest altitudes, while trajectories closest to Antarctica have the highest altitudes. The steepest increase in altitude is observed between ~60-75°S across the strong topographic relief along the Antarctic coast. This pattern is consistent with Neff & Bertler (2015), wherein simulated air parcel trajectories originating from SSA increase in altitude as parcels travel closer to Antarctica. While downward entrainment of particles is expected over the continent due to katabatic winds pronounced during winter (Broeke & Leipzig, 2003b; Laluraj et al., 2014), this is not evident in the 2 and 5 µm particle simulations; the average trajectory heights do not show any downward trend from the Southern Ocean to the ISOL-ICE site based on the plots measured in meters above sea level in

Fig. 4.13. However, downward transport near the ISOL-ICE site is simulated for 10 µm particles, with mean trajectory heights of 5500-6000 m.a.s.l. just off the coast of the ISOL-ICE site and 3000-4000 m.a.s.l. heights at the ISOL-ICE site. Based on the plots using meters above ground level, it can also be observed that trajectories are largely not terrain-following; trajectories just off the coast of the ISOL-ICE site are already at a high altitude even before reaching the continent. Therefore, while orographic lifting may contribute to the upward transport of particles near the ISOL-ICE site, other mechanisms, such as cyclonic activity, have already likely uplifted particles to a certain altitude before reaching the continent.

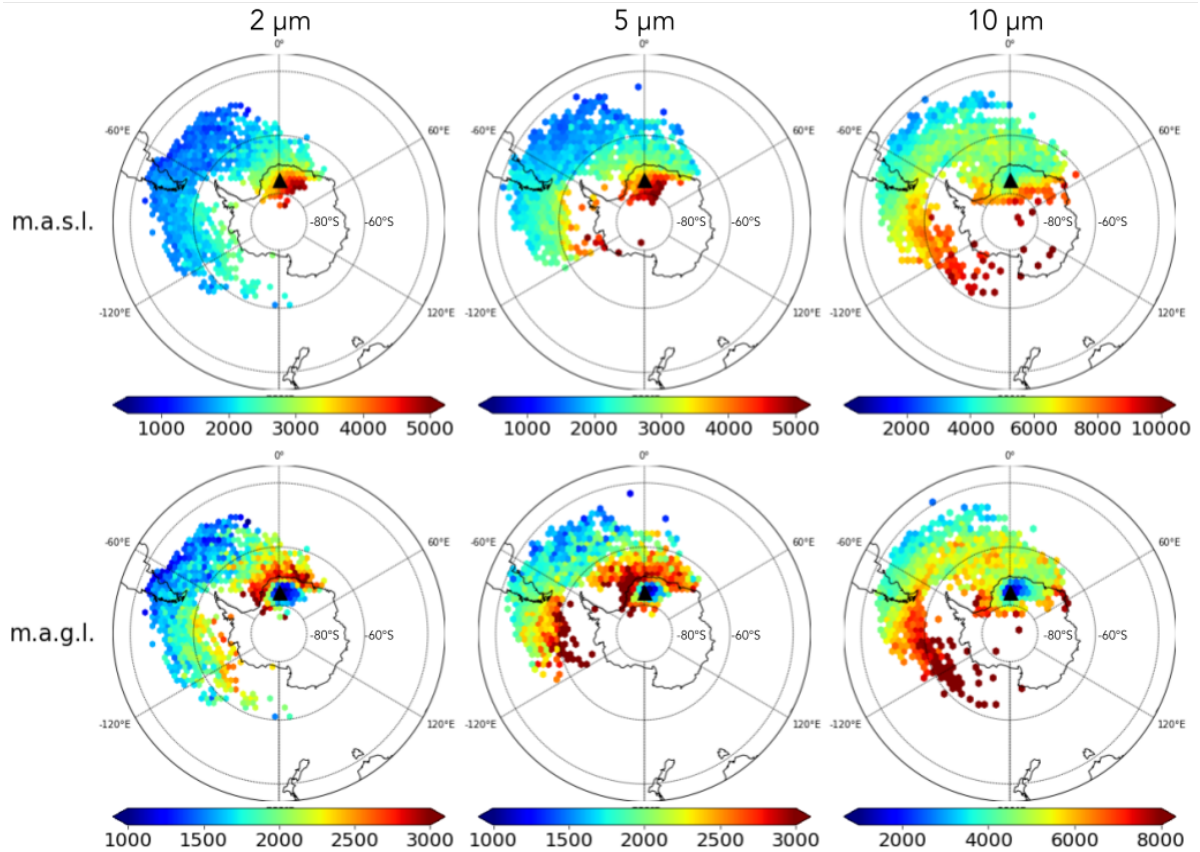

Figure 4.13 Average back trajectory height across particle size (columns) in meters above sea level and meters above ground level (rows) for the period 1979-2017. Trajectories are from the 600 meters above ground level release height simulation. The black triangle shows the location of the ISOL-ICE site. Note the different colour bar scales in the plots.

Mean trajectory heights vary depending on simulated particle size (Fig. 4.13). On average, trajectories are located ~1500, 2300, and 5000 m.a.s.l. over SSA for 2, 5, and 10 μm, respectively. Trajectories of finer particles are generally transported closer to the surface compared to coarser particles. This pattern can be explained by the fact that coarser particles have to be transported higher in the atmosphere because of the stronger influence of gravitational settling. Notably, the altitude difference between particle sizes is non-linear because Stokes law for gravitational settling is dependent on the particle size squared. The average trajectory heights over SSA also suggest that 2, 5, 10 μm particles from this source region need to be emitted and uplifted to ~1500, 2300, and 5000 m.a.s.l., respectively, in order to reach the ISOL-ICE site at 600 m.a.g.l. Hence, upward transport is required over SSA after emission or in downwind regions for particles to undergo long-range transport towards the ISOL-ICE site. The high altitude requirement for 10 μm particles makes it less likely for SSA particles of this size to be transported to the ISOL-ICE site compared to 2 and 5 μm particles, which have much lower altitude requirements (< 2300 m.a.s.l.).

The number of trajectories passing over sub-Antarctic landmasses show specific patterns relative to particle size, trajectory duration, and release height (Fig. 4.14). The specific relationships are discussed next.

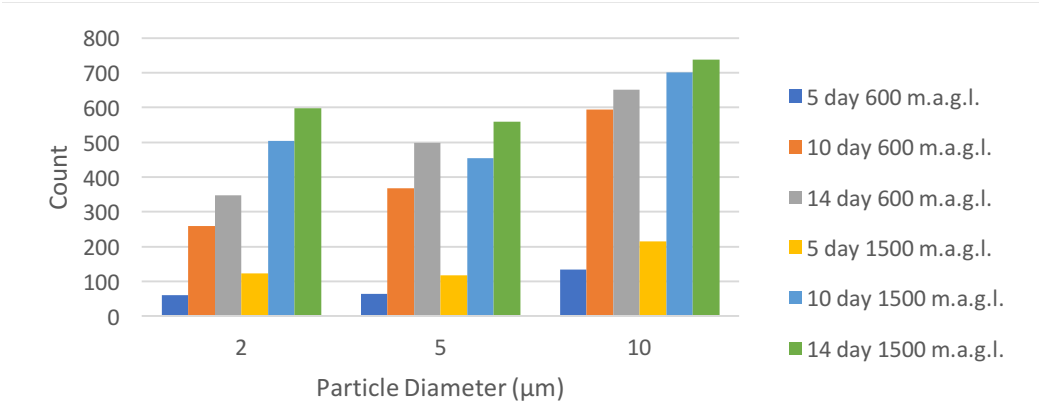

Figure 4.14 Variations in trajectory counts relative to particle size, trajectory duration, and release height for trajectories passing over sub-Antarctic landmasses.

In terms of particle size, a higher number of trajectories passing over sub-Antarctic landmasses contain coarser particles (Fig. 4.14). This relationship can be explained by the higher transport altitude required for larger particles to undergo long-range transport; higher-altitude transport generally follows longer trajectory paths as most clearly seen in the 10 µm particles in Fig. 4.11, and longer trajectory paths are more likely to pass over sub-Antarctic landmasses. However, back trajectories intersect sub-Antarctic land areas at different altitudes depending on particle size as shown in Fig. 4.13. Therefore, higher trajectory counts for coarser particles do not necessarily signify stronger transport of surface-emitted coarse dust particles. Higher trajectory counts merely suggest that transport pathways of coarser particles pass over sub-Antarctic landmasses more frequently than that of finer particles. Considering the high-altitude transport required of large particles, there is increased potential for long-range transport of coarser particles with higher dust uplift over source regions.

Trajectories with longer transport times show higher trajectory numbers reaching sub-Antarctic landmasses (Fig. 4.14). In particular, 5, 10, and 14-day trajectory counts range from ~60-220, 260-700, 350-740, respectively. This pattern is

expected as longer trajectory durations generally mean longer trajectory paths and hence higher likelihood of passing over sub-Antarctic land areas. Interestingly, 10 and 14 days show similar numbers of trajectories, while a larger difference is noted between 5 and 10 days. This difference suggests that dust transport from sub-Antarctic landmasses more often takes ~10-14 days rather than 5 days. Moreover, the small difference in trajectory counts between 10 and 14-day trajectories also suggest that ~10 days is the typical sufficient amount of time to obtain the most frequent transport of particles to the ISOL-ICE site from sub-Antarctic land areas. This transit time is consistent with findings from Gassó et al., (2010) and Li et al. (2010) indicating that transport to East Antarctica typically takes a maximum of 10 days.

Looking at particle release heights, the 1500 m.a.g.l. height shows higher trajectory counts than the 600 m.a.g.l. height (Fig. 4.14). This finding is consistent with previous explanations since long-range transported dust particles arriving at the ISOL-ICE site at higher altitudes would have also likely originated from higher initial altitudes. Higher altitude transport translates to longer simulated trajectories through stronger upper-tropospheric winds.

4.2.2 Emission Sensitivity

Across all the investigated particle sizes (2, 3, 4, 5, 8, 10 μm), the ISOL-ICE site is most sensitive to potential dust emissions from the East Antarctic Plateau and parts of coastal DML (Fig. 4.15). Compared to lower elevation West Antarctica or the Southern Ocean, dust particles originating from the East Antarctic Plateau are already at greater than 2 km elevation and only need not be transported less than 1 km

upwards to reach the ISOL-ICE site. While the emission sensitivity values are highest over the East Antarctic Plateau, this region is primarily ice covered, and hence there are less dust sources from this area compared to sub-Antarctic continents. However, local contribution from exposed rock surfaces near the ice core site, such as the mountain ranges near coastal DML, cannot be excluded, though the dust emissions from these landforms are difficult to quantify (Delmonte et al., 2019; Laluraj et al., 2009).

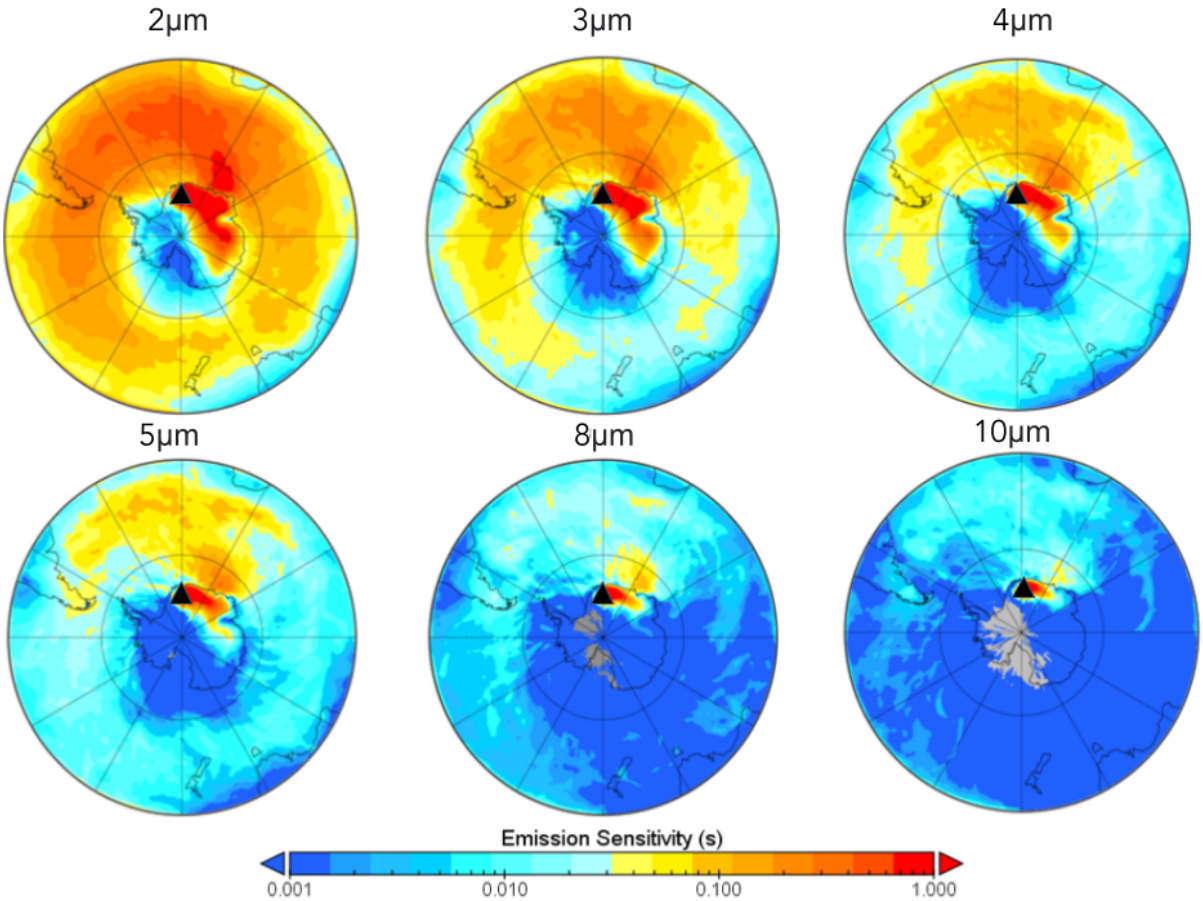

Figure 4.15 Average sensitivity of the ISOL-ICE site to surface emissions for the period 1979-2017. The location of the ISOL-ICE site is denoted by the black triangle. Units for emission sensitivity are in seconds, describing the residence time of back trajectories at each grid square.

In contrast to East Antarctica, West Antarctica hosts the lowest emission sensitivity values in the entire study region (Fig. 4.15). The low emission sensitivity is likely due to the amount of uplift required to transport particles high up onto the plateau

with respect to the dominant downward-flowing katabatic winds associated with the polar easterlies. These two factors (elevation and prevailing wind flow) are not conducive for dust transport from West Antarctica to the ISOL-ICE site. Local dust particles from West Antarctica generally have to circumnavigate the continent counterclockwise to reach the ISOL-ICE site given the prevailing easterly flow. Furthermore, the strong katabatic flows and stable boundary layer, especially near the plateau, impedes upward transport onto the plateau. Significant upward momentum from turbulence or convection would be required for particles to be entrained to higher altitudes. Antarctica generally experiences weak turbulent vertical mixing in the atmosphere (due to low insolation and strong temperature inversions) as exemplified by its relatively shallow atmospheric boundary (mixed) layer compared to lower latitudes (Engeln & Teixeira, 2013). Additionally, convective processes associated with cyclones mostly influence Antarctic coastal margins (e.g., Reijmer & Oerlemans, 2002), leaving the inland regions with minimal mechanisms to vertically transport dust. Among the regions in West Antarctica, the Ross Ice Shelf region emerges as the area with the lowest emission sensitivity as most clearly seen with 2 μm particles (Fig. 4.15). Apart from its low elevation (approximately sea level), this region is located on the opposite side of the continent to the ISOL-ICE site. Dust particles coming from the Ross Ice Shelf would have to undergo significant upward transport and travel ~ 3000 km to the opposite side of the continent to reach the ISOL-ICE site.

Interestingly, West Antarctica shows similar or less emission sensitivity compared to sub-Antarctic landmasses despite its closer proximity to the ISOL-ICE site (Fig. 4.15). These modelling results suggest that given the same emission strength and availability of dust particles across all PSA, the ISOL-ICE site would receive

similar or lower amounts of dust from West Antarctica compared to SSA, New Zealand, southern Australia, and South Africa. While these results seem counterintuitive given the closer proximity of West Antarctica to the ISOL-ICE site compared to sub-Antarctic landmasses, this finding makes physical sense because of more abundant mechanisms for dust uplift over the Southern Ocean and sub-Antarctic landmasses. For instance, sub-Antarctic landmasses likely experience stronger localised convective activity and turbulent mixing (and a deeper mixed boundary layer) owing to stronger insolation. Other possible mechanisms include cyclonic activity across the middle latitudes and associated frontal systems passing through dust source regions. The importance of higher/similar emission sensitivity in sub-Antarctic landmasses relative to West Antarctica is underscored by the fact that most of Antarctica is ice-covered, and wider areas of available dust sources are located in sub-Antarctic landmasses.

Among the sub-Antarctic landmasses, the highest emission sensitivity is simulated over SSA (Fig. 4.15). This high sensitivity over SSA is consistent with the predominant westerly flow transporting dust to the ice core site and with SSA being the dominant origin of long-range transported dust deposited at the ice core site (Fig. 4.11) and across East Antarctica as noted by previous studies (Wegner et al., 2012; Delmonte et al., 2019, 2017; Gili et al., 2017; Bory et al., 2010).

A similar spatial pattern of emission sensitivity is observed across different particle sizes but with decreasing magnitude with increasing particle size (Fig. 4.15). Emission sensitivity is greatest for the smallest particles (i.e. 2 μm particles) and progressively decrease for coarser particles, with 10 μm exhibiting the lowest

sensitivity. The ISOL-ICE site is 100 times more sensitive to emitted 2 μm particles compared to 10 μm particles. As discussed in section 2.1.3, coarser particles are more indicative of proximal transport as these particles typically settle back down to the surface near the source area. In contrast, finer particles are more susceptible to wind flow and are therefore more likely to undergo long-range transport. Interestingly, West Antarctica contains zero emission sensitivities (denoted by grey shading) in the 8 and 10 μm particle sizes. For 8 μm particles, the Filchner-Ronne Ice Shelf in the Weddell Sea and the Ross Ice Shelf emerge as areas with zero sensitivity. This suggests that no 8 or 10 μm particles were simulated to originate from these areas, likely as a result of the low elevation (< 1 km) in these regions. For 10 μm particles, nearly the entire West Antarctic region shows zero emission sensitivity.

Emission sensitivities over SSA show considerable spatial variability across different particle sizes (Fig. 4.16). In general, a meridional emission sensitivity gradient is observed, increasing from north to south with the highest emission sensitivity generally located south of 45°S. For 2-5 μm particles, the highest emission sensitivity values are located along the east coast of SSA between 47-50°S. The emission sensitivity of coarser 8-10 μm particles is greatest at the inland region around ~47.5°S 70°W, but transport of these coarse particles is unlikely due to the strong influence of gravitational settling. The different locations of emission sensitivity hotspots between 2-5 and 8-10 μm particles suggest that different atmospheric processes, such as fronts, foehn winds, or land/sea breezes, likely govern dust entrainment and transport in these regions. Further research is needed to investigate the different local atmospheric processes behind this difference in emission sensitivity hotspots, but this work is beyond the scope of this study.

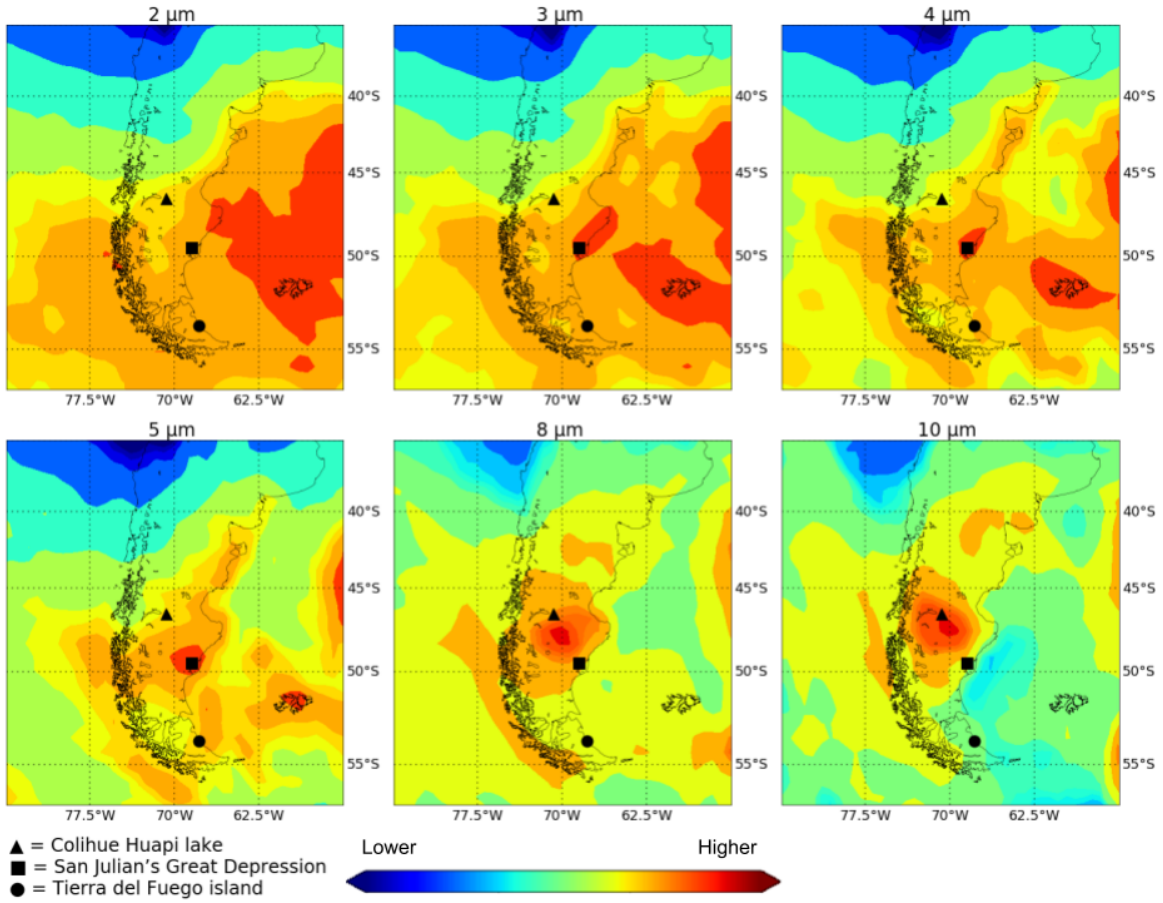

Figure 4.16 Same as Fig. 4.15 but zoomed in over SSA. Emission sensitivity values are normalised to a relative scale to emphasise hotspot regions. The shapes locate modern dust activity hotspots based on observational studies.

4.2.3 Sensitivity of dust back trajectories to particle size and seasonality

The sensitivity of dust transport to particle size and seasonality is investigated to determine whether these two factors are important drivers of dust transport over time. Both dust back trajectories and emission sensitivity are explored in relation to particle size and seasonality.

Back trajectory clusters grouped into seasons are shown in Fig. 4.17. The differences between seasons for both 600 and 1500 m.a.g.l. release heights are subtle, and no clear seasonal pattern is distinguishable (Fig. 4.17). While Fig. 4.17

only features 2 μm particle trajectories, the same results are seen for 5 and 10 μm particles. Hence, seasonality does not seem to have a significant effect on transport pathways.

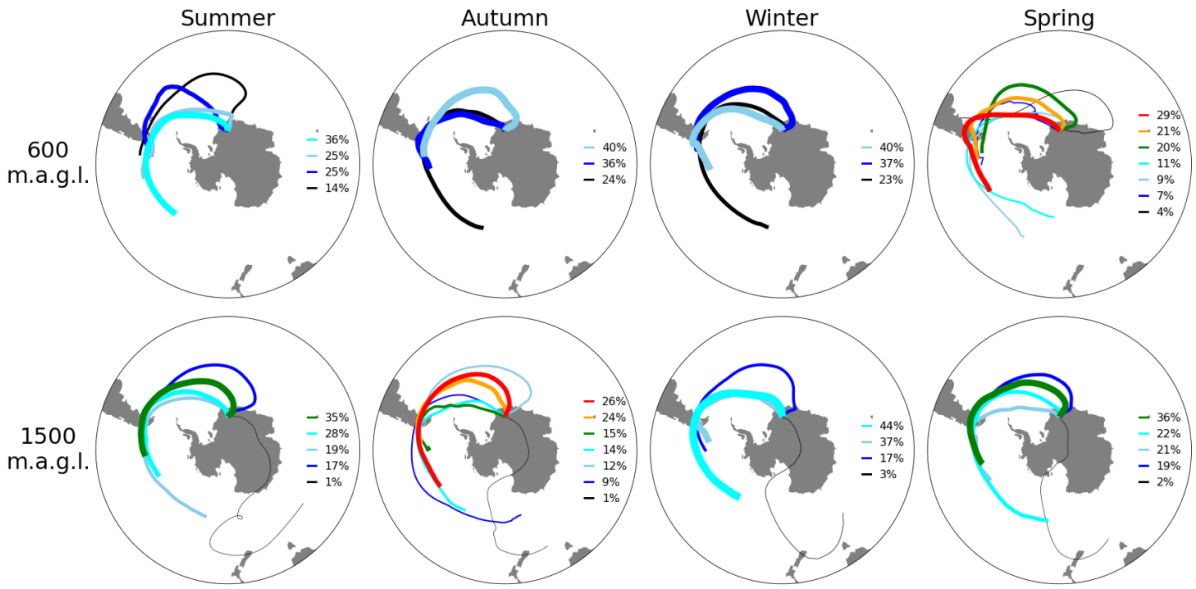

Figure 4.17 10-day back trajectory clustering across seasons (columns) and release heights (row).

Similarly, the overall emission sensitivity pattern is largely the same across seasons (Fig. 4.18). This again indicates that the spatial pattern of emission sensitivity does not change significantly across particle size and seasonality. However, while the overall emission sensitivity patterns across seasons are similar, some regional differences are notable. These regional differences also vary across particle size and do not show any systematic pattern. The only clear and consistent signal across all particle sizes is the higher summer emission sensitivity over the East Antarctic Plateau, indicating stronger influence from polar easterlies during this season.

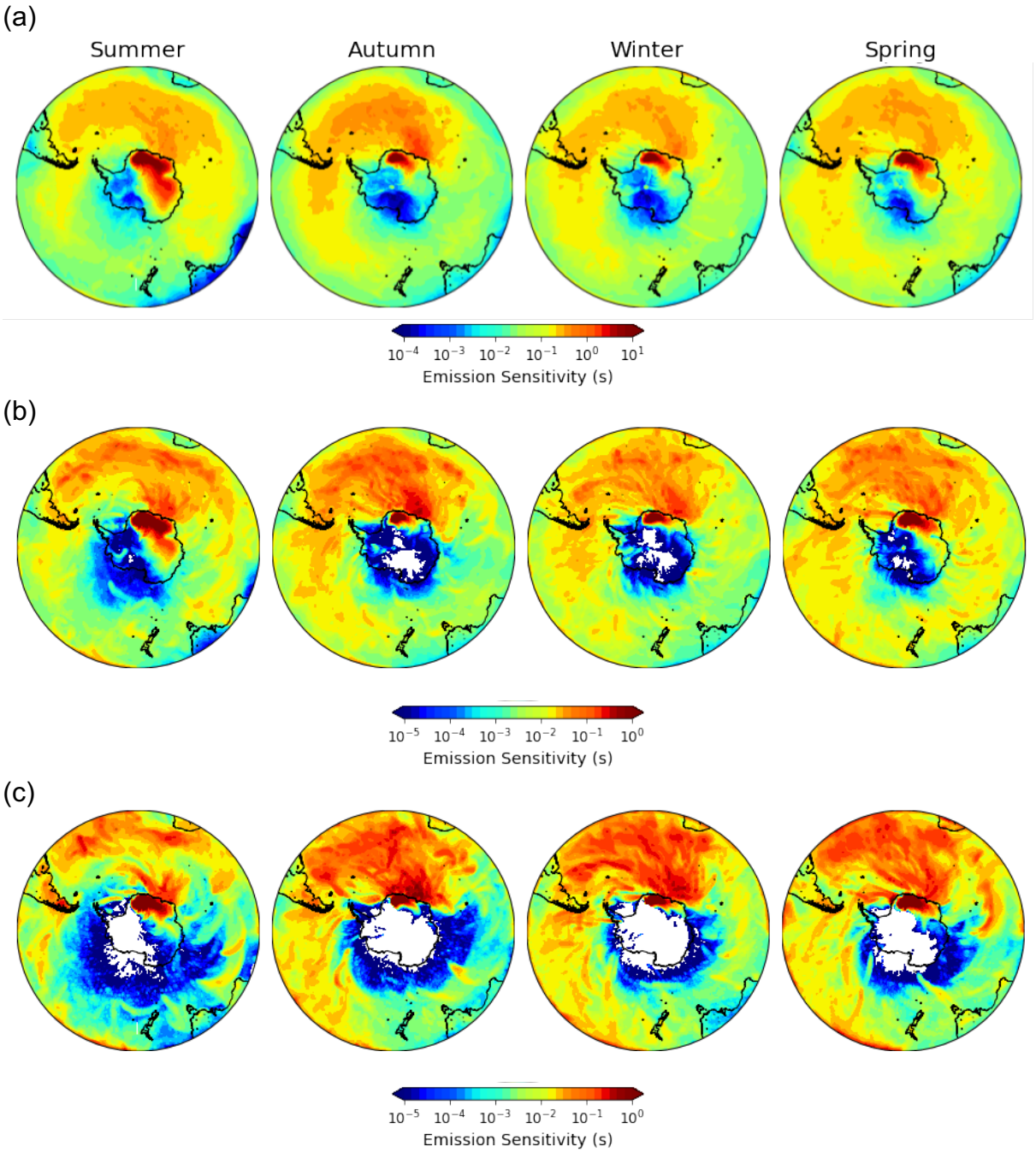

Figure 4.18 Average seasonal emission sensitivity for (a) 2, (b) 5, and (c) 10 μm particles. Colour scaling is different for each particle size to highlight spatial patterns. White areas denote zero emission sensitivity, in other words, no particles are simulated to originate from these regions.

Over SSA, the emission sensitivity values show more size-specific regional patterns rather than an overall seasonal signal across all particle sizes. For 2 μm particles, autumn-spring generally have higher sensitivity compared to summer (Fig.

4.19a), and autumn emission sensitivity best matches the 2 μm sensitivity hotspot region in Fig. 4.16. Potential transport of 2 μm particles from SSA is therefore strongest during autumn and weakest during summer. For 5 μm particles, the simulations show highest sensitivity during summer and autumn, and weakest during winter (Fig. 4.19b). The 5 μm hotspot region in Fig. 4.16 closely matches the summer and autumn emission sensitivity patterns therefore again suggesting that atmospheric circulation patterns are most conducive for transport of 5 μm particles during these seasons. Lastly, 10 μm particles show the highest emission sensitivity values in summer (Fig. 4.19c), and the spatial pattern is consistent with the 10 μm hotspot in Fig. 4.16. This high emission sensitivity signal during summer for 10 μm particles is more prominent than the highest seasonal sensitivities in other particle sizes, suggesting a more pronounced summer transport for 10 μm particles relative to 2 and 5 μm particles. For 2 and 5 μm particles, emission sensitivity patterns are relatively more equally spread out across seasons indicating dust transport is more constant throughout a year compared to 10 μm particles.

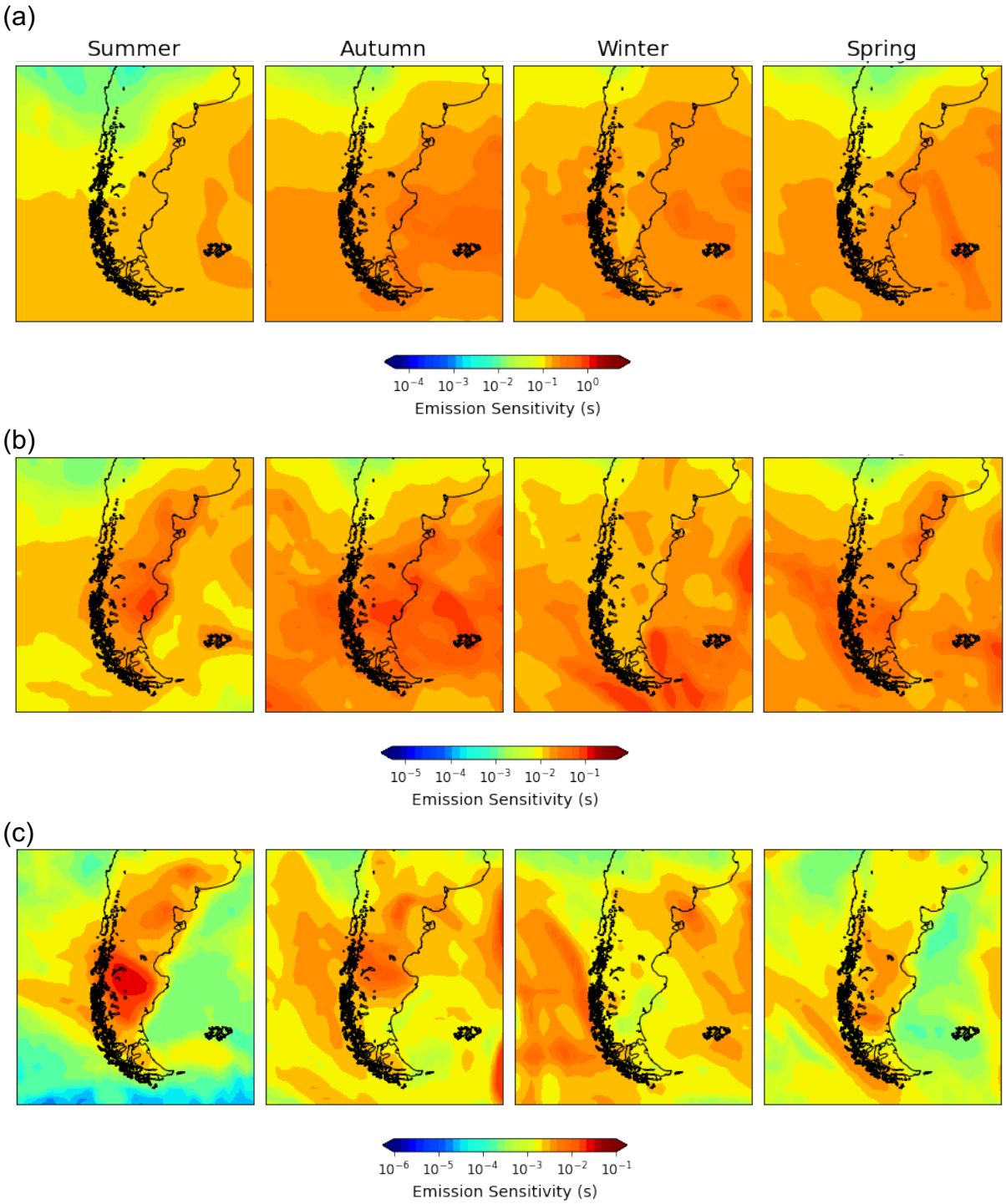

Figure 4.19 Same as Fig. 4.18 but zoomed in over SSA. Colour scaling is different for each particle size to highlight spatial patterns.

4.3 Dust-climate relationships over the past 40 years

4.3.1 Correlations using annual averages

The dominant circulation pattern associated with dust CPP variability at the ice core site is a low-pressure system over Drake Passage (Fig. 4.20). To fully characterise dust-climate patterns vertically in the atmosphere, multiple pressure levels are plotted in Fig 4.20. Positive dust CPP anomalies at the ice core site show a significant relationship with negative geopotential height anomalies over Drake Passage. The correlations are most pronounced in the 700 and 500 mb plots with an R-value ranging from -0.3 to -0.4 ($p < 0.10$) Lower geopotential heights translate to a deeper low-pressure system and stronger cyclonic/clockwise flow over the Drake Passage and is tied to increased dust CPP or larger particles transported to the ice core site. Conversely, higher values for geopotential height means higher pressure (or weaker low-pressure system) over the Drake Passage and smaller particles arriving at the ice core site. While the negative correlations could also indicate a high-pressure system over Drake Passage associated with smaller dust particles at the ice core site, the simulated trajectories in the previous section 4.2.1 do not show any dust transport pathway related to a high-pressure/anticyclonic circulation over Drake Passage. Hence, for all geopotential height correlations in this section, the assumption is that variability in circulation south of SSA only relates to deepening or weakening of low-pressure cyclonic systems. Aside from the low-pressure system over Drake Passage, the geopotential height correlation maps also generally show a wave-like zonally asymmetric pattern extending from the Drake Passage to the South Pacific. This structure suggests stronger influence from regional circulation anomalies rather than

a hemispheric-wide circumpolar pattern that is typically associated with the SAM. Based on these correlations, SAM therefore does not appear to be a major driver of interannual long-range transport of dust to the ice core site.

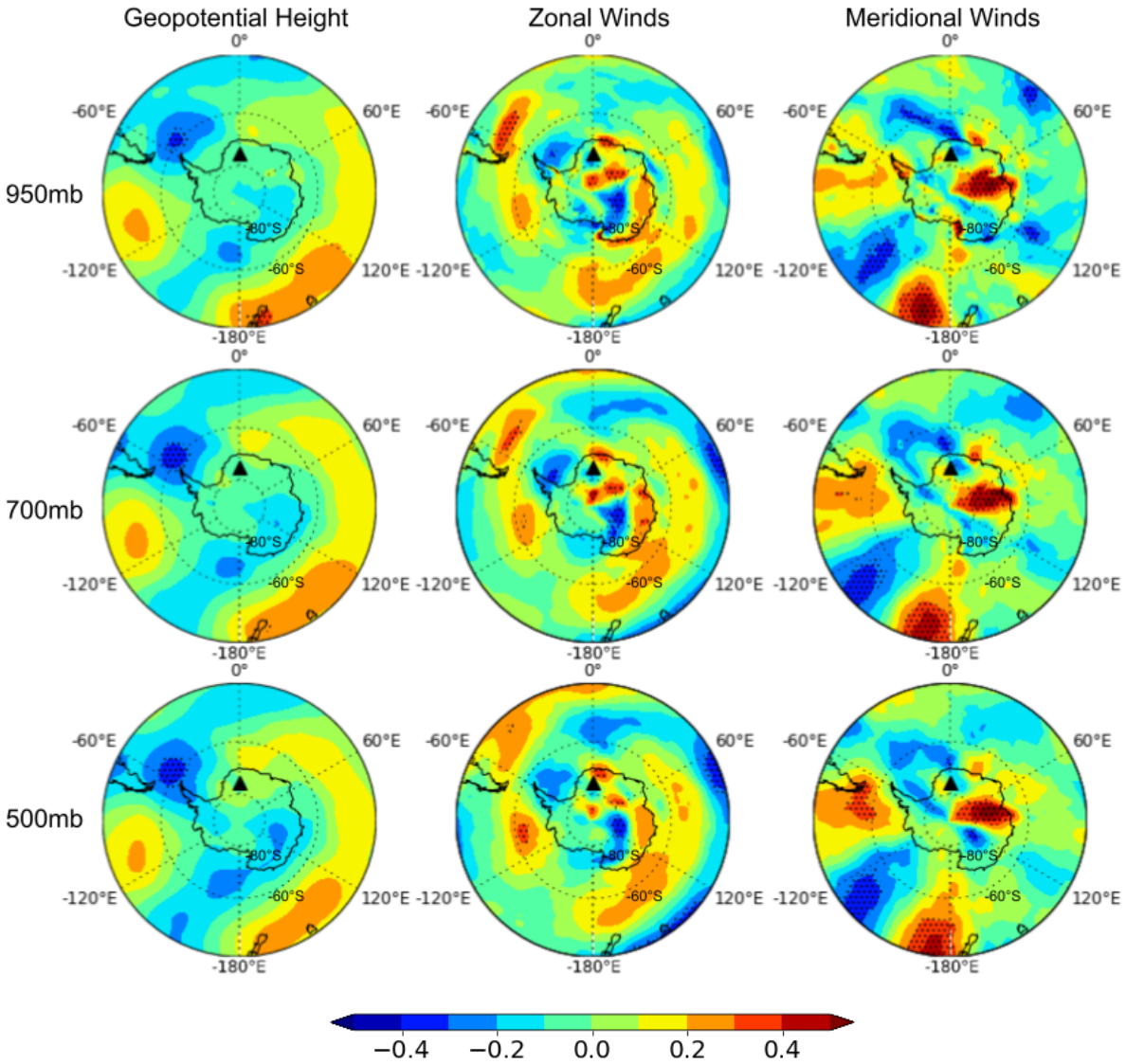

Figure 4.20 Correlations between annual average dust CPP at the ISOL-ICE site (black triangle) and annual average geopotential height, zonal winds, and meridional winds across different atmospheric pressure levels. All variables are detrended prior to calculating the correlations to highlight interannual variability between parameters. Hatching denotes statistical significance at $p < 0.10$.

Correlations with zonal winds show that the low-pressure system over Drake Passage is associated with westerly wind anomalies (positive correlation) over the SSA region across all pressure levels (Fig. 4.20). However, the positive correlation is most pronounced (and significant) in the near-surface 950 mb winds just east of SSA,

with R-values between 0.3 to 0.4, and therefore lower-level zonal wind flow likely has the strongest influence on dust transport to the site. This pattern is consistent with the fact that these regions of high zonal wind correlation are close to dust source regions over SSA, where particles emitted from the surface are likely still located in the lower levels of the atmosphere. The positive correlations indicate that stronger (weaker) westerly winds in the SSA region transports coarser (finer) dust particles from SSA to the ice core site. As previously discussed in section 2.1.3, stronger winds are required to transport larger dust particles due to the lower susceptibility of larger particles to wind transport compared to smaller particles.

In conjunction with zonal wind patterns, meridional winds also show significant correlations related to the cyclonic circulation over Drake Passage (Fig. 4.20). Negative correlations (northerly wind anomalies) are seen across a broad region north of the ice core site, with the highest R-values of -0.3 to -0.4 in the 700 and 950 mb levels located north of the ice core site. Therefore, northerly wind anomalies result in larger particles being transported to DML. Conversely, positive meridional wind anomalies are associated with weaker northerly winds, thereby impeding dust transport to Antarctica and transporting smaller particles. Significant correlations up to the 700 mb level can be explained by the high elevation (2892 m.a.s.l.) of the ISOL-ICE site with an average pressure around 600 mb. Compared to the SSA region, dust particles are transported at higher altitudes closer to Antarctica and therefore are correlated with meridional winds at higher atmospheric levels (lower pressure levels). This vertical profile of transport is consistent with findings from the Flexpart simulations wherein plume trajectories originating from SSA exhibit higher mean altitudes closer to Antarctica (Fig. 4.13).

Aside from wind patterns, precipitation in the SSA region is also significantly correlated with dust CPP at the ice core site (Fig. 4.21). In particular, a region of negative correlations is seen over eastern SSA at ~50°S, with R-values ranging from -0.3 to -0.5. The correlations indicate that lower (higher) amounts of precipitation over eastern SSA are associated with larger (smaller) particles at the ice core site. This relationship is expected as lower amounts of precipitation results in less wet removal of particles from the atmosphere and vice versa. Moreover, as discussed in the section 2.1.2, decreased precipitation lowers soil moisture content and interparticle cohesion thereby making land surfaces more conducive for dust emission. The opposite pattern for soil moisture content is true for higher amounts of precipitation. Between SSA and the ice core site, no other notable region of negative correlations is seen, suggesting that the influence of precipitation patterns is mostly constrained to the SSA region. This regional relationship can be explained by the fact that the highest dust concentrations in the entire transport pathway are typically located over source regions, and dust entrainment (influenced by soil moisture) and wet removal of particles are most strongly affected by precipitation over the SSA region. Apart from the region between SSA and the ice core site, Fig. 4.21 shows other areas with significant correlations such as over East Antarctica and New Zealand. However, these regions are excluded from further investigation since they are not within the area influenced by the regional circulation over Drake passage.

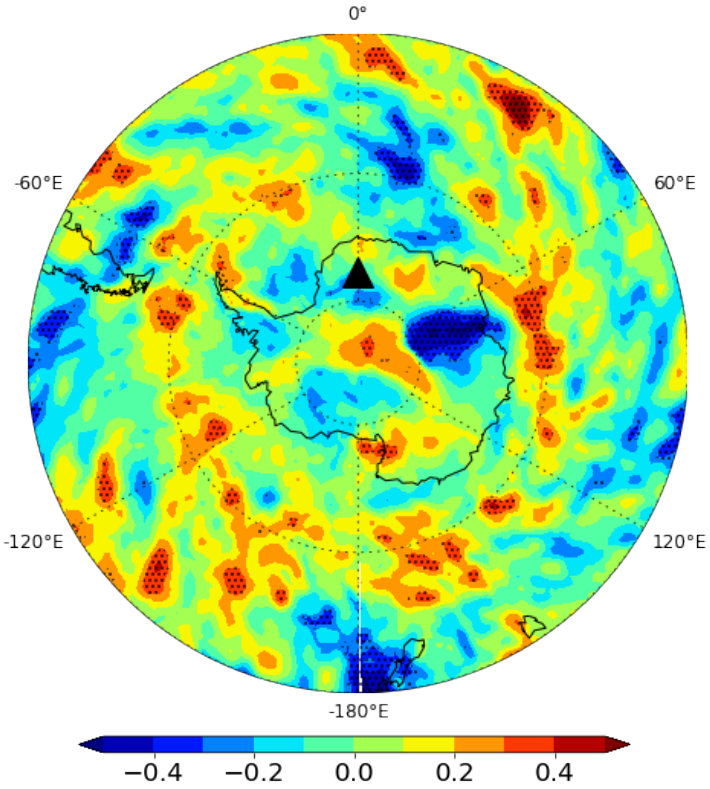

Figure 4.21 Same as Fig. 4.20 but for total precipitation.

To determine connections of the regional circulation pattern over Drake Passage with large-scale circulation patterns, correlation maps spanning the South Pacific and South Atlantic basins are plotted in Fig. 4.22. The circulation pattern over Drake Passage appears tied to a Rossby wave train emanating from the central tropical Pacific near the exit region of the subtropical jet (Ding et al. 2012). Alternating positive and negative correlations of 500 mb geopotential height are detected following the white line in Fig. 4.22a. The correlation map indicates that the Rossby wave train manifests as a low-pressure anomaly in the subtropics (~160°W, 20°S), a high-pressure anomaly in the mid latitudes (~160°W, 50°S), and finally a low-pressure system over Drake Passage. Similarly, the 300 mb stream function shows alternating correlations in the upper troposphere (Fig. 4.22b), depicting the same wave pattern as in the 500mb geopotential height plot. However, the stream function shows an additional upper level correlation cell near the equator (~170°W, 5°S). The negative

stream function correlations in this region (positive upper-level pressure) reflect enhanced tropical convection as shown in the red box in Fig. 4.22c. The significant negative correlation with outgoing longwave radiation indicates colder and higher cloud tops translating to increased tropical convection. Convective activity in this region therefore likely triggers Rossby waves traveling to Drake Passage. These Rossby wave patterns are generally associated with positive SST anomalies across the central tropical Pacific resembling El Niño conditions, but the SST correlations are generally weak and insignificant (Fig. 4.22d). Furthermore, ENSO variability is known to influence circulation farther west in the Amundsen Sea region rather than over Drake Passage (Li et al., 2021). Based on these correlation maps, ENSO therefore does not appear to be a major driver of the tropical teleconnections to Drake Passage, and it is more tied to localised convective variability in the central tropical Pacific. The exact cause of convective variability in this region may be tied to a number of climate patterns, including the Madden Julian Oscillation (Rondanelli et al., 2019), variability in the South Pacific Convergence Zone including mid-latitude wave activity (Matthews, 2012), and internal variability. Understanding the exact mechanism driving convection in this region is outside the scope of this study.

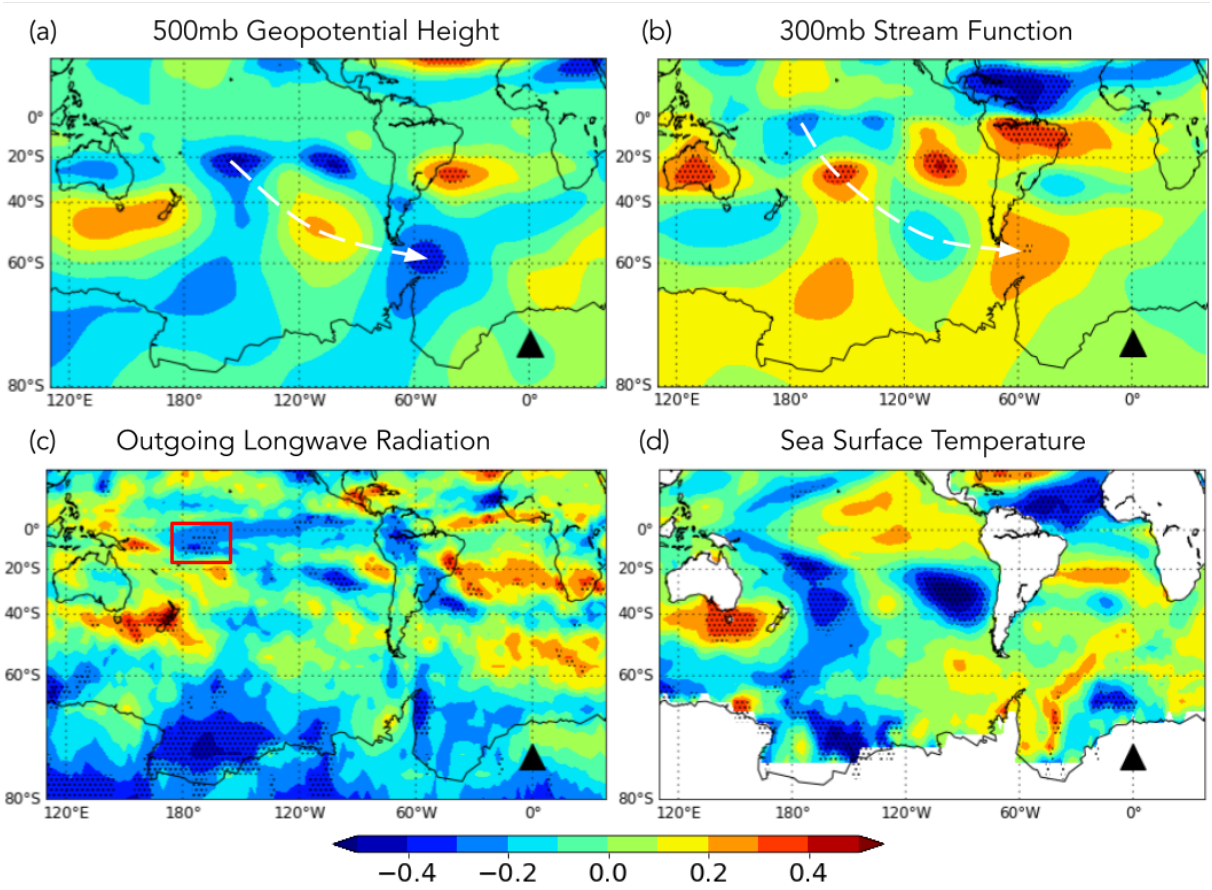

Figure 4.22 Correlations between annual average dust CPP at the ISOL-ICE site (black triangle) and annual average (a) 500mb geopotential height, (b) 300mb stream function, (c) outgoing longwave radiation, and (d) sea surface temperature for the period 1979-2017. All variables are detrended to highlight interannual variability between parameters. Hatching denotes statistical significance at $p < 0.10$.

4.3.2 Correlations using seasonal averages

The discussed annual average correlation plots are indicative of the most consistent annual signal between dust CPP at the ice core site and the various atmospheric/climate parameters. However, annual average values smooth out seasonal patterns, which can be very different from the annual mean especially since the structure of the atmospheric circulation across the SH varies significantly across seasons (e.g., Ding et al. 2012). Hence, seasonal correlations are investigated to determine how dust-climate relationships change throughout a year. Again, the seasonal grouping in this study is split into winter-spring and summer-autumn as

discussed in section 3.3.2. Additionally, since the seasonal correlation patterns show similar patterns across pressure levels as in the annual plots, only select levels are presented in Fig. 4.23.

During winter-spring, the geopotential height correlation map shows a dominant circulation pattern related to a broad low-pressure region centred just west of the Antarctic Peninsula (Fig. 4.23). The correlations values range from -0.3 to -0.5 and are significant at $p < 0.10$. The extent and location of this pattern is reminiscent of the Amundsen Sea Low (ASL; Turner et al., 2013) and from hereon will be referred to as such. Deepening of the ASL appears to be accompanied by a high-pressure/anticyclonic system north of the ASL. Zonal winds sandwiched by the two circulation anomalies produces significant westerly wind anomalies over a broad region from the South Pacific to the South Atlantic, with the highest R-values (0.4-0.6) over the SSA region. Similar to the annual correlation maps, a positive zonal wind correlation translates to stronger westerlies related to higher CPP or larger dust particles at the ice core site. For meridional winds, the correlation map shows an elongated region of significant negative correlations (northerly wind anomalies) just east of the Antarctic Peninsula extending from about ~55°S to the South Pole. The R-values for this region range from -0.3 to -0.4, and the negative correlations indicate northerly winds bringing larger particles to the ice core site. Notably, the region of negative correlations is west of the ice core, indicating that southward dust transport occurs closer to the Antarctic Peninsula. However, since the polar easterlies become more dominant in more inland regions over Antarctica, southward dust transport is likely most pronounced at the northern tip of the elongated negative correlation region, northeast of the Antarctic Peninsula. In terms of precipitation, deepening of the ASL is

linked to less precipitation over eastern SSA, particularly at ~50°S extending eastward off the coast. The computed R-values are significant and range from -0.3 to -0.4. Again, less precipitation allows for increased dust entrainment and less wash-out of particles from the atmosphere. The opposite pattern is true for higher amounts of precipitation.

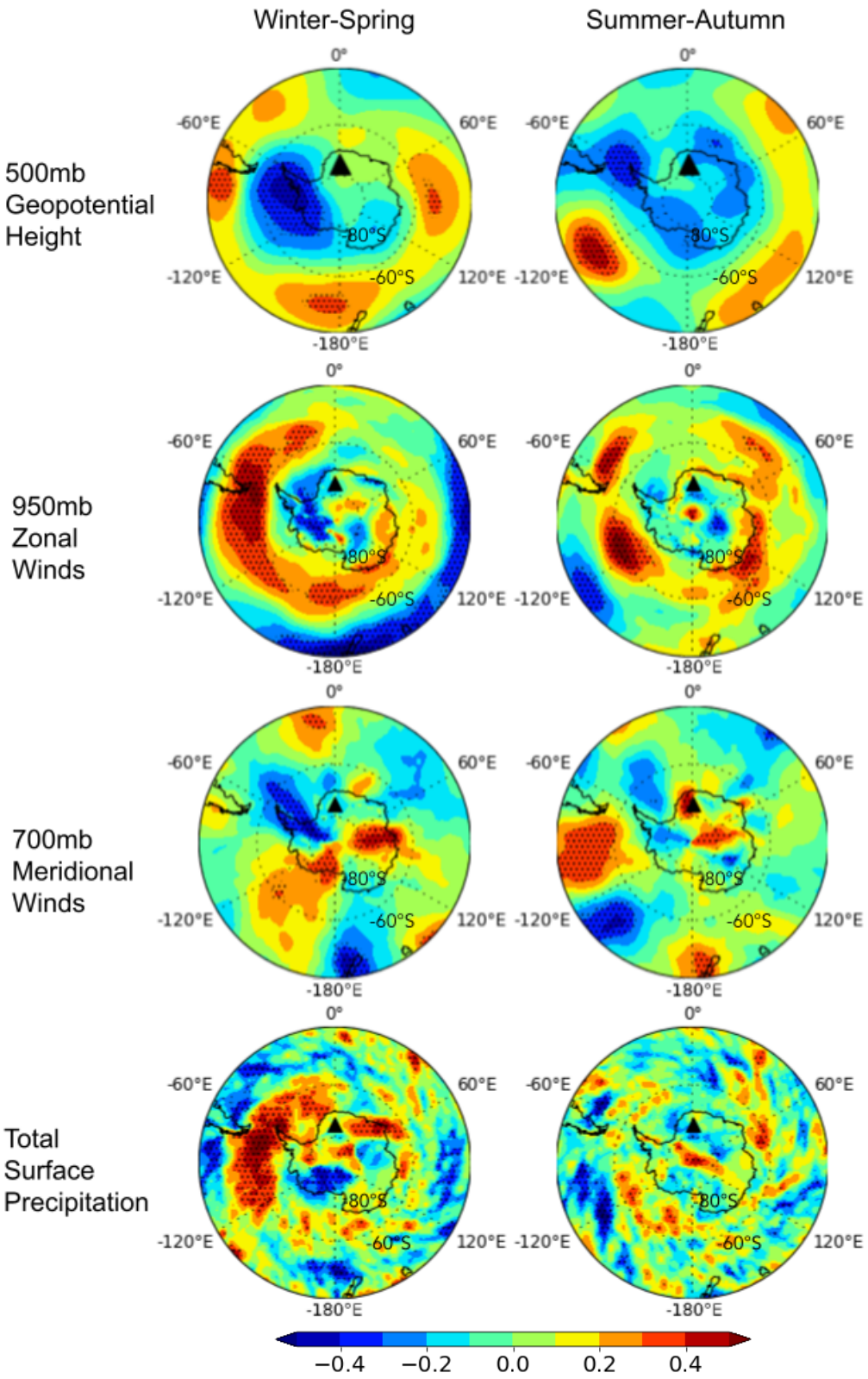

Figure 4.23 Correlations between seasonal average dust CPP at the ISOL-ICE site (black triangle) and seasonal average geopotential height, zonal winds, meridional winds, and total precipitation. All variables are detrended to highlight interannual variability between parameters. Hatching denotes statistical significance at $p < 0.10$.

During summer-autumn, increased dust transport to the ice core site is associated with a low-pressure system over Drake Passage (Fig. 4.23), with significant negative correlations for geopotential height in this region ranging between -0.3 to -0.4. The cyclonic circulation related to the low-pressure system brings westerly winds over the SSA region as seen in the positive zonal wind correlations just east of SSA, with R-values ranging from 0.3 to 0.5. Comparatively, meridional wind correlations are not as strong as that of zonal winds. Negative correlations with meridional winds are seen over the Weddell Sea region, extending as far north as 50°S, but the correlations are weak, with R-values from -0.2 to -0.3. Nonetheless, the negative correlations still indicate stronger northerly winds over this region favouring enhanced poleward transport of dust particles. Similar to winter-spring, drier conditions over the eastern coastal SSA region (~50°S) are associated with larger particles being transported to the ice core site, with correlation values for precipitation ranging from -0.3 to -0.4.

Deepening of the ASL during winter-spring appears to be induced by a wave train originating over Australia. Both 500 mb geopotential height (Fig. 4.24a) and 250 mb stream function (Fig. 4.24b) show consistent correlation patterns associated with alternating pressure systems. A low-pressure anomaly is situated over Australia followed by a high-pressure anomaly southeast of New Zealand and then the deep ASL centred just west of the Antarctic Peninsula. Significant correlations for both geopotential height and stream function are computed with correlation strengths between 0.3-0.6. Moreover, the low-pressure system over Australia and the high-pressure system southeast of New Zealand exhibit an elongated structure and appear to be part of a latitudinal band of similar correlations extending eastward to the South Atlantic as most clearly seen in the stream function plot. The locations and elongated

structures of the pressure systems reflect variability in the subtropical jet, which is noted to be most pronounced and distinct from the eddy-driven polar front jet during winter (Gallego et al., 2005; Gillet et al., 2021). Notably, perturbation of the SH subtropical jet is known to be related to Rossby wave propagation towards Antarctica during non-summer months (e.g., Ding et al., 2012; Clem & Fogt, 2015).

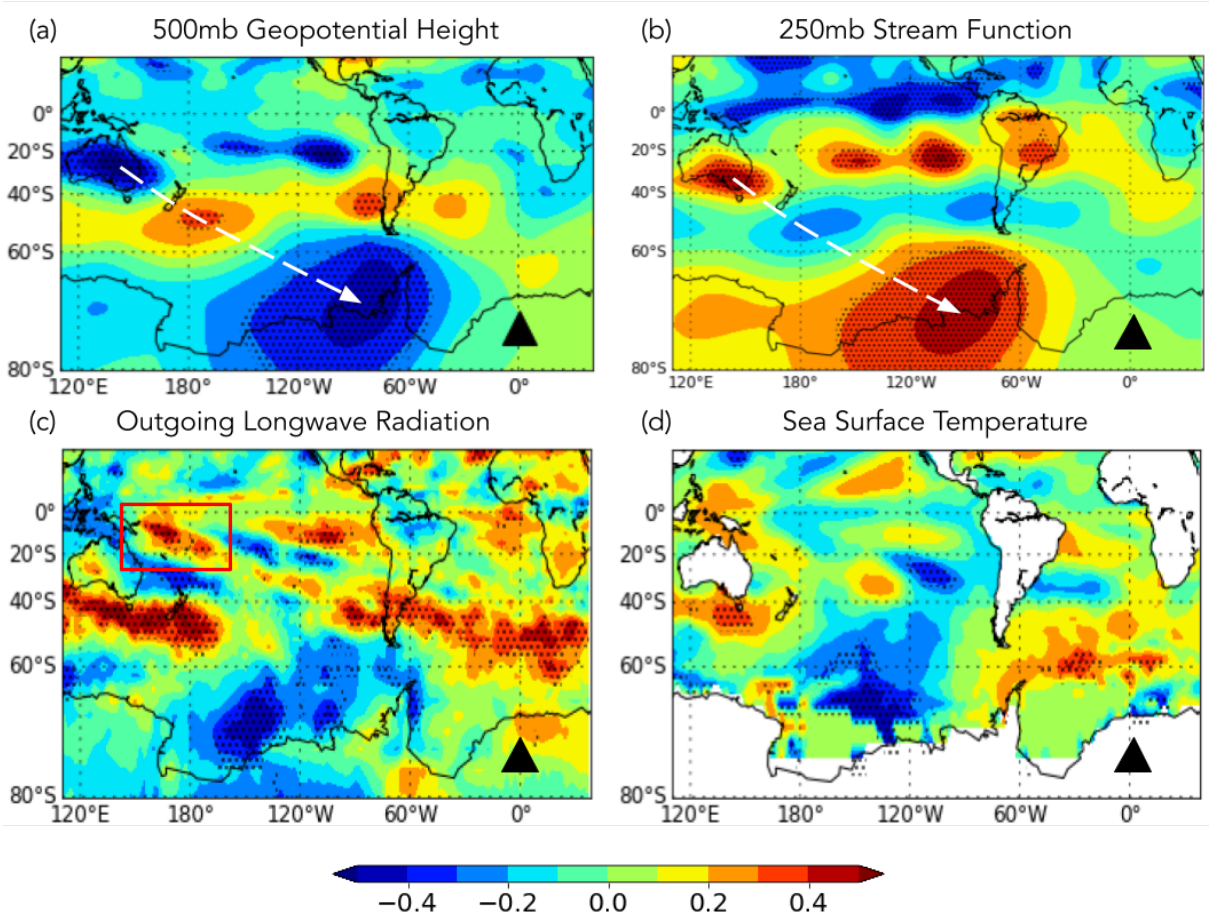

Figure 4.24 Same as Fig. 4.22 but for winter-spring averages.

The origin of the wave train appears to be linked to suppressed tropical convection northeast of Australia in the South Pacific Convergence Zone (SPCZ; Vincent, 1994; Brown et al, 2020), shown by a diagonal band of positive correlations seen from Papua New Guinea extending south-eastward (Fig. 4.24c). Suppressed convective activity in the SPCZ during winter can generate an anomalous Rossby wave source along the subtropical jet, which has previously been shown to produce a

cyclonic anomaly near the Antarctic Peninsula in winter (Clem et al. 2019). While studies have suggested subtropical jet variability related to ENSO activity (e.g., Ding et al., 2012; Gillet et al., 2021), the lack of significant correlations with SST over the tropical Pacific indicates that in this particular case, ENSO does not appear to be associated with this circulation pattern (Fig. 4.24d).

In the summer-autumn semester, the low-pressure system over Drake passage is part of a Rossby wave train emanating near the dateline just south of a local region of enhanced deep convection. Alternating low- and high-pressure systems are detected starting with a high near 180°W 15°S, a low ~150°W 30°S, a high ~120°W 50°S, and the low over Drake Passage (Fig. 4.25a & b). The strength of the correlations for both geopotential height and stream function correlation maps range from 0.2-0.6. At ~180°W 20°S, the negative correlations for stream function appears to be tied to an off-equatorial band of deep convection in the SPCZ region (Fig. 4.25c), which again can trigger poleward wave propagation resulting in a low-pressure system over Drake Passage during summer (Clem et al. 2019). Similar to winter-spring, dust CPP at the ice core site during summer-autumn do not have any significant correlation with SST in the tropical Pacific (Fig. 4.25d), thereby indicating that the discussed Rossby wave likely occurs largely independent of ENSO.

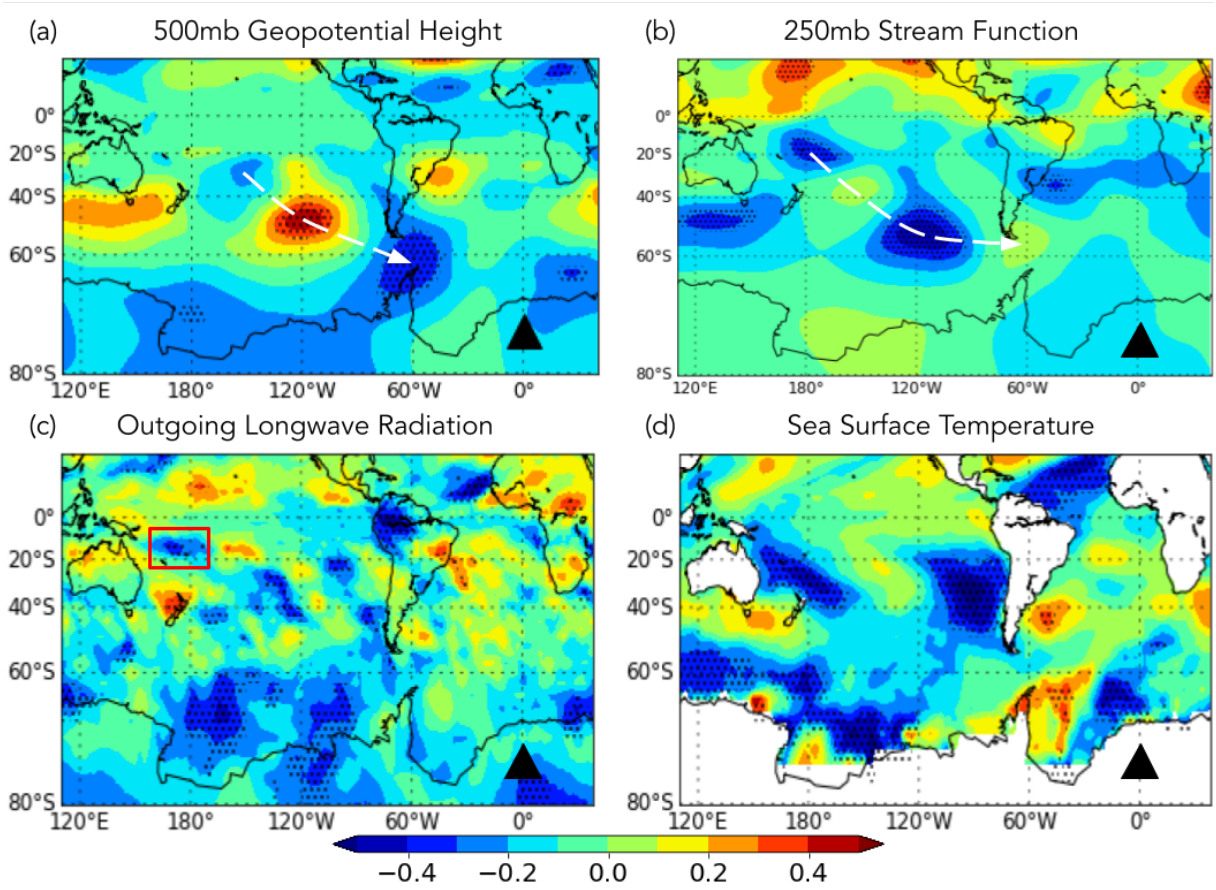

Figure 4.25 Same as Fig. 4.22 but for summer-autumn averages.

4.3.3 Correlations with large-scale climate patterns

The correlation maps in the previous section suggests that the large-scale atmospheric circulation patterns leading to the Drake Passage cyclone are not significantly related to ENSO or SAM. To further investigate this, correlations between dust CPP at the ice core site and large-scale climate patterns are computed. Consistent with the previous results, neither ENSO nor SAM show any significant correlation with dust CPP at the ice core site (Fig. 4.26). The only significant correlation is between PDO and dust CPP during summer-autumn. The R-value is weak (R=0.2), but the correlation is significant at the 95 % confidence level, implying that more positive (negative) PDO phases are related to relatively larger (smaller) dust particles being transported to the ice core site during this semester. This is consistent

with Clem et al. (2019) showing variability in SPCZ convection is significantly related to variability in the PDO. The weak correlation is likely due to the poor interannual correspondence between the PDO index and dust CPP. However, on decadal time scales there is a stronger correspondence between the PDO and CPP when considering the entire period from 1900-2017 (Fig. 4.26). Relatively high CPP are associated with positive PDO values from 1900-1940, both of which then sharply decline in the 1940s. This is followed by a period of relatively low/negative values between the 1950s to the mid-1970s, and then increasing to a period of higher values from the 1980s onwards. This long-term correspondence indicates that the relationship between PDO and dust CPP at the ice core site is important over multi-decadal timescales rather than over interannual timescales, likely through modifying decadal variability in deep convection over the SPCZ. This multi-decadal relationship is expected as PDO patterns are most pronounced over this timescale. Additionally, the multi-decadal timescale of influence also explains why correlations with the Southern Oscillation Index (SOI) are not significant as ENSO variability operates on shorter interannual timescales.

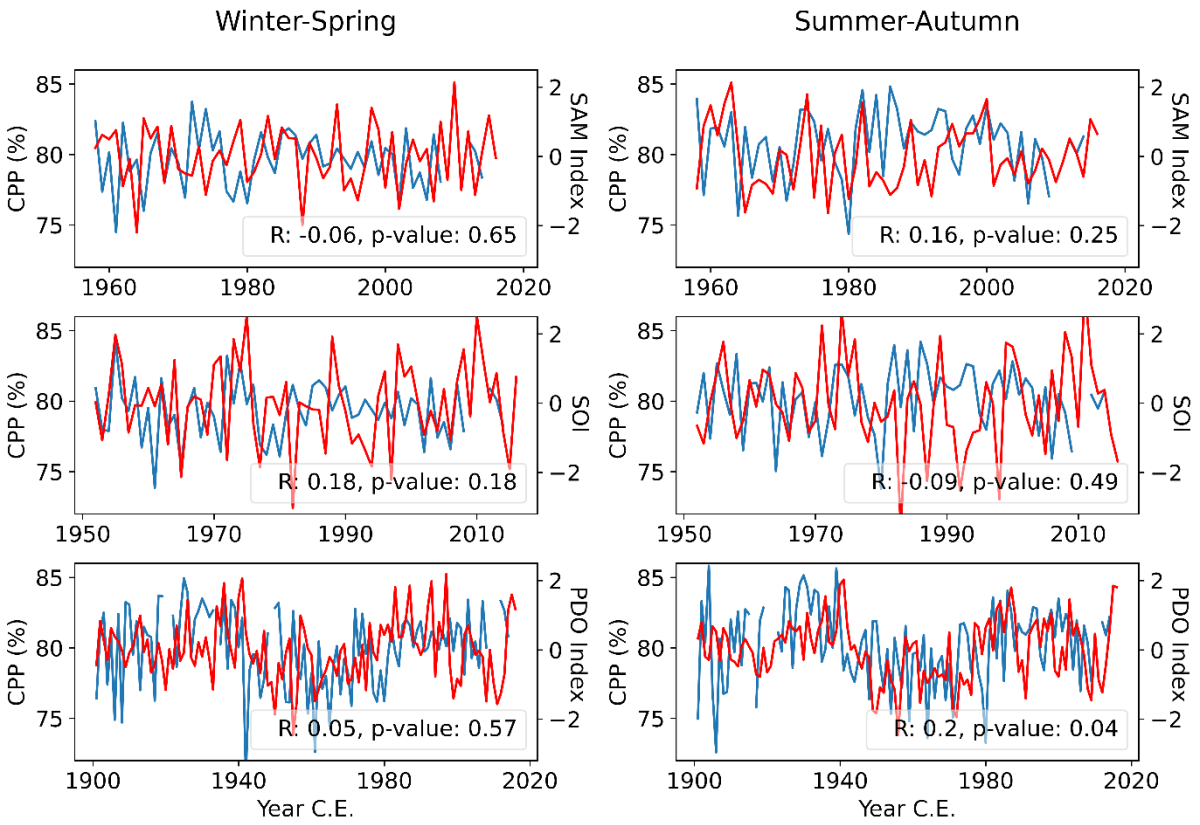

Figure 4.26 Winter-spring (left) and summer-autumn (right) average dust CPP and SAM index (top), SOI (middle), and PDO index (bottom) for varying time periods. The blue line denotes dust CPP and the red line, the specific index. All variables are detrended to highlight interannual variability between parameters. Correlation values and statistical significance are noted on the bottom right of each plot.

5. DISCUSSION

This chapter focuses on synthesising the results to address the objectives (section 1.3) and answer the overall research question of this study: From where and how is dust transported to high-elevation DML, Antarctica over the satellite era? Based on the findings over of satellite era, implications for dust deposition variability to high-elevation DML over the last millennium are suggested.

5.1 Dust source and transport over the satellite era

5.1.1 Dust Source

The results consistently point to SSA, south of ~45°S, as the dominant PSA for long-range transported dust to the ISOL-ICE site over the satellite era. Several lines of evidence support this finding. Firstly, the observed PSD with a mode of 3.7 μm (Fig. 4.9) is within the typical size range of long-range transported dust to Antarctica (e.g., Koffman et al., 2014, Wegner et al., 2015). As discussed in section 2.1.3, fine particles (< 5 μm) have the potential to be transported long distances at high altitudes within the troposphere due to inefficient gravitational settling. Similarly, ice cores from the high elevation EDML (Wegner et al., 2015) and EPICA Dome C (Delmonte et al., 2002) sites both report size modes between ~1.6-3.0 μm during the Holocene and have been linked to long-range transport of dust particles from remote Southern Hemispheric continents. Secondly, the dust flux of ~0.3 mg m^{-2} yr^{-1} over the satellite era is comparable to estimates from other high-elevation East Antarctic ice core sites (0.28-0.54 mg m^{-2} yr^{-1}) receiving dust from remote sources during the Holocene (Delmonte et al., 2019). Third, at least 98 % of Flexpart plume trajectories passing over sub-Antarctic land areas originate from SSA (Fig. 4.11). Forward trajectory modelling of air-parcels from Neff & Bertler (2015) also confirm that trajectories from SSA most frequently pass over the EDML/ISOL-ICE site compared to trajectories originating from New Zealand, Australia, and South Africa. Fourth, when considering only sub-Antarctic source regions, the ISOL-ICE site is most sensitive to dust emissions from SSA (Fig. 4.15). Lastly, the majority of the correlation maps (Fig. 4.20, 4.21, & 4.23) show the highest correlations in the SSA region, suggesting a connection between SSA and

dust deposition at the ISOL-ICE site. The highest wind – CPP correlations are mostly from zonal wind anomalies in the SSA region related to cyclonic circulation south of SSA (Fig. 4.20 & 4.23). Furthermore, negative correlations for precipitation are consistently seen in the SSA region ~50°S (Fig. 4.21 & 4.23). The location of these correlations over SSA provides compelling evidence that interannual dust deposition variability at the ISOL-ICE ice core site is explained by wind flow and precipitation patterns in the SSA region. The remote PSA of SSA is further supported by radiogenic isotope and rare earth element analysis indicating SSA as the dominant origin for East Antarctic (including DML) dust during the glacial period and a major contributor of dust for the Holocene and present day (Wegner et al., 2012; Delmonte et al., 2019, 2017; Gili et al., 2017; Bory et al., 2010**)**.

In terms of the PSA in SSA, the emission sensitivity patterns over SSA show localised hotspots in the eastern coastal regions between 47 and 50°S for fine 2-5 μm particles and inland (47.5°S 70°W) for coarser 8-10 μm particles (Fig.4.16). The high emission sensitivity over these regions is consistent with negative precipitation correlations in the same area (Fig. 4.21 & 4.23). As discussed, drier conditions are more conducive for dust generation at source regions. The emission sensitivity hotspots also coincide with the locations of active dust regions in SSA (Fig. 4.16). In particular, 3-5 μm particles have emission sensitivity hotspots that encompass the San Julian's Great Depression (49.5°S 68.5°W), an area characterised by topographic depressions and desiccated lakes. Strong dust activity in this region is exemplified by the satellite-observed dust event between 22 and 26 June 2006 (Li et al., 2010). Comparatively, emission sensitivity hotspots for 8-10 μm particles are centred close to the Colihue Huapi lake (46.56°S 70.74°W), another desiccated lake considered to

be the largest dust source in SSA. Satellite aerosol detection and surface synoptic observations confirm strong dust activity in this region over the last ~50 years (Gassó et al., 2010; Gassó & Torres, 2019). Lastly, dry lakes in the vicinity of the Tierra del Fuego Island (53.8°S 67.8°W) are also known for notable dust events. An example of these events was observed through satellite detection on 26 February 2005, with a prominent dust plume extending into the eastern ocean region (Fig. 2.8; Gassó et al., 2010). While Tierra del Fuego does not fall into any of the observed emission sensitivity hotspot regions, it is still within the second highest contour of emission sensitivity values especially for 2-4 μm particles (Fig. 4.16). For the late Quaternary glacial periods, geochemical evidence points to Patagonia/Tierra del Fuego as the dominant dust source region in SSA (Basile et al., 1997; Grousset et al., 1992), with additional inputs from lower latitude areas (Gili et al., 2016, 2017) such as the Pampean region in central western Argentina.

While SSA is the dominant dust PSA to the ISOL-ICE site, there is evidence of a non-negligible dust contribution from local Antarctic dust sources. Given that the size of dust particles in dust source regions is generally observed to be ~10 μm (Fig. 2.2) and the particle size of long-range transported dust to Antarctica is typically between 1-5 μm but < 10 μm (e.g., Koffman et al., 2014, Wegner et al., 2015), the presence of large coarse particles deposited at the ice core site (Fig. 4.7) are indicative of contribution from nearby Antarctic dust sources, such as from the Heimefrontfjella mountain ranges in the coastal DML region. This is supported by analysis of rare earth elements in the EDML ice core, suggesting some dust contribution from local Antarctic dust sources during the last glacial period (Wegner et al., 2012), and radiogenic isotopes measured on dust representing the period 1700 to 1997 CE extracted from

the Camp Maudheimvidda ice core (73°06′19 ″S, 13°09′54 ″W; 360 m a.s.l) (Delmonte et al., 2019). Both geochemical evidences suggest dust contribution from local Antarctic dust sources. Furthermore, the highest emission sensitivities from the Flexpart simulations are also located over some parts of coastal DML, supporting potential contribution from exposed rock surfaces in these areas. However, it is difficult to determine the exact contribution from local sources versus long-range transported dust.

5.1.2 Dust transport

From source regions in SSA, dust particles are uplifted into the atmosphere to undergo long-range transport to the ISOL-ICE site. The particle size of long-range transported dust provides information about transport heights. Given an ISOL-ICE dust mode of 3.7 μm, the modelled back trajectory heights of particles between 2 and 5 μm (Fig. 4.13) suggest that dust particles are uplifted to at least ~1500 m.a.s.l. over SSA in order to be transported to the ISOL-ICE site. Notably, this modelled height requirement is consistent with a satellite-observed dust event in February 2005 showing dust was uplifted to 2000 m.a.s.l. near Tierra del Fuego (Gassó et al., 2010).

From the SSA region, dust particles are transported to the ISOL-ICE site dominantly through a low-pressure/cyclonic system south of SSA. Low-pressure/cyclonic systems play an important role in facilitating dust transport from SSA to East Antarctica as exemplified in Li et al. (2010). Importantly, while the cyclonic system south of SSA is the dominant identified mechanism by which dust is transported to the ISOL-ICE site, the significant correlation values between CPP and

500 mb geopotential height only range from 0.3-0.6 in magnitude (Fig. 4.20 & 4.23). The coefficient of determination (R^2) therefore indicates that this cyclonic pattern explains 10-36 % of the dust CPP variability at the ISOL-ICE site and additional factors such as other circulation patterns, source-related factors, or deposition processes influence interannual dust transport to the ISOL-ICE site.

Reanalysis data provides important insights into the drivers and mechanisms of dust transport on seasonal timescales. While the wind flow patterns from SSA to the ISOL-ICE site are similar across seasonal semesters, winter-spring circulation patterns show more prominent correlations with CPP compared to during summer-autumn. In particular, winter-spring zonal winds show a broader region of positive correlations encompassing SSA with correlations up to R=0.6, whereas summer-autumn correlations are constrained to a smaller region centred just east of SSA with correlations up to R=0.5 (Fig. 4.23). Additionally, winter-spring meridional winds show higher correlation values (-0.3 to -0.4) southeast of SSA compared to summer-autumn, which have R-values from -0.2 to -0.3. The more prominent wind correlations during winter-spring may be tied to the more zonally asymmetric (wavy) structure of the Southern Hemispheric circulation during winter and spring (Ding et al., 2012). Notably, the more prominent correlation patterns during winter-spring compared to summer-autumn are also consistent with the observed seasonal dust deposition at the ISOL-ICE site showing a maximum in winter-spring (Fig. 4.8). This winter/spring dust maximum is also noted in the Holocene as observed from the EDML ice core from Wegner et al. (2015). Furthermore, the winter-spring ASL correlation is not present in the annual average correlation maps, and instead, the low-pressure system over Drake Passage emerges as the dominant annual signal (Fig. 4.20). This suggests that

while the winter-spring ASL pattern is more pronounced than the summer-autumn low-pressure system over Drake Passage, the ASL signal is largely constrained to winter-spring, whereas the low-pressure over Drake Passage is more consistently observed throughout the year.

The size-specific seasonal patterns of emission sensitivity (Fig. 4.19) show some differences with the observed seasonal dust deposition at the ISOL-ICE site (Fig. 4.8) and the seasonal correlation maps of geopotential height (Fig. 4.23). Given ~3.7 μm is the observed particle size mode of long-range transported dust, seasonal emission sensitivities of 2 μm (Fig. 19a) and 5 μm (Fig. 19b) are used for comparison with the ISOL-ICE seasonal dust deposition record and the seasonal correlation maps. The ISOL-ICE site is most sensitive to emissions of fine particles (2-5 μm) between summer and autumn from the eastern coastal region of SSA (Fig. 4.19a & b). This indicates that atmospheric conditions and circulation patterns are most conducive for long-range transport of dust from SSA to the ISOL-ICE site during these seasons. The difference between the summer-autumn maximum in emission sensitivity (Fig. 4.19a & b) versus the strong winter-spring dust deposition (Fig. 4.8) and wind correlations (Fig. 4.23) suggests that while transport of 2-5 μm particles are optimal during summer-autumn (Fig. 4.19a & b), source conditions, such as soil sediment availability, are possibly more conducive for dust emissions during winter-spring. This could explain the difference between the seasonal emission sensitivity (Fig. 4.19a & b) versus the observed seasonal dust deposition (Fig. 4.8) since emission sensitivity does not take into account source conditions. Comparatively, the correlation analysis may partly capture variability in source conditions as well.

Cyclonic circulation variability south of SSA appears tied to the SPCZ on seasonal timescales and central Pacific convection on annual timescales. Variability in convective activity in the SPCZ is known to instigate Rossby wave propagation affecting cyclonic circulation south of SSA on a seasonal basis (Clem et al. 2019). In particular, during summer-autumn, enhanced convection in the SPCZ is associated with increased cyclonic activity over Drake Passage (Fig. 4.25), while during winter-spring, supressed convection in the SPCZ perturbs the subtropical jet leading to a deepening of the ASL centred just west of the Antarctic Peninsula (Fig. 4.24). Averaged annually, the summer-autumn and winter-spring seasonal patterns likely cancel out each other and hence do not emerge as a dominant Rossby wave pattern on an annual basis. Instead, Rossby wave propagation on annual timescales is triggered by anomalous convection in the central tropical Pacific, leading to increased cyclonic activity over Drake Passage (Fig. 4.22). A similar Rossby wave pattern is noted in Clem et al. (2020) for annual timescales, wherein a deep convective anomaly in the central tropical Pacific induces a wave train that increases cyclonic activity over the Weddell Sea.

The influence of particle size on dust transport is pronounced in the strength of transport (i.e., amount of transported dust) rather than the pathway. As discussed, stronger emission sensitivities are simulated for finer particles (Fig. 4.15), but the dust plume trajectories do not vary systematically across particle sizes (Fig. 4.11). In other words, the overall dust transport pathway from SSA to the ISOL-ICE site is largely the same across different particle sizes, but the strength of the transport is greater for smaller particles compared to larger particles. This is likely due to the lower initial altitude required for fine particles to be entrained in long-range transported dust from

SSA to the ISOL-ICE site. For example, 2 μm particles need to be uplifted to ~1500 m.a.s.l. over the SSA region, whereas 10 μm have to be transported vertically to a height of ~5000 m.a.s.l. over SSA to undergo long-range transport to the ISOL-ICE site (Fig. 4.13). In general, it is possible that coarse particles are transported to coastal Antarctica, such as at Roosevelt Island (Winton et al., 2016), but unlikely over the East Antarctic Plateau due to the high elevation

5.2 Implications for centennial scale ice core dust records

5.2.1 Spatial patterns of Antarctic dust deposition

Comparative analysis of Antarctic ice core dust records spanning the last century (Table 3.1) is done to contextualise dust deposition variability observed in the ISOL-ICE core. This section gives an overview of dust variability across the Atlantic sector of Antarctica over the last century. Dust fluxes are compared for particles < 10 μm to reduce the influence of locally sourced dust on the flux values and highlight dust deposition from long-range transported dust.

From 1850-2017, no other available record shows an abrupt increase in dust flux starting ~1915 as observed in the ISOL-ICE core (Fig. 5.1). Similarly, the WAIS record also does show an abrupt increase in the early-1900s (Koffman et al., 2014). The lack of a similar abrupt increase in the dust records for both 0.9-10 μm and 0.9-5.0 μm particles in Fig. 5.1, combined with the dust deposition characteristics at the ISOL-ICE site, suggests that the sudden shift is a regional high elevation DML signal compared to the lower elevation WAIS, JRI, and IND-25/B5 sites. Notably, the ISOL-

ICE record features a second spike in dust concentrations in the late-2000s as most clearly seen in 0.9-5.0 μm particles, but the other dust records do not cover this time period.

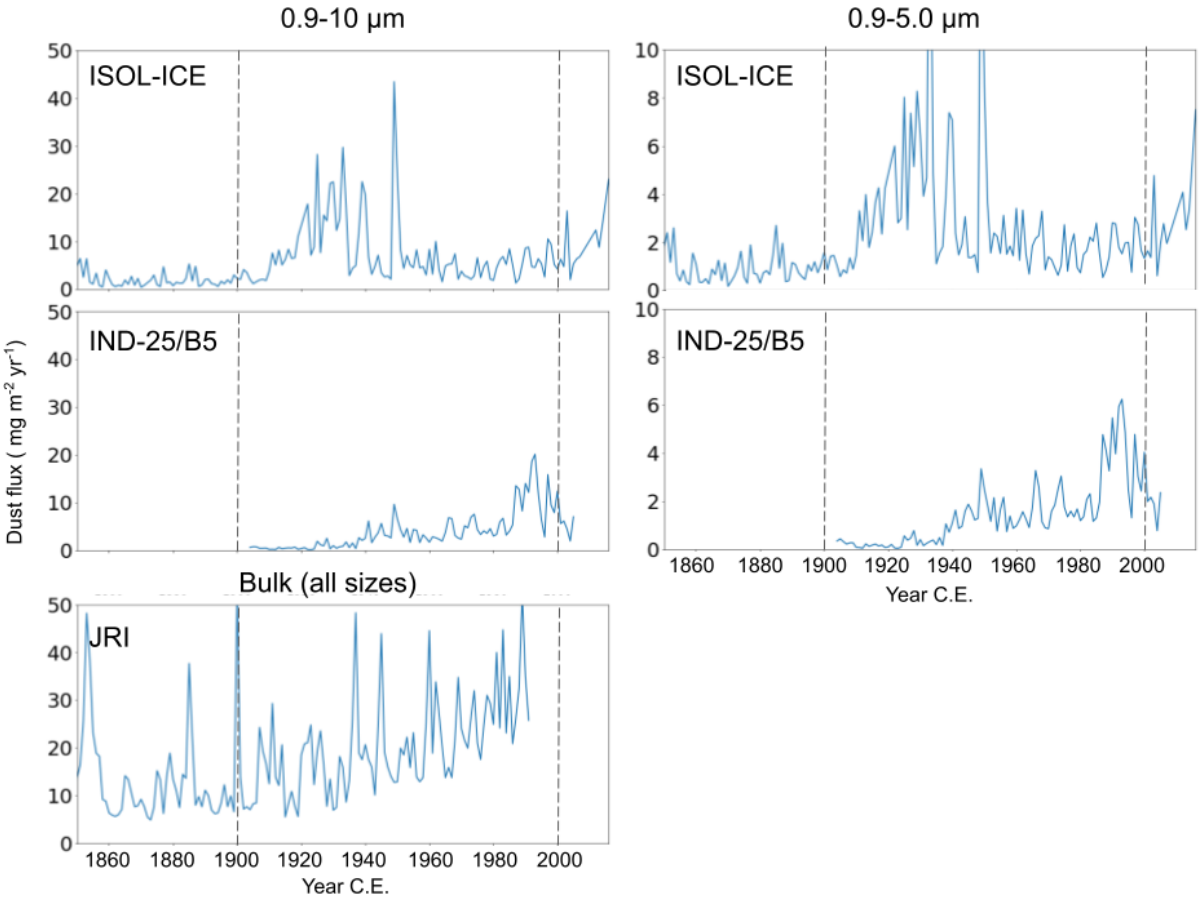

Figure 5.1 Comparison of ISOL-ICE, IND-25/B5, and JRI ice core dust fluxes from 1850-2017 CE. Blue lines are annual averages. Size bins are noted on top of each set of plots. No plot for JRI is shown for the 0.9-10 and 0.9-5.0 μm size range since the dataset only provides the total dust flux for all size bins and not particle size-segregated fluxes. Vertical dashed lines mark 1900 and 2000, showing the positive trend from the 1900 onwards and the second spike in fluxes in ISOL-ICE core after 2000.

The dust records from several ice core sites exhibit an overall positive trend in the past century but with differences in shorter-scale variability (Fig. 5.1). From ~1900 CE onwards, a similar overall positive trend is observed in the ISOL-ICE, IND-25/B5, and JRI sites. Notably, the WAIS dust record also shows increasing dust flux from ~1900 CE onwards (Koffman et al., 2014). The common trend over the last century

across all these ice core dust records indicate an Antarctic-wide increase in dust deposition over the last century. This widespread increase could be due to several factors, such as land use change (McConnell et al., 2007) and climate variability related to SAM, ENSO, and/or the PDO (e.g., Koffman et al., 2014; Laluraj et al., 2020). Additionally, while there is a clear overall positive trend in the records, shorter-scale variability is largely different across records. This possibly reflects differences in combinations of PSAs and regional transport patterns for each site.

5.2.2 Dust deposition to high-elevation DML from the last glacial period to the Holocene-present day

The new evidence from this study over the satellite period and last millennium highlights that certain aspects of the regional dust cycle to the high-elevation DML region have remained unchanged since the last glacial period. Firstly, as discussed, there is overwhelming evidence that SSA is the dominant PSA for the high-elevation DML region over the last glacial period through to the Holocene (Wegner et al., 2012; Delmonte et al., 2019; Krätschmer et al., 2022; Gili et al., 2017; Bory et al., 2010), and this remains the same even during the satellite era (Fig. 4.11 & 4.15). Second, the seasonality of dust deposition also has not changed significantly given the common winter-spring maximum in dust deposition observed over the last millennium in the ISOL-ICE core (Fig 4.8) and during the Holocene in the EDML core (Wegner et al., 2015). Third, the dust transport pathways and overall dust fetch area for the DML region between the last glacial period (Krätschmer et al., 2022) and the satellite era (Fig. 4.11 & 4.17) are still largely the same.

In contrast, dust flux and PSD in DML have changed significantly between the last glacial period, Holocene, and present-day. The dust particle flux observed in the EDML core decreased from ~ 5 x 10^5 cm^2 yr^{-1} during the last glacial period (~20,000 years BP) to a Holocene mean of 2 x 10^4 cm^2 yr^{-1} , while the particle size mode increased from ~2.0 to 2.2 μm from the last glacial period to the Holocene (Wegner et al., 2015). Comparatively, the dust flux and PSD in the ISOL-ICE core are observed to covary over the last millennium, with larger (smaller) particles associated with increased (decreased) dust flux (Fig. 4.4b & c). Based on what has remained the same in the regional dust cycle to the high-elevation DML region, the difference in dust flux and PSD patterns in the EDML versus ISOL-ICE core can possibly be explained by either changes in source conditions, such as aridity and soil sediment availability, or the strength of dust transport (e.g., same transport pathways but with stronger wind speeds or less wash-out from precipitation).

5.2.3 Abrupt increase in dust deposition over the last century

As a striking feature of the ISOL-ICE dust record over the past century is the abrupt increase in dust parameters in the early-1900s (Fig. 4.5), this section provides possible explanations behind this sudden shift based on the literature and results from this study. Importantly, the insensitivity of dust transport pathways to particle size and seasonality (Fig. 4.11 & 4.17) suggests that changes to the dust transport pathways related to these two factors are likely not important drivers of the abrupt shift and are therefore excluded as possible reasons. Similarly, changes to seasonality of dust deposition at the ISOL-ICE site and the dominant PSA are ruled out as potential drivers

of the abrupt increase since these have also not changed significantly since the Holocene or last glacial period as discussed in section 5.2.2. In addition, the snow accumulation rate does not exhibit a similar abrupt increase in the early-1900s, indicating that the accumulation rate was not a driver of the increase (Fig. 4.5d). After ruling out these potential drivers, this section therefore explores changes at the dust source regions or climate variability as possible explanations for the abrupt increase in dust deposition.

The similar timing of the abrupt increase and the development of the SSA dust bowls in the early-1900s suggest a connection between the two. Higher wind speeds and drier conditions over SSA associated with the dust bowls provide more favourable conditions for dust transport from SSA to the ISOL-ICE site (Viglizzo & Frank, 2006). However, while a drier climate likely contributed to increased dust activity during this period, the detected new mean level in dust parameters after the early-1900s increase (Fig 4.5) is indicative of a sustained change in dust source conditions and/or transport patterns that can be better explained by permanent land use change in SSA rather than an abrupt and prolonged shift in climate patterns; there is no known climate/circulation pattern that exhibits the same abrupt and sustained change from the 1930s onwards. Although this hypothesis involving land use change in SSA is reasonable, the early-1900s increase in concentrations is not clearly observed in other SSA-sourced ice cores, especially the nearby IND-25/B5 core (Fig. 5.1). It is therefore questionable whether the abrupt increase in the ISOL-ICE core is due to changes to source conditions, especially land-use change associated with the dust bowls.

Another possible explanation for the sudden shift in dust deposition is increased contribution from local Antarctic dust sources, such as from nearby mountain ranges in coastal DML. This is supported by the abrupt increase in CPP at the ISOL-ICE site in the early-1900s (Fig. 4.5b), indicating larger particles being deposited at the site, and the presence of large coarse particles during the same period (Fig. 4.7). However, it remains difficult to further support this hypothesis given the lack of geochemical fingerprinting data from the ISOL-ICE site over this time period (Delmonte et al., 2019).

From an atmospheric dynamics perspective, the abrupt increase could also reflect a period of enhanced cyclonic activity south of SSA possibly related to the PDO. Based on the correlation analysis, summer-autumn PDO appears to be an important large-scale climate pattern associated with multi-decadal dust CPP variability at the ISOL-ICE site over the past century (Fig. 4.26). Despite a weak interannual correlation (R=0.2), the multi-decadal variability of the summer-autumn PDO closely matches that of dust CPP at the ISOL-ICE site. This is consistent with previous studies showing PDO variability influences cyclonic activity over Drake Passage (Clem et al. 2019, 2020; Turner et al. 2016). Importantly, inter-annual variability in dust deposition at the ISOL-ICE site does not appear related to ENSO or SAM, contrary to what studies in other SSA-sourced ice core sites suggest (e.g., Koffman et al., 2014; Laluraj et al., 2020). However, since the correlation analysis in this study is mainly done for the satellite era, interpretations of the dust record before 1979 are based on the assumption that the relationships between circulation and dust deposition variability at the ISOL-ICE site hold over the last century. However, Marshall (2007) and Turner et al. (2019a) show that the large-scale atmospheric circulation patterns that drive wind and temperature variability across coastal East Antarctica and DML are not stationary

in time. Therefore, there are limitations in this assumption that the large-scale forcing of the Drake Passage cyclone during 1979-2017 holds true throughout the entire 20th century or before. Further research is required to determine whether the circulation patterns driving dust deposition at the ISOL-ICE site over the satellite era are the same for the rest of the 20th century, but this study reveals that tropically forced cyclonic activity south of SSA associated with PDO variability is one important mechanism that transports dust from SSA to the ISOL-ICE site. Notably, an enhanced cyclonic circulation during the early-1900s would generally lead to less precipitation over central SSA (Fig. 4.21 & 4.23), consistent with the reported drier conditions during the dust bowl era (Viglizzo & Frank, 2006). This indicates a possible association between the dust bowls and cyclonic activity south of SSA.

5.3 Future work

The dust transport mechanisms established over the satellite era in this work holds much potential for investigating decadal to centennial climate and dust variability in the SH. Several directions for future work are suggested:

1. The robustness of dust transport mechanisms and the sensitivity of dust transport pathways/fetch areas to different conditions over the satellite era can be further strengthened by doing case studies of certain climate epochs/periods within the same period.

2. Further investigating the relationship between dust CPP and the non-ENSO variability of the PDO would be useful to further understand the relationships between cyclonic activity south of SSA and tropically forced Rossby waves.

3. The same correlation analyses between large-scale atmospheric circulation/climate patterns and dust particle size can be done using other ice cores that have high resolution size-resolved dust records over the satellite era. This will allow for a more comprehensive characterisation of dust particle size-climate relationships over Antarctica.

4. The modelled emission sensitivities simulated in Flexpart can be converted to simulated dust contribution by simulating dust emission rates from source regions, thereby not only accounting for dust transport but also source conditions.

5. As this study primarily utilises modelling and reanalysis data, geochemical fingerprinting work focusing on the last century can complement findings in this research, especially in relation to determining the relative dust contribution from local versus sub-Antarctic dust source regions.

6. The use of dust deposition at the ISOL-ICE site as a proxy for past large-scale climate/circulation variability requires comparison with other climate proxy records to support interpretations about past climate, especially over centennial timescales.

7. Frequency analysis of ISOL-ICE record can be done to identify key periodicities in dust deposition that will help determine the drivers of dust variability at the site over different timescales.

6. CONCLUSIONS

The main findings are outlined below answering the specific objectives of this study:

Objective 1: Identify key dust transport pathways to the ISOL-ICE site over the satellite era

1. The main potential source areas for dust deposited at the ISOL-ICE site include SSA, primarily south of 45°S, and mountain ranges with exposed rock surfaces north of the ISOL-ICE site. The observed particle size mode in ISOL-ICE core is 3.7 μm, which likely represents long-range transported dust from the eastern coast of SSA between 47-50°S as simulated by backward dust dispersion modelling. Both dust back trajectories and emission sensitivity point to SSA as the dominant PSA for the ISOL-ICE site. Furthermore, the strongest dust particle size and atmospheric circulation correlations are close to SSA, indicating long-range transport from SSA to the ISOL-ICE site. However, the high dust CPP values and the presence of large coarse particles (10-50 μm) over the satellite era also indicate non-negligible transport from nearby Antarctic dust sources.

2. Dust particles from SSA are uplifted to at least ~1500 m.a.s.l. in the SSA region and are advected east to south-eastward to the ISOL-ICE site following a cyclonic circulation south of SSA. Comparatively, dust from nearby exposed rock surfaces follow the prevailing polar easterly flow to the ice core site.

3. While dust transport pathways to the ISOL-ICE site do not show a clear systematic pattern across seasons and particle sizes, the amount of dust transported to the ISOL-ICE site is higher for smaller particles compared to larger particles and is most pronounced during winter/spring. This winter/spring maximum in dust transport possibly reflects optimal source conditions for dust generation during these seasons associated with a broad and deep ASL.

Objective 2: Determine the regional climatic controls of PSD at the ISOL-ICE site over the satellite era

4. The primary circulation pattern associated with dust deposition at the ISOL-ICE site is a cyclonic system south of SSA. This cyclonic activity most consistently manifests as a low-pressure system over the Drake Passage that is pronounced during summer-autumn. During winter-spring, deepening of the ASL centred just west of the Antarctic Peninsula enables stronger dust transport from SSA to the ISOL-ICE ice core site compared to the cyclonic circulation over Drake Passage in summer-autumn, though the ASL pattern is primarily constrained to winter-spring.

5. The cyclonic circulation patterns south of SSA are part of tropically forced Rossby wave patterns. On seasonal timescales, cyclonic circulation in this region is tied to variations in convective activity in the SPCZ, with summer-autumn associated with increased convection in the SPCZ and winter-spring related to suppressed convection in the SPCZ perturbing the subtropical jet. On

an annual basis, the described seasonal patterns likely cancel out, and instead, the Rossby wave source is located in central tropical Pacific.

6. Southward Rossby wave propagation appears to be related to multi-decadal PDO variability during summer-autumn. Given the insignificant correlation between dust CPP and SOI, the Rossby wave patterns are likely related to the non-ENSO variability of the PDO, explaining the SPCZ-induced Rossby wave source. Importantly, no significant correlation is also found with SAM and ENSO and therefore do not appear to be important drivers of dust transport from SSA to the ISOL-ICE site.

Objective 3: Contextualise the recent increase in dust deposition at the ISOL-ICE site over the last millennium.

7. Dust deposition recorded in the ISOL-ICE core shows an abrupt transition to a higher mean dust flux of 0.30 mg m^{-2} yr^{-1} in the early-1900s onwards compared to the pre-1900 average of 0.03 mg m^{-2} yr^{-1}. Similarly, dust CPP increased from a pre-1900 mean of 71 % to 83 % from the early-1900s onwards. The shift translates to a 10x increase in dust mass concentrations and flux, and a ~12 % increase in the proportion of larger particles being deposited at the site. Intercomparison with other ice cores indicates that the early-1900s abrupt increase in the ISOL-ICE dust record represents a high-elevation regional scale rather than Antarctic-wide signal. This study suggests that the abrupt increase is possibly due to either land use change related to the 1930s-1950s dust bowls, local dust contribution from exposed rock surfaces from the mountain

ranges in the coastal DML region, enhanced cyclonic activity south of SSA related to the SPCZ and PDO, or a combination thereof.

8. An overall positive trend in dust mass concentrations is observed over the last century for the ISOL-ICE, WAIS, IND-25/B5, and JRI cores. However, shorter-scale variability is largely different for each core, possibly reflecting differences in combinations of PSAs and regional transport patterns.

9. Comparing the last glacial period, the Holocene, and present-day, certain aspects of the regional dust cycle to the high-elevation DML region have remained unchanged. Firstly, the dominant dust source for high-elevation DML is still SSA. Second, the winter/spring maximum in dust deposition has not changed significantly since the Holocene. Lastly, the dust transport pathways and overall dust fetch area for the DML region between the last glacial period and the satellite era are largely the same.

From where and how is dust transported to high-elevation DML, Antarctica over the satellite era? The results of this study show that dust is transported from SSA to the ISOL-ICE site through cyclonic circulation south of SSA. Multi-decadal PDO variability during summer-autumn relates to the Rossby wave propagation that deepens or forms this cyclonic circulation. Importantly, this circulation pattern provides a foundation for future work to investigate the drivers of dust variability in the high-elevation DML region over the past millennium.

7. REFERENCES

Abram, N. J., Mulvaney, R., Vimeux, F., Phipps, S. J., Turner, J., & England, M. H. (2014). Evolution of the Southern Annular Mode during the past millennium. *Nature Climate Change*, *4*(7), 564–569. https://doi.org/10.1038/nclimate2235

Ackerman, S. A., & Chung, H. (1992). Radiative Effects of Airborne Dust on Regional Energy Budgets at the Top of the Atmosphere. *Journal of Applied Meteorology and Climatology*, *31*(2), 223–233. https://doi.org/10.1175/1520-0450(1992)031<0223:REOADO>2.0.CO;2

Arblaster, J. M., Meehl, G. A., & Karoly, D. J. (2011). Future climate change in the Southern Hemisphere: Competing effects of ozone and greenhouse gases. *Geophysical Research Letters*, *38*(2). https://doi.org/10.1029/2010GL045384

Bagnold, R. A. (1941). *The Physics of Blown Sand and Desert Dunes*. Chapman and Hall, London.

Barbante, C., Bellomi, T., Mezzadri, G., Cescon, P., Scarponi, G., Morel, C., Jay, S., Van De Velde, K., Ferrari, C., & Boutron, C. F. (1997). Direct Determination of Heavy Metals at Picogram per Gram Levels in Greenland and Antarctic Snow by Double Focusing Inductively Coupled Plasma Mass Spectrometry. *Journal of Analytical Atomic Spectrometry*, *12*(9), 925–931. https://doi.org/10.1039/a701686g

Basile, I., Grousset, F. E., Revel, M., Petit, J. R., Biscaye, P. E., & Barkov, N. I. (1997). Patagonian origin of glacial dust deposited in East Antarctica (Vostok and Dome C) during glacial stages 2, 4 and 6. *Earth and Planetary Science Letters*, *146*(3), 573–589. https://doi.org/10.1016/S0012-821X(96)00255-5

Bergametti, G., & Forêt, G. (2014). Dust Deposition. In P. Knippertz & J.-B. W. Stuut (Eds.), *Mineral Dust: A Key Player in the Earth System* (pp. 179–200). Springer Netherlands. https://doi.org/10.1007/978-94-017-8978-3_8

Bernardos, J. N., Viglizzo, E. F., Jouvet, V., Lértora, F. A., Pordomingo, A. J., & Cid, F. D. (2001). The use of EPIC model to study the agroecological change during 93 years of farming transformation in the Argentine pampas. *Agricultural Systems*, *69*(3), 215–234. https://doi.org/10.1016/S0308-521X(01)00027-0

Bory, A., Wolff, E., Mulvaney, R., Jagoutz, E., Wegner, A., Ruth, U., & Elderfield, H. (2010). Multiple sources supply eolian mineral dust to the Atlantic sector of coastal Antarctica: Evidence from recent snow layers at the top of Berkner Island ice sheet. *Earth and Planetary Science Letters*, *291*(1), 138–148. https://doi.org/10.1016/j.epsl.2010.01.006

Bowman, K. P., Lin, J. C., Stohl, A., Draxler, R., Konopka, P., Andrews, A., & Brunner, D. (2013). Input Data Requirements for Lagrangian Trajectory Models. *Bulletin of the American Meteorological Society*, *94*(7), 1051–1058. https://doi.org/10.1175/BAMS-D-12-00076.1

Bracegirdle, T. J., Holmes, C. R., Hosking, J. S., Marshall, G. J., Osman, M., Patterson, M., & Rackow, T. (2020). Improvements in Circumpolar Southern Hemisphere Extratropical Atmospheric Circulation in CMIP6 Compared to CMIP5. *Earth and Space Science*, *7*(6), e2019EA001065. https://doi.org/10.1029/2019EA001065

Bracegirdle, T. J., & Marshall, G. J. (2012). The Reliability of Antarctic Tropospheric Pressure and Temperature in the Latest Global Reanalyses. *Journal of Climate*, *25*(20), 7138–7146. https://doi.org/10.1175/JCLI-D-11-00685.1

Broeke, M. R. V. D., & Lipzig, N. P. M. V. (2003a). Response of Wintertime Antarctic Temperatures to the Antarctic Oscillation: Results of a Regional Climate Model. In *Antarctic Peninsula Climate Variability: Historical and Paleoenvironmental Perspectives* (pp. 43–58). American Geophysical Union (AGU). https://doi.org/10.1029/AR079p0043

Broeke, M. R. van den, & Lipzig, N. P. M. van. (2003b). Factors Controlling the Near-Surface Wind Field in Antarctica. *Monthly Weather Review*, *131*(4), 733–743. https://doi.org/10.1175/1520-0493(2003)131<0733:FCTNSW>2.0.CO;2

Bromwich, D. H., & Fogt, R. L. (2004). Strong Trends in the Skill of the ERA-40 and NCEP–NCAR Reanalyses in the High and Midlatitudes of the Southern Hemisphere, 1958–2001. *Journal of Climate*, *17*(23), 4603–4619. https://doi.org/10.1175/3241.1

Brown, J. R., Lengaigne, M., Lintner, B. R., Widlansky, M. J., van der Wiel, K., Dutheil, C., Linsley, B. K., Matthews, A. J., & Renwick, J. (2020). South Pacific Convergence Zone dynamics, variability and impacts in a changing climate. *Nature Reviews Earth & Environment*, *1*(10), 530–543. https://doi.org/10.1038/s43017-020-0078-2

Bullard, J. E., Baddock, M., Bradwell, T., Crusius, J., Darlington, E., Gaiero, D., Gassó, S., Gisladottir, G., Hodgkins, R., McCulloch, R., McKenna-Neuman, C., Mockford, T., Stewart, H., & Thorsteinsson, T. (2016). High-latitude dust in the Earth system. *Reviews of Geophysics*, *54*(2), 447–485. https://doi.org/10.1002/2016RG000518

Butterworth, S. (1930). On the Theory of Filter Amplifiers. *Experimental Wireless and the Wireless Engineer*, Vol. 7, pp. 536-541.

Clem, K. R., & Fogt, R. L. (2015). South Pacific circulation changes and their connection to the tropics and regional Antarctic warming in austral spring, 1979–2012. *Journal of Geophysical Research: Atmospheres*, *120*(7), 2773–2792. https://doi.org/10.1002/2014JD022940

Clem, K. R., Fogt, R. L., Turner, J., Lintner, B. R., Marshall, G. J., Miller, J. R., & Renwick, J. A. (2020). Record warming at the South Pole during the past three decades. *Nature Climate Change*, *10*(8), 762–770. https://doi.org/10.1038/s41558-020-0815-z

Clem, K. R., Lintner, B. R., Broccoli, A. J., & Miller, J. R. (2019). Role of the South Pacific Convergence Zone in West Antarctic Decadal Climate Variability. *Geophysical Research Letters*, *46*(12), 6900–6909. https://doi.org/10.1029/2019GL082108

Cole-Dai, J., & Mosley-Thompson, E. (1999). The Pinatubo eruption in South Pole snow and its potential value to ice-core paleovolcanic records. *Annals of Glaciology*, *29*, 99–105. https://doi.org/10.3189/172756499781821319

Collins, M., An, S.-I., Cai, W., Ganachaud, A., Guilyardi, E., Jin, F.-F., Jochum, M., Lengaigne, M., Power, S., Timmermann, A., Vecchi, G., & Wittenberg, A. (2010). The impact of global warming on the tropical Pacific Ocean and El Niño. *Nature Geoscience*, *3*(6), 391–397. https://doi.org/10.1038/ngeo868

Crowley, T. J., & Lowery, T. S. (2000). How Warm Was the Medieval Warm Period? *AMBIO: A Journal of the Human Environment*, *29*(1), 51–54. https://doi.org/10.1579/0044-7447-29.1.51

Cruz, M. T., Bañaga, P. A., Betito, G., Braun, R. A., Stahl, C., Aghdam, M. A., Cambaliza, M. O., Dadashazar, H., Hilario, M. R., Lorenzo, G. R., Ma, L., MacDonald, A. B., Pabroa, P. C., Yee, J. R., Simpas, J. B., & Sorooshian, A.

(2019). Size-resolved composition and morphology of particulate matter during the southwest monsoon in Metro Manila, Philippines. *Atmospheric Chemistry and Physics*, *19*(16), 10675–10696. https://doi.org/10.5194/acp-19-10675-2019

Dee, D. P., Uppala, S. M., Simmons, A. J., Berrisford, P., Poli, P., Kobayashi, S., Andrae, U., Balmaseda, M. A., Balsamo, G., Bauer, P., Bechtold, P., Beljaars, A. C. M., van de Berg, L., Bidlot, J., Bormann, N., Delsol, C., Dragani, R., Fuentes, M., Geer, A. J., … Vitart, F. (2011). The ERA-Interim reanalysis: Configuration and performance of the data assimilation system. *Quarterly Journal of the Royal Meteorological Society*, *137*(656), 553–597. https://doi.org/10.1002/qj.828

Delmonte, B., Petit, .J. & Maggi, .V. Glacial to Holocene implications of the new 27000-year dust record from the EPICA Dome C (East Antarctica) ice core. *Climate Dynamics* **18,** 647–660 (2002). https://doi.org/10.1007/s00382-001-0193-9

Delmonte, B., Basile-Doelsch, I., Petit, J.-R., Maggi, V., Revel-Rolland, M., Michard, A., Jagoutz, E., & Grousset, F. (2004). Comparing the Epica and Vostok dust records during the last 220,000 years: Stratigraphical correlation and provenance in glacial periods. *Earth-Science Reviews*, *66*(1), 63–87. https://doi.org/10.1016/j.earscirev.2003.10.004

Delmonte, B., Paleari, C. I., Andò, S., Garzanti, E., Andersson, P. S., Petit, J. R., Crosta, X., Narcisi, B., Baroni, C., Salvatore, M. C., Baccolo, G., & Maggi, V. (2017). Causes of dust size variability in central East Antarctica (Dome B): Atmospheric transport from expanded South American sources during Marine

Isotope Stage 2. *Quaternary Science Reviews*, *168*, 55–68. https://doi.org/10.1016/j.quascirev.2017.05.009

Delmonte, B., Winton, H., Baroni, M., Baccolo, G., Hansson, M., Andersson, P., Baroni, C., Salvatore, M. C., Lanci, L., & Maggi, V. (2019). Holocene dust in East Antarctica: Provenance and variability in time and space. *The Holocene*, *30*(4), 546–558. https://doi.org/10.1177/0959683619875188

Ding, Q., Steig, E. J., Battisti, D. S., & Wallace, J. M. (2012). Influence of the Tropics on the Southern Annular Mode. *Journal of Climate*, *25*(18), 6330–6348. https://doi.org/10.1175/JCLI-D-11-00523.1

Draxler, R.R., and G.D. Hess, (1998): An overview of the HYSPLIT_4 modeling system of trajectories, dispersion, and deposition. Aust. Meteor. Mag., 47, 295-308.

Eckhardt, S., Cassiani, M., Evangeliou, N., Sollum, E., Pisso, I., & Stohl, A. (2017). Source–receptor matrix calculation for deposited mass with the Lagrangian particle dispersion model FLEXPART v10.2 in backward mode. *Geoscientific Model Development*, *10*(12), 4605–4618. https://doi.org/10.5194/gmd-10-4605-2017

Engeln, A. von, & Teixeira, J. (2013). A Planetary Boundary Layer Height Climatology Derived from ECMWF Reanalysis Data. *Journal of Climate*, *26*(17), 6575–6590. https://doi.org/10.1175/JCLI-D-12-00385.1

Fogt, R. L., Bromwich, D. H., & Hines, K. M. (2011). Understanding the SAM influence on the South Pacific ENSO teleconnection. *Climate Dynamics*, *36*(7), 1555–1576. https://doi.org/10.1007/s00382-010-0905-0

Fogt, R. L., & Marshall, G. J. (2020). The Southern Annular Mode: Variability, trends, and climate impacts across the Southern Hemisphere. *WIREs Climate Change*, *11*(4), e652. https://doi.org/10.1002/wcc.652

Gallego, D., Ribera, P., Garcia-Herrera, R., Hernandez, E., & Gimeno, L. (2005). A new look for the Southern Hemisphere jet stream. *Climate Dynamics*, *24*(6), 607–621. https://doi.org/10.1007/s00382-005-0006-7

Gassó, S., Stein, A., Marino, F., Castellano, E., Udisti, R., & Ceratto, J. (2010). A combined observational and modeling approach to study modern dust transport from the Patagonia desert to East Antarctica. *Atmospheric Chemistry and Physics*, *10*(17), 8287–8303. https://doi.org/10.5194/acp-10-8287-2010

Gassó, S., & Torres, O. (2019). Temporal Characterization of Dust Activity in the Central Patagonia Desert (Years 1964–2017). *Journal of Geophysical Research: Atmospheres*, *124*(6), 3417–3434. https://doi.org/10.1029/2018JD030209

Gherboudj, I., Naseema Beegum, S., & Ghedira, H. (2017). Identifying natural dust source regions over the Middle-East and North-Africa: Estimation of dust emission potential. *Earth-Science Reviews*, *165*, 342–355. https://doi.org/10.1016/j.earscirev.2016.12.010

Gili, S., Gaiero, D. M., Goldstein, S. L., Chemale, F., Jweda, J., Kaplan, M. R., Becchio, R. A., & Koester, E. (2017). Glacial/interglacial changes of Southern Hemisphere wind circulation from the geochemistry of South American dust. *Earth and Planetary Science Letters*, *469*, 98–109. https://doi.org/10.1016/j.epsl.2017.04.007

Gili, S., Gaiero, D. M., Goldstein, S. L., Chemale Jr, F., Koester, E., Jweda, J., Vallelonga, P., & Kaplan, M. R. (2016). Provenance of dust to Antarctica: A lead isotopic perspective. *Geophysical Research Letters*, *43*(5), 2291–2298. https://doi.org/10.1002/2016GL068244

Gillett, N. P., & Thompson, D. W. J. (2003). Simulation of Recent Southern Hemisphere Climate Change. *Science*. https://doi.org/10.1126/science.1087440

Gillett, Z. E., Hendon, H. H., Arblaster, J. M., & Lim, E.-P. (2021). Tropical and Extratropical Influences on the Variability of the Southern Hemisphere Wintertime Subtropical Jet. *Journal of Climate*, *34*(10), 4009–4022. https://doi.org/10.1175/JCLI-D-20-0460.1

Ginoux, P., Prospero, J. M., Gill, T. E., Hsu, N. C., & Zhao, M. (2012). Global-scale attribution of anthropogenic and natural dust sources and their emission rates based on MODIS Deep Blue aerosol products. *Reviews of Geophysics*, *50*(3). https://doi.org/10.1029/2012RG000388

Göktas, F., Fischer, H., Oerter, H., Weller, R., Sommer, S., & Miller, H. (2002). A glacio-chemical characterization of the new EPICA deep-drilling site on Amundsenisen, Dronning Maud Land, Antarctica. *Annals of Glaciology*, *35*, 347–354. https://doi.org/10.3189/172756402781816474

Gong, D., & Wang, S. (1999). Definition of Antarctic Oscillation index. *Geophysical Research Letters*, *26*(4), 459–462. https://doi.org/10.1029/1999GL900003

Grieman, M. M., Hoffmann, H. M., Humby, J. D., Mulvaney, R., Nehrbass-Ahles, C., Rix, J., Thomas, E. R., Tuckwell, R., & Wolff, E. W. (2022). Continuous flow analysis methods for sodium, magnesium and calcium detection in the

Skytrain ice core. *Journal of Glaciology*, *68*(267), 90–100. https://doi.org/10.1017/jog.2021.75

Grousset, F. E., Biscaye, P. E., Revel, M., Petit, J.-R., Pye, K., Joussaume, S., & Jouzel, J. (1992). Antarctic (Dome C) ice-core dust at 18 k.y. B.P.: Isotopic constraints on origins. *Earth and Planetary Science Letters*, *111*(1), 175–182. https://doi.org/10.1016/0012-821X(92)90177-W

Grove, J. M. (2004). *The Little Ice Age* (2nd edition). Routledge.

Grove, J. M., & Switsur, R. (1994). Glacial geological evidence for the medieval warm period. *Climatic Change*, *26*(2), 143–169. https://doi.org/10.1007/BF01092411

Grythe, H., Kristiansen, N. I., Groot Zwaaftink, C. D., Eckhardt, S., Ström, J., Tunved, P., Krejci, R., & Stohl, A. (2017). A new aerosol wet removal scheme for the Lagrangian particle model FLEXPART v10. *Geoscientific Model Development*, *10*(4), 1447–1466. https://doi.org/10.5194/gmd-10-1447-2017

Gupta, A. S., & England, M. H. (2006). Coupled Ocean–Atmosphere–Ice Response to Variations in the Southern Annular Mode. *Journal of Climate*, *19*(18), 4457–4486. https://doi.org/10.1175/JCLI3843.1

Hartmann, D. L. (2016). *Global Physical Climatology* (2nd edition). Elsevier Science.

He, P., Bian, L., Zheng, X., Yu, J., Sun, C., Ye, P., & Xie, Z. (2016). Observation of surface ozone in the marine boundary layer along a cruise through the Arctic Ocean: From offshore to remote. *Atmospheric Research*, *169*, 191–198. https://doi.org/10.1016/j.atmosres.2015.10.009

Henley, B. J. (2017). Pacific decadal climate variability: Indices, patterns and tropical-extratropical interactions. *Global and Planetary Change*, *155*, 42–55. https://doi.org/10.1016/j.gloplacha.2017.06.004

Henley, B. J., Gergis, J., Karoly, D. J., Power, S., Kennedy, J., & Folland, C. K. (2015). A Tripole Index for the Interdecadal Pacific Oscillation. *Climate Dynamics*, *45*(11–12), 3077–3090. https://doi.org/10.1007/s00382-015-2525-1

Hersbach, H., Bell, B., Berrisford, P., Hirahara, S., Horányi, A., Muñoz-Sabater, J., Nicolas, J., Peubey, C., Radu, R., Schepers, D., Simmons, A., Soci, C., Abdalla, S., Abellan, X., Balsamo, G., Bechtold, P., Biavati, G., Bidlot, J., Bonavita, M., … Thépaut, J.-N. (2020). The ERA5 global reanalysis. *Quarterly Journal of the Royal Meteorological Society*, *146*(730), 1999–2049. https://doi.org/10.1002/qj.3803

Hofstede, C. M., Roderik, S. W. van de W., Kaspers, K. A., Broeke, M. R. van den, Karlöf, L., Winther, J.-G., Isaksson, E., Lappegard, G., Mulvaney, R., Oerter, H., & Wilhelms, F. (2004). Firn accumulation records for the past 1000 years on the basis of dielectric profiling of six cores from Dronning Maud Land, Antarctica. *Journal of Glaciology*, *50*(169), 279–291. https://doi.org/10.3189/172756504781830169

Hooper, J., & Marx, S. (2018). A global doubling of dust emissions during the Anthropocene? *Global and Planetary Change*, *169*, 70–91. https://doi.org/10.1016/j.gloplacha.2018.07.003

Huang, B., Thorne, P. W., Banzon, V. F., Boyer, T., Chepurin, G., Lawrimore, J. H., Menne, M. J., Smith, T. M., Vose, R. S., & Zhang, H.-M. (2017). Extended Reconstructed Sea Surface Temperature, Version 5 (ERSSTv5): Upgrades, Validations, and Intercomparisons. *Journal of Climate*, *30*(20), 8179–8205. https://doi.org/10.1175/JCLI-D-16-0836.1

Irving, D., & Simmonds, I. (2016). A New Method for Identifying the Pacific–South American Pattern and Its Influence on Regional Climate Variability. *Journal of Climate*, *29*(17), 6109–6125. https://doi.org/10.1175/JCLI-D-15-0843.1

Jones, A., Thomson, D., Hort, M., & Devenish, B. (2007). The U.K. Met Office's Next-Generation Atmospheric Dispersion Model, NAME III. In C. Borrego & A.-L. Norman (Eds.), *Air Pollution Modeling and Its Application XVII* (pp. 580–589). Springer US. https://doi.org/10.1007/978-0-387-68854-1_62

Killick, R., Fearnhead, P., & Eckley, I. A. (2012). Optimal Detection of Changepoints With a Linear Computational Cost. *Journal of the American Statistical Association*, *107*(500), 1590–1598. https://doi.org/10.1080/01621459.2012.737745

Knippertz, P. (2014). Meteorological Aspects of Dust Storms. In P. Knippertz & J.-B. W. Stuut (Eds.), *Mineral Dust: A Key Player in the Earth System* (pp. 121–147). Springer Netherlands. https://doi.org/10.1007/978-94-017-8978-3_6

Koffman, B. G., Goldstein, S. L., Winckler, G., Borunda, A., Kaplan, M. R., Bolge, L., Cai, Y., Recasens, C., Koffman, T. N. B., & Vallelonga, P. (2021). New Zealand as a source of mineral dust to the atmosphere and ocean. *Quaternary Science Reviews*, *251*, 106659. https://doi.org/10.1016/j.quascirev.2020.106659

Koffman, B. G., & Kreutz, K. J. (2014). Evidence that local dust sources supply low-elevation Antarctic regions. *Past Global Changes Magazine*, *22*(2), 76–77. https://doi.org/10.22498/pages.22.2.76

Koffman, B. G., Kreutz, K. J., Breton, D. J., Kane, E. J., Winski, D. A., Birkel, S. D., Kurbatov, A. V., & Handley, M. J. (2014). Centennial-scale variability of the Southern Hemisphere westerly wind belt in the eastern Pacific over the past

two millennia. *Climate of the Past*, *10*(3), 1125–1144. https://doi.org/10.5194/cp-10-1125-2014

Kok, J. F. (2011). Does the size distribution of mineral dust aerosols depend on the wind speed at emission? *Atmospheric Chemistry and Physics*, *11*(19), 10149–10156. https://doi.org/10.5194/acp-11-10149-2011

Kok, J. F., Parteli, E. J. R., Michaels, T. I., & Karam, D. B. (2012). The physics of wind-blown sand and dust. *Reports on Progress in Physics*, *75*(10), 106901. https://doi.org/10.1088/0034-4885/75/10/106901

Laluraj, C. M., Krishnan, K. P., Thamban, M., Mohan, R., Naik, S. S., D'Souza, W., Ravindra, R., & Chaturvedi, A. (2009). Origin and characterisation of microparticles in an ice core from the Central Dronning Maud Land, East Antarctica. *Environmental Monitoring and Assessment*, *149*(1), 377–383. https://doi.org/10.1007/s10661-008-0212-y

Laluraj, C. M., Rahaman, W., Thamban, M., & Srivastava, R. (2020). Enhanced Dust Influx to South Atlantic Sector of Antarctica During the Late-20th Century: Causes and Contribution to Radiative Forcing. *Journal of Geophysical Research: Atmospheres*, *125*(8), e2019JD030675. https://doi.org/10.1029/2019JD030675

Laluraj, C. M., Thamban, M., & Satheesan, K. (2014). Dust and associated geochemical fluxes in a firn core from coastal East Antarctica and its linkages with Southern Hemisphere climate variability over the last 50 years. *Atmospheric Environment*, *90*, 23–32. https://doi.org/10.1016/j.atmosenv.2014.03.031

Lamb, H. H. (1965). The early medieval warm epoch and its sequel. *Palaeogeography, Palaeoclimatology, Palaeoecology*, *1*, 13–37. https://doi.org/10.1016/0031-0182(65)90004-0

Lambert, F., Bigler, M., Steffensen, J. P., Hutterli, M., & Fischer, H. (2012). Centennial mineral dust variability in high-resolution ice core data from Dome C, Antarctica. *Climate of the Past*, *8*(2), 609–623. https://doi.org/10.5194/cp-8-609-2012

Lambert, F., Delmonte, B., Petit, J. R., Bigler, M., Kaufmann, P. R., Hutterli, M. A., Stocker, T. F., Ruth, U., Steffensen, J. P., & Maggi, V. (2008). Dust-climate couplings over the past 800,000 years from the EPICA Dome C ice core. *Nature*, *452*(7187), 616–619. https://doi.org/10.1038/nature06763

Lambert, F., Tagliabue, A., Shaffer, G., Lamy, F., Winckler, G., Farias, L., Gallardo, L., & De Pol-Holz, R. (2015). Dust fluxes and iron fertilization in Holocene and Last Glacial Maximum climates. *Geophysical Research Letters*, *42*(14), 6014–6023. https://doi.org/10.1002/2015GL064250

Lamy, F., Gersonde, R., Winckler, G., Esper, O., Jaeschke, A., Kuhn, G., Ullermann, J., Martinez-Garcia, A., Lambert, F., & Kilian, R. (2014). Increased Dust Deposition in the Pacific Southern Ocean During Glacial Periods. *Science*. https://doi.org/10.1126/science.1245424

Langway Jr., C. C., Osada, K., Clausen, H. B., Hammer, C. U., & Shoji, H. (1995). A 10-century comparison of prominent bipolar volcanic events in ice cores. *Journal of Geophysical Research: Atmospheres*, *100*(D8), 16241–16247. https://doi.org/10.1029/95JD01175

Lavielle, M. (2005). Using penalized contrasts for the change-point problem. *Signal Processing*, *85*(8), 1501–1510. https://doi.org/10.1016/j.sigpro.2005.01.012

Lawrence, C. R., Painter, T. H., Landry, C. C., & Neff, J. C. (2010). Contemporary geochemical composition and flux of aeolian dust to the San Juan Mountains, Colorado, United States. *Journal of Geophysical Research: Biogeosciences*, *115*(G3). https://doi.org/10.1029/2009JG001077

L'Heureux, M. L., & Thompson, D. W. J. (2006). Observed Relationships between the El Niño–Southern Oscillation and the Extratropical Zonal-Mean Circulation. *Journal of Climate*, *19*(2), 276–287. https://doi.org/10.1175/JCLI3617.1

Li, F., Ginoux, P., & Ramaswamy, V. (2010). Transport of Patagonian dust to Antarctica. *Journal of Geophysical Research: Atmospheres*, *115*(D18). https://doi.org/10.1029/2009JD012356

Li, X., Cai, W., Meehl, G. A., Chen, D., Yuan, X., Raphael, M., Holland, D. M., Ding, Q., Fogt, R. L., Markle, B. R., Wang, G., Bromwich, D. H., Turner, J., Xie, S.-P., Steig, E. J., Gille, S. T., Xiao, C., Wu, B., Lazzara, M. A., … Song, C. (2021). Tropical teleconnection impacts on Antarctic climate changes. *Nature Reviews Earth & Environment*, *2*(10), 680–698. https://doi.org/10.1038/s43017-021-00204-5

Liebmann, B., & Smith, C. A. (1996). Description of a Complete (Interpolated) Outgoing Longwave Radiation Dataset. *Bulletin of the American Meteorological Society*, *77*(6), 1275–1277.

Lin, J. C., Gerbig, C., Wofsy, S. C., Andrews, A. E., Daube, B. C., Davis, K. J., & Grainger, C. A. (2003). A near-field tool for simulating the upstream influence of atmospheric observations: The Stochastic Time-Inverted Lagrangian Transport (STILT) model. *Journal of Geophysical Research: Atmospheres*, *108*(D16). https://doi.org/10.1029/2002JD003161

Lüning, S., Gałka, M., & Vahrenholt, F. (2019). The Medieval Climate Anomaly in Antarctica. *Palaeogeography, Palaeoclimatology, Palaeoecology*, *532*, 109251. https://doi.org/10.1016/j.palaeo.2019.109251

Ma, Y. F., Du, B. Y., Wang, Q., Hu, Q. Q., Bian, Y. S., Wang, M. B., & Jin, S. Y. (2019). Analysis of the atmospheric pollution transport pathways and sources in Shenyang, based on the HYSPLIT model. *IOP Conference Series: Earth and Environmental Science*, *351*(1), 012030. https://doi.org/10.1088/1755-1315/351/1/012030

Mahowald, N., Albani, S., Kok, J. F., Engelstaeder, S., Scanza, R., Ward, D. S., & Flanner, M. G. (2014). The size distribution of desert dust aerosols and its impact on the Earth system. *Aeolian Research*, *15*, 53–71. https://doi.org/10.1016/j.aeolia.2013.09.002

Mann, M. E., Zhang, Z., Rutherford, S., Bradley, R. S., Hughes, M. K., Shindell, D., Ammann, C., Faluvegi, G., & Ni, F. (2009). Global Signatures and Dynamical Origins of the Little Ice Age and Medieval Climate Anomaly. *Science*. https://doi.org/10.1126/science.1177303

Mantua, N. J., Hare, S. R., Zhang, Y., Wallace, J. M., & Francis, R. C. (1997). A Pacific Interdecadal Climate Oscillation with Impacts on Salmon Production*. *Bulletin of the American Meteorological Society*, *78*(6), 1069–1080. https://doi.org/10.1175/1520-0477(1997)078<1069:APICOW>2.0.CO;2

Markle, B. R., Bertler, N. a. N., Sinclair, K. E., & Sneed, S. B. (2012). Synoptic variability in the Ross Sea region, Antarctica, as seen from back-trajectory modeling and ice core analysis. *Journal of Geophysical Research: Atmospheres*, *117*(D2). https://doi.org/10.1029/2011JD016437

Marshall, G. J. (2007). Half-century seasonal relationships between the Southern Annular mode and Antarctic temperatures. *International Journal of Climatology*, *27*(3), 373–383. https://doi.org/10.1002/joc.1407

Marshall, G. J. (2003). Trends in the Southern Annular Mode from Observations and Reanalyses. *Journal of Climate*, *16*(24), 4134–4143. https://doi.org/10.1175/1520-0442(2003)016<4134:TITSAM>2.0.CO;2

Marticorena, B. (2014). Dust Production Mechanisms. In P. Knippertz & J.-B. W. Stuut (Eds.), *Mineral Dust: A Key Player in the Earth System* (pp. 93–120). Springer Netherlands. https://doi.org/10.1007/978-94-017-8978-3_5

Martin, J. H. (1990). Glacial-interglacial CO2 change: The Iron Hypothesis. *Paleoceanography*, *5*(1), 1–13. https://doi.org/10.1029/PA005i001p00001

Marx, S. K., Kamber, B. S., McGowan, H. A., Petherick, L. M., McTainsh, G. H., Stromsoe, N., Hooper, J. N., & May, J.-H. (2018). Palaeo-dust records: A window to understanding past environments. *Global and Planetary Change*, *165*, 13–43. https://doi.org/10.1016/j.gloplacha.2018.03.001

Masson-Delmotte, V., Schulz, M., Abe-Ouchi, A., Beer, J., Ganopolski, A., Gonzalez Rouco, J. F., Jansen, E., Lambeck, K., Luterbacher, J., Naish, T., Osborn, T., Otto-Bliesner, B., Quinn, T., Ramesh, R., Rojas, M., Shao, X., & Timmermann, A. (2013). Information from paleoclimate archives. In T. F. Stocker, D. Qin, G.-K. Plattner, M. M. B. Tignor, S. K. Allen, J. Boschung, A. Nauels, Y. Xia, V. Bex, & P. M. Midgley (Eds.), *Climate change 2013: The physical science basis* (pp. 383–464). Cambridge University Press. https://doi.org/10.1017/CBO9781107415324.013

Matsuoka, K., Skoglund, A., Roth, G., de Pomereu, J., Griffiths, H., Headland, R., Herried, B., Katsumata, K., Le Brocq, A., Licht, K., Morgan, F., Neff, P. D.,

Ritz, C., Scheinert, M., Tamura, T., Van de Putte, A., van den Broeke, M., von Deschwanden, A., Deschamps-Berger, C., … Melvær, Y. (2021). Quantarctica, an integrated mapping environment for Antarctica, the Southern Ocean, and sub-Antarctic islands. *Environmental Modelling & Software*, *140*, 105015. https://doi.org/10.1016/j.envsoft.2021.105015

Matthews, A. J. (2012). A multiscale framework for the origin and variability of the South Pacific Convergence Zone. *Quarterly Journal of the Royal Meteorological Society*, *138*(666), 1165–1178. https://doi.org/10.1002/qj.1870

McConnell, J. R., Aristarain, A. J., Banta, J. R., Edwards, P. R., & Simões, J. C. (2007). 20th-Century doubling in dust archived in an Antarctic Peninsula ice core parallels climate change and desertification in South America. *Proceedings of the National Academy of Sciences*, *104*(14), 5743–5748. https://doi.org/10.1073/pnas.0607657104

McConnell, J. R., Chellman, N. J., Mulvaney, R., Eckhardt, S., Stohl, A., Plunkett, G., Kipfstuhl, S., Freitag, J., Isaksson, E., Gleason, K. E., Brugger, S. O., McWethy, D. B., Abram, N. J., Liu, P., & Aristarain, A. J. (2021). Hemispheric black carbon increase after the 13th-century Māori arrival in New Zealand. *Nature*, *598*(7879), 82–85. https://doi.org/10.1038/s41586-021-03858-9

McConnell, J. R., Wilson, A. I., Stohl, A., Arienzo, M. M., Chellman, N. J., Eckhardt, S., Thompson, E. M., Pollard, A. M., & Steffensen, J. P. (2018). Lead pollution recorded in Greenland ice indicates European emissions tracked plagues, wars, and imperial expansion during antiquity. *Proceedings of the National Academy of Sciences*, *115*(22), 5726–5731. https://doi.org/10.1073/pnas.1721818115

McMahon, T. A., & Denison, P. J. (1979). Empirical atmospheric deposition parameters—A survey. *Atmospheric Environment (1967)*, *13*(5), 571–585. https://doi.org/10.1016/0004-6981(79)90186-0

Mo, K. C., & Higgins, R. W. (1998). The Pacific–South American Modes and Tropical Convection during the Southern Hemisphere Winter. *Monthly Weather Review*, *126*(6), 1581–1596. https://doi.org/10.1175/1520-0493(1998)126<1581:TPSAMA>2.0.CO;2

Neff, P. D., & Bertler, N. A. N. (2015). Trajectory modeling of modern dust transport to the Southern Ocean and Antarctica. *Journal of Geophysical Research: Atmospheres*, *120*(18), 9303–9322. https://doi.org/10.1002/2015JD023304

Newman, M., Alexander, M. A., Ault, T. R., Cobb, K. M., Deser, C., Lorenzo, E. D., Mantua, N. J., Miller, A. J., Minobe, S., Nakamura, H., Schneider, N., Vimont, D. J., Phillips, A. S., Scott, J. D., & Smith, C. A. (2016). The Pacific Decadal Oscillation, Revisited. *Journal of Climate*, *29*(12), 4399–4427. https://doi.org/10.1175/JCLI-D-15-0508.1

Nye, J. F. (1963). Correction Factor for Accumulation Measured by the Thickness of the Annual Layers in an Ice Sheet. *Journal of Glaciology*, *4*(36), 785–788. https://doi.org/10.3189/S0022143000028367

Oerter, H., Drücker, C., Kipfstuhl, S., & Wilhelms, F. (2009). Kohnen station-the drilling camp for the EPICA deep ice core in Dronning Maud Land. *Polarforschung*, *78*(1), 1-23.

Oerter, H., Wilhelms, F., Jung-Rothenhäusler, F., Göktas, F., Miller, H., Graf, W., & Sommer, S. (2000). Accumulation rates in Dronning Maud Land, Antarctica, as revealed by dielectric-profiling measurements of shallow firn cores. *Annals of Glaciology*, *30*, 27–34. https://doi.org/10.3189/172756400781820705

Ottino, J. M. (1989). *The Kinematics of Mixing: Stretching, Chaos, and Transport* (1st edition). Cambridge University Press.

Parish, T. R., & Bromwich, D. H. (2007). Reexamination of the Near-Surface Airflow over the Antarctic Continent and Implications on Atmospheric Circulations at High Southern Latitudes. *Monthly Weather Review*, *135*(5), 1961–1973. https://doi.org/10.1175/MWR3374.1

Petit, J. R., Jouzel, J., Raynaud, D., Barkov, N. I., Barnola, J.-M., Basile, I., Bender, M., Chappellaz, J., Davis, M., Delaygue, G., Delmotte, M., Kotlyakov, V. M., Legrand, M., Lipenkov, V. Y., Lorius, C., PÉpin, L., Ritz, C., Saltzman, E., & Stievenard, M. (1999). Climate and atmospheric history of the past 420,000 years from the Vostok ice core, Antarctica. *Nature*, *399*(6735), 429–436. https://doi.org/10.1038/20859

Pisso, I., Sollum, E., Grythe, H., Kristiansen, N. I., Cassiani, M., Eckhardt, S., Arnold, D., Morton, D., Thompson, R. L., Groot Zwaaftink, C. D., Evangeliou, N., Sodemann, H., Haimberger, L., Henne, S., Brunner, D., Burkhart, J. F., Fouilloux, A., Brioude, J., Philipp, A., … Stohl, A. (2019). The Lagrangian particle dispersion model FLEXPART version 10.4. *Geoscientific Model Development*, *12*(12), 4955–4997. https://doi.org/10.5194/gmd-12-4955-2019

Power, S., Casey, T., Folland, C., Colman, A., & Mehta, V. (1999). Inter-decadal modulation of the impact of ENSO on Australia. *Climate Dynamics*, *15*(5), 319–324. https://doi.org/10.1007/s003820050284

Pye, K. (1987). *Aeolian Dust and Dust Deposits* (First edition). Academic Press.

Pye, K. (1995). The nature, origin and accumulation of loess. *Quaternary Science Reviews*, *14*(7), 653–667. https://doi.org/10.1016/0277-3791(95)00047-X

QGIS.org, 2021. QGIS Geographic Information System. QGIS Association. http://www.qgis.org

Raphael, M. N., Marshall, G. J., Turner, J., Fogt, R. L., Schneider, D., Dixon, D. A., Hosking, J. S., Jones, J. M., & Hobbs, W. R. (2016). The Amundsen Sea Low: Variability, Change, and Impact on Antarctic Climate. *Bulletin of the American Meteorological Society*, *97*(1), 111–121. https://doi.org/10.1175/BAMS-D-14-00018.1

Reijmer, C. H., & Oerlemans, J. (2002). Temporal and spatial variability of the surface energy balance in Dronning Maud Land, East Antarctica. *Journal of Geophysical Research: Atmospheres*, *107*(D24), ACL 9-1-ACL 9-12. https://doi.org/10.1029/2000JD000110

Rodrigo, J. S., & Anderson, P. S. (2013). Investigation of the Stable Atmospheric Boundary Layer at Halley Antarctica. *Boundary-Layer Meteorology*, *148*(3), 517–539. https://doi.org/10.1007/s10546-013-9831-0

Rogers, J. C., & Loon, H. van. (1982). Spatial Variability of Sea Level Pressure and 500 mb Height Anomalies over the Southern Hemisphere. *Monthly Weather Review*, *110*(10), 1375–1392. https://doi.org/10.1175/1520-0493(1982)110<1375:SVOSLP>2.0.CO;2

Rondanelli, R., Hatchett, B., Rutllant, J., Bozkurt, D., & Garreaud, R. (2019). Strongest MJO on Record Triggers Extreme Atacama Rainfall and Warmth in Antarctica. *Geophysical Research Letters*, *46*(6), 3482–3491. https://doi.org/10.1029/2018GL081475

Ruth, U., Barbante, C., Bigler, M., Delmonte, B., Fischer, H., Gabrielli, P., Gaspari, V., Kaufmann, P., Lambert, F., Maggi, V., Marino, F., Petit, J.-R., Udisti, R., Wagenbach, D., Wegner, A., & Wolff, E. W. (2008). Proxies and

Measurement Techniques for Mineral Dust in Antarctic Ice Cores. *Environmental Science & Technology*, *42*(15), 5675–5681. https://doi.org/10.1021/es703078z

Ruth, U., Barnola, J.-M., Beer, J., Bigler, M., Blunier, T., Castellano, E., Fischer, H., Fundel, F., Huybrechts, P., Kaufmann, P., Kipfstuhl, S., Lambrecht, A., Morganti, A., Oerter, H., Parrenin, F., Rybak, O., Severi, M., Udisti, R., Wilhelms, F., & Wolff, E. (2007). "EDML1": A chronology for the EPICA deep ice core from Dronning Maud Land, Antarctica, over the last 150 000 years. *Climate of the Past*, *3*(3), 475–484. https://doi.org/10.5194/cp-3-475-2007

Ruth, U., Wagenbach, D., Bigler, M., Steffensen, J. P., Röthlisberger, R., & Miller, H. (2002). High-resolution microparticle profiles at NorthGRIP, Greenland: Case studies of the calcium–dust relationship. *Annals of Glaciology*, *35*, 237–242. https://doi.org/10.3189/172756402781817347

Ruth, U., Wagenbach, D., Steffensen, J. P., & Bigler, M. (2003). Continuous record of microparticle concentration and size distribution in the central Greenland NGRIP ice core during the last glacial period. *Journal of Geophysical Research: Atmospheres*, *108*(D3). https://doi.org/10.1029/2002JD002376

Schepanski, K., Merkel, U., & Tegen, I. (2014). Mineral dust: Meteorological controls and climate impacts. *Past Global Changes Magazine*, *22*(2), 62–63. https://doi.org/10.22498/pages.22.2.62

Schubert, S. D., Suarez, M. J., Pegion, P. J., Koster, R. D., & Bacmeister, J. T. (2004). On the Cause of the 1930s Dust Bowl. *Science*. https://doi.org/10.1126/science.1095048

Seibert, P., & Frank, A. (2004). Source-receptor matrix calculation with a Lagrangian particle dispersion model in backward mode. *Atmospheric Chemistry and Physics*, *4*(1), 51–63. https://doi.org/10.5194/acp-4-51-2004

Shaffer, G., & Lambert, F. (2018). In and out of glacial extremes by way of dust−climate feedbacks. *Proceedings of the National Academy of Sciences*, *115*(9), 2026–2031. https://doi.org/10.1073/pnas.1708174115

Shao, Y. (2014). Including dust dynamics in paleoclimate modeling. *Past Global Changes Magazine*, *22*(2), 66–67. https://doi.org/10.22498/pages.22.2.66

Sigman, D. M., Hain, M. P., & Haug, G. H. (2010). The polar ocean and glacial cycles in atmospheric CO2 concentration. *Nature*, *466*(7302), 47–55. https://doi.org/10.1038/nature09149

Simms, A. R., Bentley, M. J., Simkins, L. M., Zurbuchen, J., Reynolds, L. C., DeWitt, R., & Thomas, E. R. (2021). Evidence for a “Little Ice Age” glacial advance within the Antarctic Peninsula – Examples from glacially-overrun raised beaches. *Quaternary Science Reviews*, *271*, 107195. https://doi.org/10.1016/j.quascirev.2021.107195

Simpkins, G. R., & Karpechko, A. Yu. (2012). Sensitivity of the southern annular mode to greenhouse gas emission scenarios. *Climate Dynamics*, *38*(3), 563–572. https://doi.org/10.1007/s00382-011-1121-2

Slinn, W. G. N. (1982). Predictions for particle deposition to vegetative canopies. *Atmospheric Environment (1967)*, *16*(7), 1785–1794. https://doi.org/10.1016/0004-6981(82)90271-2

Solomon, S., Ivy, D. J., Kinnison, D., Mills, M. J., Ryan R. Neely, I. I. I., & Schmidt, A. (2016). Emergence of healing in the Antarctic ozone layer. *Science*. https://doi.org/10.1126/science.aae0061

Sommer, S., Wagenbach, D., Mulvaney, R., & Fischer, H. (2000). Glacio-chemical study spanning the past 2 kyr on three ice cores from Dronning Maud Land, Antarctica: 2. Seasonally resolved chemical records. *Journal of Geophysical Research: Atmospheres*, *105*(D24), 29423–29433. https://doi.org/10.1029/2000JD900450

Stohl, A., Eckhardt, S., Forster, C., James, P., Spichtinger, N., & Seibert, P. (2002). A replacement for simple back trajectory calculations in the interpretation of atmospheric trace substance measurements. *Atmospheric Environment*, *36*(29), 4635–4648. https://doi.org/10.1016/S1352-2310(02)00416-8

Stohl, A., Forster, C., Frank, A., Seibert, P., & Wotawa, G. (2005). Technical note: The Lagrangian particle dispersion model FLEXPART version 6.2. *Atmospheric Chemistry and Physics*, *5*(9), 2461–2474. https://doi.org/10.5194/acp-5-2461-2005

Stohl, A., Hittenberger, M., & Wotawa, G. (1998). Validation of the lagrangian particle dispersion model FLEXPART against large-scale tracer experiment data. *Atmospheric Environment*, *32*(24), 4245–4264. https://doi.org/10.1016/S1352-2310(98)00184-8

Struve, T., Pahnke, K., Lamy, F., Wengler, M., Böning, P., & Winckler, G. (2020). A circumpolar dust conveyor in the glacial Southern Ocean. *Nature Communications*, *11*(1), 5655. https://doi.org/10.1038/s41467-020-18858-y

Stuut, J.-B. W., & Prins, M. A. (2014). The significance of particle size of long-range transported mineral dust. *Past Global Changes Magazine*, *22*(2), 70–71. https://doi.org/10.22498/pages.22.2.70

Sutherland, W. (1893). LII. The viscosity of gases and molecular force. *The London, Edinburgh, and Dublin Philosophical Magazine and Journal of Science*, *36*(223), 507–531. https://doi.org/10.1080/14786449308620508

Tegen, I., Lacis, A. A., & Fung, I. (1996). The influence on climate forcing of mineral aerosols from disturbed soils. *Nature*, *380*(6573), 419–422. https://doi.org/10.1038/380419a0

Tetzner, D., Thomas, E. R., Allen, C. S., & Wolff, E. W. (2021). A Refined Method to Analyze Insoluble Particulate Matter in Ice Cores, and Its Application to Diatom Sampling in the Antarctic Peninsula. *Frontiers in Earth Science*, *9*. https://doi.org/10.3389/feart.2021.617043

Thomas, E. R., van Wessem, J. M., Roberts, J., Isaksson, E., Schlosser, E., Fudge, T. J., Vallelonga, P., Medley, B., Lenaerts, J., Bertler, N., van den Broeke, M. R., Dixon, D. A., Frezzotti, M., Stenni, B., Curran, M., & Ekaykin, A. A. (2017). Regional Antarctic snow accumulation over the past 1000 years. Climate of the Past, 13(11), 1491–1513. https://doi.org/10.5194/cp-13-1491-2017

Thompson, D. W. J., & Solomon, S. (2002). Interpretation of Recent Southern Hemisphere Climate Change. *Science*. https://doi.org/10.1126/science.1069270

Thompson, D. W. J., Solomon, S., Kushner, P. J., England, M. H., Grise, K. M., & Karoly, D. J. (2011). Signatures of the Antarctic ozone hole in Southern Hemisphere surface climate change. *Nature Geoscience*, *4*(11), 741–749. https://doi.org/10.1038/ngeo1296

Thompson, D. W. J., & Wallace, J. M. (2000). Annular Modes in the Extratropical Circulation. Part I: Month-to-Month Variability. *Journal of Climate*, *13*(5),

1000–1016. https://doi.org/10.1175/1520-0442(2000)013<1000:AMITEC>2.0.CO;2

Traufetter, F., Oerter, H., Fischer, H., Weller, R., & Miller, H. (2004). Spatio-temporal variability in volcanic sulphate deposition over the past 2 kyr in snow pits and firn cores from Amundsenisen, Antarctica. *Journal of Glaciology*, *50*(168), 137–146. https://doi.org/10.3189/172756504781830222

Turner, J., Colwell, S. R., Marshall, G. J., Lachlan-Cope, T. A., Carleton, A. M., Jones, P. D., Lagun, V., Reid, P. A., & Iagovkina, S. (2005). Antarctic climate change during the last 50 years. *International Journal of Climatology*, *25*(3), 279–294. https://doi.org/10.1002/joc.1130

Turner, J., Lu, H., White, I., King, J. C., Phillips, T., Hosking, J. S., Bracegirdle, T. J., Marshall, G. J., Mulvaney, R., & Deb, P. (2016). Absence of 21st century warming on Antarctic Peninsula consistent with natural variability. *Nature*, *535*(7612), 411–415. https://doi.org/10.1038/nature18645

Turner, J., Phillips, T., Hosking, J. S., Marshall, G. J., & Orr, A. (2013). The Amundsen Sea low. *International Journal of Climatology*, *33*(7), 1818–1829. https://doi.org/10.1002/joc.3558

Turner, J., Marshall, G. J., Clem, K., Colwell, S., Phillips, T., & Lu, H. (2019a). Antarctic temperature variability and change from station data. *International Journal of Climatology*, *40*(6), 2986–3007. https://doi.org/10.1002/joc.6378

Turner, J., Phillips, T., Thamban, M., Rahaman, W., Marshall, G. J., Wille, J. D., Favier, V., Winton, V. H. L., Thomas, E., Wang, Z., van den Broeke, M., Hosking, J. S., & Lachlan-Cope, T. (2019b). The Dominant Role of Extreme Precipitation Events in Antarctic Snowfall Variability. *Geophysical Research Letters*, *46*(6), 3502–3511. https://doi.org/10.1029/2018GL081517

Vallelonga, P. (2014). The enigma of dust provenance: Where else does Antarctic dust come from? *Past Global Changes Magazine*, *22*(2), 74–75. https://doi.org/10.22498/pages.22.2.74

Vallelonga, P., & Svensson, A. (2014). Ice Core Archives of Mineral Dust. In P. Knippertz & J.-B. W. Stuut (Eds.), *Mineral Dust: A Key Player in the Earth System* (pp. 463–485). Springer Netherlands. https://doi.org/10.1007/978-94-017-8978-3_18

Verdon, D. C., & Franks, S. W. (2006). Long-term behaviour of ENSO: Interactions with the PDO over the past 400 years inferred from paleoclimate records. *Geophysical Research Letters*, *33*(6). https://doi.org/10.1029/2005GL025052

Viglizzo, E. F., & Frank, F. C. (2006). Ecological interactions, feedbacks, thresholds and collapses in the Argentine Pampas in response to climate and farming during the last century. *Quaternary International*, *158*(1), 122–126. https://doi.org/10.1016/j.quaint.2006.05.022

Vincent, D. G. (1994). The South Pacific Convergence Zone (SPCZ): A Review. *Monthly Weather Review*, *122*(9), 1949–1970. https://doi.org/10.1175/1520-0493(1994)122<1949:TSPCZA>2.0.CO;2

Wallace, J. M., & Hobbs, P. V. (2006). *Atmospheric Science, Second Edition: An Introductory Survey* (2nd edition). Academic Press.

Wang, C., Deser, C., Yu, J.-Y., DiNezio, P., & Clement, A. (2017). El Niño and Southern Oscillation (ENSO): A Review. In P. W. Glynn, D. P. Manzello, & I. C. Enochs (Eds.), *Coral Reefs of the Eastern Tropical Pacific: Persistence and Loss in a Dynamic Environment* (pp. 85–106). Springer Netherlands. https://doi.org/10.1007/978-94-017-7499-4_4

Wang, G., Hendon, H. H., Arblaster, J. M., Lim, E.-P., Abhik, S., & van Rensch, P. (2019). Compounding tropical and stratospheric forcing of the record low Antarctic sea-ice in 2016. *Nature Communications*, *10*(1), 13. https://doi.org/10.1038/s41467-018-07689-7

Wang, Y. Q., Zhang, X. Y., & Draxler, R. R. (2009). TrajStat: GIS-based software that uses various trajectory statistical analysis methods to identify potential sources from long-term air pollution measurement data. *Environmental Modelling & Software*, *24*(8), 938–939. https://doi.org/10.1016/j.envsoft.2009.01.004

Wegner, A., Fischer, H., Delmonte, B., Petit, J.-R., Erhardt, T., Ruth, U., Svensson, A., Vinther, B., & Miller, H. (2015). The role of seasonality of mineral dust concentration and size on glacial/interglacial dust changes in the EPICA Dronning Maud Land ice core. *Journal of Geophysical Research: Atmospheres*, *120*(19), 9916–9931. https://doi.org/10.1002/2015JD023608

Wegner, A., Gabrielli, P., Wilhelms-Dick, D., Ruth, U., Kriews, M., De Deckker, P., Barbante, C., Cozzi, G., Delmonte, B., & Fischer, H. (2012). Change in dust variability in the Atlantic sector of Antarctica at the end of the last deglaciation. *Climate of the Past*, *8*(1), 135–147. https://doi.org/10.5194/cp-8-135-2012

Weller, R., & Wagenbach, D. (2007). Year-round chemical aerosol records in continental Antarctica obtained by automatic samplings. *Tellus B: Chemical and Physical Meteorology*, *59*(4), 755–765. https://doi.org/10.1111/j.1600-0889.2007.00293.x

Wernli, H., & Davies, H. C. (1997). A Lagrangian-based analysis of extratropical cyclones. I: The method and some applications. *Quarterly Journal of the*

Royal Meteorological Society, *123*(538), 467–489. https://doi.org/10.1002/qj.49712353811

Wills, R. C., Schneider, T., Wallace, J. M., Battisti, D. S., & Hartmann, D. L. (2018). Disentangling Global Warming, Multidecadal Variability, and El Niño in Pacific Temperatures. *Geophysical Research Letters*, *45*(5), 2487–2496. https://doi.org/10.1002/2017GL076327

Wilschefski, S. C., & Baxter, M. R. (2019). Inductively Coupled Plasma Mass Spectrometry: Introduction to Analytical Aspects. *The Clinical Biochemist. Reviews*, *40*(3), 115–133. https://doi.org/10.33176/AACB-19-00024

Winton, V.H.L, Caillon, N., Hauge, L., Mulvaney, R., Rix, J., Savarino, J., Tuckwell, R., Frey, M. (2019). Ice core chemistry, density, conductivity, dust, snow accumulation rate, and stable nitrate isotopic composition of the 120 m ISOL-ICE ice core, Dronning Maud Land, Antarctica (Version 1.0) [Data set]. UK Polar Data Centre, Natural Environment Research Council, UK Research & Innovation. doi.org/10.5285/9c972cfb-0ffa-4144-a943-da6eb82431d2 (Unreleased data).

Winton, V. H. L., Edwards, R., Delmonte, B., Ellis, A., Andersson, P. S., Bowie, A., Bertler, N. a. N., Neff, P., & Tuohy, A. (2016). Multiple sources of soluble atmospheric iron to Antarctic waters. *Global Biogeochemical Cycles*, *30*(3), 421–437. https://doi.org/10.1002/2015GB005265

Winton, V. H. L., Ming, A., Caillon, N., Hauge, L., Jones, A. E., Savarino, J., Yang, X., & Frey, M. M. (2020). Deposition, recycling, and archival of nitrate stable isotopes between the air–snow interface: Comparison between Dronning Maud Land and Dome C, Antarctica. *Atmospheric Chemistry and Physics*, *20*(9), 5861–5885. https://doi.org/10.5194/acp-20-5861-2020

Wotawa, G., De Geer, L.-E., Denier, P., Kalinowski, M., Toivonen, H., D'Amours, R., Desiato, F., Issartel, J.-P., Langer, M., Seibert, P., Frank, A., Sloan, C., & Yamazawa, H. (2003). Atmospheric transport modelling in support of CTBT verification—Overview and basic concepts. *Atmospheric Environment*, *37*(18), 2529–2537. https://doi.org/10.1016/S1352-2310(03)00154-7

Yamamoto, A., Abe-Ouchi, A., Ohgaito, R., Ito, A., & Oka, A. (2019). Glacial CO_2 decrease and deep-water deoxygenation by iron fertilization from glaciogenic dust. *Climate of the Past*, *15*(3), 981–996. https://doi.org/10.5194/cp-15-981-2019

Yang, S., Li, Z., Yu, J.-Y., Hu, X., Dong, W., & He, S. (2018). El Niño–Southern Oscillation and its impact in the changing climate. *National Science Review*, *5*(6), 840–857. https://doi.org/10.1093/nsr/nwy046

Yuan, X. (2004). ENSO-related impacts on Antarctic sea ice: a synthesis of phenomenon and mechanisms. *Antarctic Science*, *16*(4), 415–425. https://doi.org/10.1017/S0954102004002238

Yuan, X., Kaplan, M. R., & Cane, M. A. (2018). The Interconnected Global Climate System—A Review of Tropical–Polar Teleconnections. *Journal of Climate*, *31*(15), 5765–5792. https://doi.org/10.1175/JCLI-D-16-0637.1

Yuan, X., & Martinson, D. G. (2001). The Antarctic dipole and its predictability. *Geophysical Research Letters*, *28*(18), 3609–3612. https://doi.org/10.1029/2001GL012969

Zhang, Y., Wallace, J. M., & Battisti, D. S. (1997). ENSO-like Interdecadal Variability: 1900–93. *Journal of Climate*, *10*(5), 1004–1020. https://doi.org/10.1175/1520-0442(1997)010<1004:ELIV>2.0.CO;2

Zielinski, G. A., Mayewski, P. A., Meeker, L. D., Whitlow, S., Twickler, M. S., Morrison, M., Meese, D. A., Gow, A. J., & Alley, R. B. (1994). Record of Volcanism Since 7000 B.C. from the GISP2 Greenland Ice Core and Implications for the Volcano-Climate System. *Science*. https://doi.org/10.1126/science.264.5161.948